Electrical effects in ferromagnetic resonance of nanostructures and atomic contacts

Olivier Rousseau

Thèse de Doctorat de l'Université Pierre et Marie Curie

Olivier ROUSSEAU

Effets électriques lors de la résonance ferromagnétique de nanostructures et de contacts atomiques

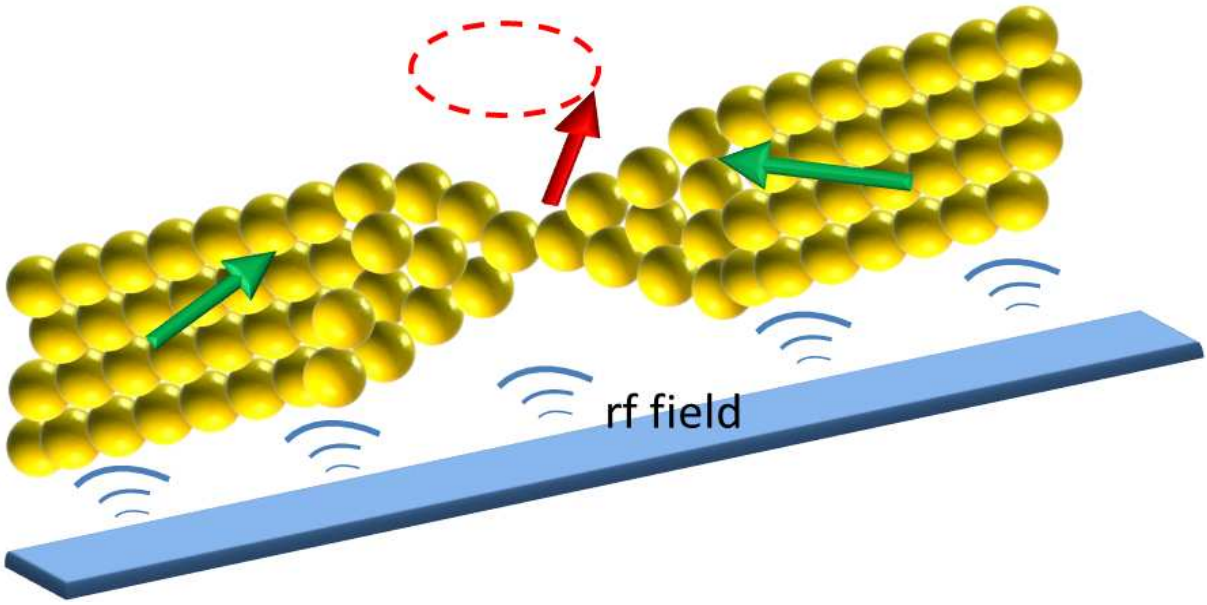

Service de Physique de l'Etat Condensée -CEA Saclay

UNIVERSITE PARIS VI - PIERRE ET MARIE CURIE
ECOLE DOCTORALE DE PHYSIQUE DE LA REGION PARISIENNE

THÈSE

Pour obtenir le grade de:

Docteur de l'Université Pierre et Marie Curie - Paris VI
Specialité : Physique

Présentée par

Olivier ROUSSEAU

Effets électriques lors de la résonance ferromagnétique de nanostructures et de contacts atomiques

Thèse préparée dans le groupe nanomagnétisme et RMN au sein du Service de Physique de l'Etat Condensée
CEA-Saclay 91191 Gif-sur-Yvette

soutenue le 16 décembre 2011 devant le jury composé de :

Rapporteurs :	YoshiChika OTANI
	Thibaut DEVOLDER
Examinateurs :	Albert FERT
	André THIAVILLE
	Rolf ALLENSPACH
	Massimiliano MARANGOLO
Directeur de thèse:	Michel VIRET

REMERCIEMENT

Je voudrais en premier lieu remercier mon directeur de thèse Michel Viret qui m'a encadré durant ces trois années de thèse. Je le remercie pour sa disponibilité, pour la confiance qu'il m'a accordée et pour son enthousiasme envers mes expériences. Je remercie également Sébastien Petit Watelot avec qui j'ai monté le dispositif expérimental durant son post-doc qui a dû partir quand celui-ci a commencé à donner des résultats, pour son aide et sa bonne humeur.

Merci à Eric Vincent de m'avoir accueilli au Service de Physique de l'Etat Condensée et Claude Fermon dans le groupe " Nanomagnétisme et RMN ". Je remercie également toutes les personnes qui m'ont donné accès à des moyens expérimentaux performants tant pour la fabrication (en particulier Pief Orfila, Gérald Le Goff et Grégory Cannies) ainsi que pour m'avoir prêté du matériel afin de tester mes besoins. Je pense notamment à Fabien Portier qui nous a prêté une source rf pendant de nombreux mois.

Je remercie également toutes les autres personnes du groupe GNM (en particulier Grégoire, Olivier, Aymen, Bodhan, Ruben, Natalia, Hadrien et Reda) et du SPEC en général pour leur accueil et les discussions de physique (entre autres) que nous avons eu. Bonne chance aux thésards actuels(Aurélie, Benjamin, Quentin, Christian, Abbass) pour la fin de leur thèse.

Je tiens également à remercier toutes les personnes de l'ANR SUD à laquelle j'ai pu collaborer du début à la fin, particulièrement Bernard Doudin, Matthieu Kociak et Cyrille Barreteau. Je remercie également Pascal Thibaudeau et David Beaujouan du CEA Le Ripault, pour avoir commencé des simulations sur la dynamique de l'aimant tion dans des contacts atomiques qui seront, je n'en doute pas, fructueuses.

Merci à tous les membres du jury pour le temps consacré à lecture du manuscrit ainsi qu'à ma soutenance.

Electrical effects in ferromagnetic resonance of nanostructures and atomic contacts

Olivier ROUSSEAU

December 16, 2011

RÉSUMÉ

Le but de cette thèse est l'étude des propriétés de résonance ferromagnétique (RFM) de nanostructures et contacts atomiques. Pour ce faire, nous exploitons le fait que les propriétés de transport électrique sont dominées par le contact atomique, et nous utilisons une détection électrique. Nous avons développé un nouveau dispositif expérimental dans lequel un dispositif mécanique de jonctions à cassure est conçu pour un environnement hyperfréquence où les mesures électriques peuvent être réalisées avec des champs magnétiques statiques et dynamiques variables. Des nanostructures ont d'abord été mesurées pour déterminer la fiabilité et la grande sensibilité de notre système. Ensuite la susceptibilité, de parois de domaines à des fréquences supérieures à celles les propageant, a été déterminée comme indépendante de la fréquence. Cette susceptibilité était environ 10 fois supérieure à celle des domaines saturés. Le dispositif expérimental permet également d'étudier l'interaction entre courants de spins et propriétés dynamiques de nanostructures pendant la résonance ferromagnétique. Les courants de spins générés dynamiquement à la RFM ont été mesurés en utilisant l'effet Hall inverse de spin dans des nanostructures Py/Pt. L'influence, sur la RFM, des courants de spin injectés par effet Hall de spin dans le platine, y a également été observée.

Dans les contacts atomiques la RFM a aussi été étudiée à l'aide de mesures du signal rectifié. Lors de la cassure de nos nanostructures de cobalt ou de permalloy, de nouveaux modes de résonance apparaissent à des champs plus élevés que la résonance uniforme. Nous attribuons cet effet à la modification des champs démagnétisant lors de la réduction du diamètre de la constriction. Dans la géométrie du contact atomique, nous avons mesuré la résonance de parois de domaines contraintes. Dans ce cas, le signal rectifié généré par quelques atomes, dépend fortement de la fréquence et peut atteindre des valeurs 1000 fois supérieures à celles de la RFM des domaines avant cassure.

Mots clés :

Résonance ferromagnétique
Parois de domaines
Nanostructures
Contacts atomiques
Effet Hall de spin
Effet Hall inverse de spin

ABSTRACT

The aim of this thesis is the study of ferromagnetic resonance properties (FMR) of nanostructures and atomic contacts. In order to achieve this, we take advantage of the fact that electrical transport is dominated by the atomic contact, and use an electrical detection technique. We developed a novel experimental setup in which a mechanical break junction technique is designed in a radio-frequency compatible environment where electrical measurements can be carried out under variable static and dynamical magnetic fields. First, magnetic nanostructures were measured in order to determine the reliability and the high sensitivity of our system. Then the susceptibility of domain walls in nanostuctures at frequencies higher than those classically used for their displacement, was measured and found to be large and almost independent of the frequency. This susceptibility was roughly 10 times that in saturated domains. The experimental setup also allowed the study of the interaction of spin currents and dynamical properties of nanostructures at the ferromagnetic resonance. The spin currents dynamically generated at the FMR have been measured in Py/Pt nanostructures using the inverse spin Hall effect in platinum. The influence on the FMR of spin current injection using the spin Hall effect in Pt has also been observed.

The FMR of atomic contacts has been studied by a rectified technique. While breaking our nanostructures of cobalt and permalloy, new resonant modes have been shown to appear at fields higher than that of the uniform resonance. This is attributed to the effect of demagnetization fields that are locally modified when reducing the constriction diameter. In the atomic contact regime, we have measured the constrained domain wall resonance. In that case the rectified signal, generated by a few atoms, depends sensitively on the frequency and can reach values 1000 times higher than the FMR signal of saturated domains in the unbroken samples.

Key words:

Ferromagnetic resonance
Domain walls
Nanostructures
Atomic contacts
Spin-Hall effect
Inverse spin-Hall effect

Contents

Introduction

Tunnel and giant magnetoresitance effects are the basic principles of several spintronic devices, a branch of electronics using the spin of electrons. Spintronic applications are mainly in information technologies and even more in computer science. They are used as magnetic field sensors in the read heads of hard disks. The magnetoresistive elements are the basics of new non volatile memories, the MRAMs (magnetic random access memories) which are now commercialized. While reducing device size, the physics of spin transport still raises several questions, especially when dimensions are small enough to enter into the ballistic transport regime. In that case several properties could change including magnetoresistance and local magnetism.

Ferromagnetic resonance (FMR) has been widely studied these last years in micro and nano scale, especially in the spin valve geometry like in MRAMs. However it has never been studied down to ultimate sizes like atomic contacts, which are well in the ballistic regime of transport. At this scale, the atoms environment are no more like in solids, and the low dimensionality can dramatically change the local magnetic properties. In particular, the orbital moments [1, 2], that are quenched in crystals, can be recovered, thus significantly modifying the local moments as well as the anisotropy. In these atomic contacts, it is very hard to investigate the properties of only a few relevant atoms and often one has to 'guess' them indirectly [3, 4, 5], through their effect on electronic transport. Here, we propose to introduce a new tool consisting in studying the magnetization dynamic properties of these contacts. This technique (FMR measurements) is known to provide key information on spin and orbital moments as well as anisotropy. Classically, in order to detect the FMR, one uses inductive techniques which give signals that scale with the probed volume. Thus, it is impossible to measure a single, or a few atoms. Here, we have chosen to detect the FMR electrically in the hope that the FMR signature on transport could provide an extremely local measurement. Indeed FMR influences the resistance of magnetic materials [6] through the anisotropic magnetoresistance (AMR) effect. Moreover electronic transport is a very good tool to probe the properties of the few atoms or even molecule [7] composing an atomic contact because the resistance is dominated by the narrowest constriction. Our resistance measurements are performed using a break-junction setup at 77 K under applied static and radio-

frequency magnetic fields in an optimized environment regarding thermal stability and electronic noise.

In this work we are also interested in the interactions between dynamical magnetic properties and spin currents. This is one of the 'hot' topics of the moment in spintronics as spin currents are non-dissipative quantities that could potentially be manipulated and used as a vector of information. Our setup also allows for some original measurements to be carried out in magnetic nanostructures in contact with normal metals using the Spin Hall Effect (SHE) and the Inverse Spin Hall Effect (ISHE) [8, 9]. Several studies of spin currents and FMR have already been reported either using electrical detection in large samples [10, 11] or with a non electrical measurement like Brillouin light scattering [12] on small samples. In this thesis work, we are interested in the spin Hall effects (inverse and direct) at the FMR of bilayer nanostructures.

This thesis manuscript is divided in six chapters. The first three chapters are general information on the basic physics and the experimental set up. In the last three chapters our measurements of FMR are presented.

The first chapter gives the basics of magnetism, ferromagnetic resonance and atomic contacts. First static ferromagnetism and its effect on resistance is introduced, then the basic theory of magnetization dynamics is tackled, and finally atomic contacts and their static magnetic properties are presented.

The second chapter presents the design of the sample with the rf antenna as well as the fabrication process.

The third chapter describes the experimental setup with the characterization of the rf excitation. Two different measurements and their expected signals are explained in details including their origin and the information that will be extracted in the following chapters.

Chapter four characterizes the sensitivity of our measurements, in terms of angular resolution of the magnetization precession with the two different techniques. We will in particular address the non propagative domain wall resonance in thin layers and how it depends on the nature of the domain wall. In a second part we extend the measurements to thicker samples and study how the FMR spectra are changed from those obtained in of the thin layers.

The fifth part deals with ferromagnetic resonance in atomic contacts as the samples are being controllably broken. The resonance of atomic sized domain walls has been observed and found to be very different from domain resonance or domain wall resonance in the unbroken nanostructures. The necessity of supplementary theoretical work to fully understand domain wall resonance in atomic contacts is

underlined.

Lastly, the sixth chapter deals with spin currents and FMR. The Hall effects and generation of spin currents are tackled. Then the ISHE measurements in nanostructures are explained as well as the influence of spin currents on the magnetization damping at resonance.

Chapter 1

Magnetism and its dynamics in nanostructures

In this first chapter, the basics of magnetism and magnetization dynamics are given. First, the main contributions to the magnetic energy are detailed to give an overview of the important parameters for magnetism experiments as well are the effect of magnetism on the resistance. Next a short introduction to spin dynamics settles the ground for the fundamental magnetization dynamics equation. To finish this introduction the field of atomic contacts is presented with respect to electrical transport and magnetism.

1.1 Static ferromagnetism in nanostructures

In this section, static micromagnetism is introduced before describing the main effects of magnetism on resistive properties.

1.1.1 Micromagnetism

In this part static micromagnetism in ferromagnets is described. The main objective of micromagnetism is to determine the distribution of magnetization directions. The first blocks of this field were set by Landau and Lifshitz in 1935 [13]. The theory is based on magnetic energy minimization. In the following are described the main contributions to this energy. In the end, the equilibrium of magnetization, in a stripe like those used in here in later experiments, is derived from these energy sources.

1.1.1.1 Exchange energy

Historically, Weiss first supposed that a magnetic field called molecular field was responsible for the coherence of spin direction in ferromagnetic materials. Later Heinsenberg established that this molecular field was due to a spin-spin interaction, now called *exchange*. The quantum origin of this interaction comes from the Pauli exclusion principle and Coulomb interaction. Indeed, both position and motion of electrons are conditioned by their spin states as two electrons can not be in exactly the same quantum state at the same place. This creates a spin correlation between first neighbors. In metals, electronic band structures have to be taken into account. In insulators, this interaction between first neighbors exists but it is due to the overlap of localized electron wave functions.
The exchange hamiltonian $\mathcal{H}$ can be written considering pairs of spins (i,j):

$$\mathcal{H} = -\sum_{(i,j)} J_{i,j} \vec{S}_i \vec{S}_j \tag{1.1}$$

with $J_{i,j}$ the exchange interaction parameter between spin i and j. J is positive for ferromagnets and negative for anti-ferromagnets for the first neighbors. In the continuous limit, the exchange energy of a magnetic volume V is:

$$E_X = \frac{A}{M_S^2} \int_V (\overrightarrow{\nabla}.\overrightarrow{M})^2 dV \tag{1.2}$$

where

- A is the exchange energy. It depends on J and the crystal structure.
- $\overrightarrow{M}$ is magnetization
- M_S is saturation magnetization
- $\overrightarrow{\nabla}$ is nabla operator

For permalloy the length where the exchange energy dominates, is about 5 nm.

1.1.1.2 Zeeman energy

The Zeeman energy comes from the interaction between the magnetization and an external magnetic field H_A. This interaction tends to stabilize the magnetization along the applied field. The energy associated to the Zeeman interaction is:

$$E_Z = -\mu_0 \int_V \overrightarrow{H_A}.\overrightarrow{M} dV \tag{1.3}$$

where, μ_0 is the magnetic permeability in vacuum.

1.1.1.3 Magneto-crystalline anisotropy energy

Through spin orbit coupling, spins are sensitive to the lattice. In presence of a crystalline structure, a magnetic anisotropy which has a symmetry related to the crystalline symmetry, may appear. In the case of a uniaxial magneto-crystalline anisotropy, the associated energy is:

$$E_K = \int_V -\frac{K_U}{M_S^2}(\overrightarrow{M}.\overrightarrow{e_K})^2 dV \tag{1.4}$$

where $\overrightarrow{e_K}$ is the unitary vector along the easy axis.

1.1.1.4 Dipolar energy

Each individual spin creates a dipolar field which is felt by the other spins. As the dipolar field varies as $1/r^3$, it is a long range interaction and its associated energy should be calculated locally, taking into account the entire magnetic volume. For ellipsoids, it is possible to demonstrate that the dipolar field is constant (if the magnetization is also constant) and can be written as:

$$\overrightarrow{H}_D = -N\overrightarrow{M} \tag{1.5}$$

where N is a tensor. Often, the dipolar field is called demagnetizing field and the tensor N, tensor of demagnetizing coefficients. It is diagonal when expressed in the base of ellipsoid axes and its trace is equal to one, which is due to magnetization conservation. For non ellipsoidal bodies one can read ref [14].

In a mean field approximation (neglecting short range correlations), the energy associated with dipolar interactions is:

$$E_D = -\frac{\mu_0}{2}\int_V \overrightarrow{M}.\overrightarrow{H}_D dV \tag{1.6}$$

The factor 1/2 accounts for the fact that this is a self energy.

1.1.1.5 Equilibrium configuration

Solving the problem of minimizing locally this total energy leads to a condition of collinearity between the magnetization and an effective magnetic field defined as:

$$H_T = -\frac{1}{\mu_0}\nabla_{\vec{M}} E_T \tag{1.7}$$

$$= \overrightarrow{H}_X + \overrightarrow{H}_Z + \overrightarrow{H}_K + \overrightarrow{H}_D \tag{1.8}$$

where $\overrightarrow{H}_{\mathrm{X}}$, $\overrightarrow{H}_{\mathrm{Z}}$, $\overrightarrow{H}_{\mathrm{K}}$ and $\overrightarrow{H}_{\mathrm{D}}$ are magnetic fields associated to respectively exchange, Zeeman interaction, magneto-crystalline anisotropy and dipolar interactions. $\mathrm{E_T}$ is the density of energy. The exchange term is taken into account in the value of $\mathrm{M_S}$ as exchange generate the magnetic order. In the following, mostly Zeeman and demagnetizing fields (dipolar fields) are taken into account in the effective field. Indeed, in this work we mostly use permalloy $Ni_{80}Fe_{20}$ as the magnetic material whose magneto crystalline anisotropy can be neglected. We can then calculate

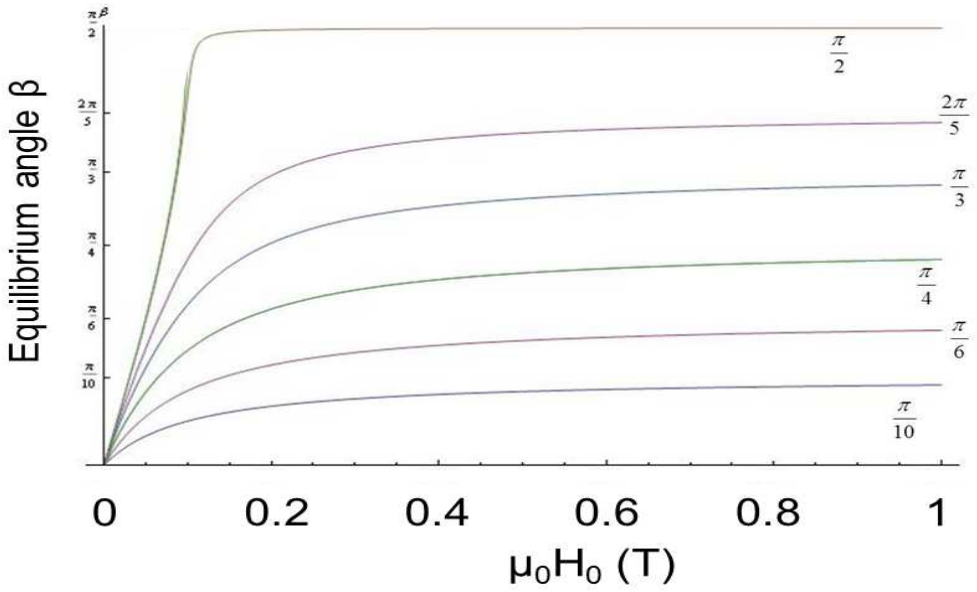

Figure 1.1: Numerical calculation of the in plane equilibrium position angle of magnetization versus magnetic field applied at different in plane angles considering a structure in a thin ellipse of infinite length and a width ten times the thickness (i.e. $N_y \cong 0.1$)

the angular equilibrium position of magnetization in plane $\beta \neq 0$ (angle between the magnetization and the long ellipsoid axis) for a thin infinite stripe with an applied static magnetic field $\vec{H}_0$ in the (x,y) plane with an angle ψ with the long axis $\vec{x}$. We suppose that the demagnetization tensor is that of an ellipse diagonal and constant thus $N_x = 0$. The magnetization energy E_m is given by:

$$\begin{aligned} E_m &= -\mu_0 \vec{H}_0 . \bar{M} + \frac{1}{2}\mu_0 (N\vec{M}).\vec{M} \\ &= -\mu_0 H_0 M_s \cos(\psi - \beta) + \frac{1}{2}\mu_0 N_y M_s^2 \sin^2 \beta \end{aligned}$$

The equilibrium is obtained for $\frac{dE_m}{d\beta} = 0$ so we obtain:

$$\frac{2H_0}{N_y M_s} \sin(\psi - \beta) = \sin(2\beta) \tag{1.9}$$

We can note that there is no analytical solution expected for $\psi = \pi/2$ when the magnetic field is transverse to the main direction of the stripe(i.e. perpendicular but in plane). In that case, there are two solutions: the trivial one $\beta = \pi/2$, and $\sin\beta = \frac{H}{N_y M_s}$. The second one is not always possible and the first one is not seen in zero applied magnetic field, so in reality the solution for $\psi = \pi/2$ is the second solution when H_0 is below $N_y M_s$ and $\pi/2$ above. In figure 1.1 the numerical solution of the problem is plotted for some applied angles of the magnetic field.

1.1.1.6 Domain walls

With the previous energies we obtain an unique magnetic domain where magnetization is constant or changes very slowly. Indeed, in a torus at the minimal energy configuration, the magnetization follows the torus geometry and even if the magnetization does not have a constant orientation, only one domain exists. Experimentally in nanostructures, or in solids, several domains of different orientations can coexist, separated by sharp borders. These sharp separations, where the magnetization rotates, are called domain walls. In bulk samples, domain walls are generally of the Bloch type, i.e. the domain wall magnetization is perpendicular to the plane of the wall. In thin films or nanostructures, Bloch domain walls generally cost too much in dipolar energy and the magnetization tends to minimize its out of plane component. This results in the stability of so called Neel domain walls that can be divided into two main categories: transverse and vortex domain walls [15]. As shown in figure 1.2 the nature of a domain wall depends on the different sizes: thickness, width or shape (see ref [16] for a review on domain wall in permalloy stripes and [17] in rings).

Domain walls can move under the action of a magnetic field, or a current using the spin torque effect. In some cases, this propagation can be helped by rf irradiation. While propagating, domain walls can be annihilated or merged even in a 360° domain wall where magnetization is doing a full turn (see ref [18] for 360° domain walls). A propagating domain wall reverses the magnetization but it can be slowed down by pinning centers. A domain wall pinned in a trap is realized by a local change in the effective magnetic field seen by the magnetic nanostructure, usually by changing the dipolar energy (an example in ref [4]). Thus, constrictions in stripes can act as traps as constrictions, but also as a region where domain walls can nucleate. Moreover, in their vicinity the nature of the domain wall can also be changed, which could be the case for vortex/transverse walls. Figure 1.3 shows a constriction and the behavior of a domain wall near or under the constriction.

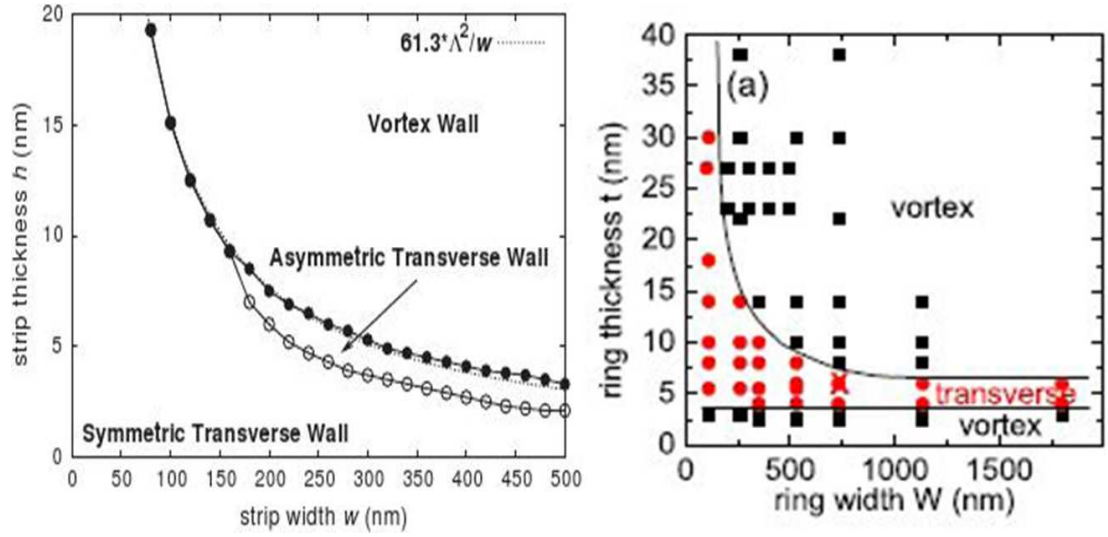

Figure 1.2: Example of phase diagram showing the stability of different domain walls in stripes on the left and rings on the right

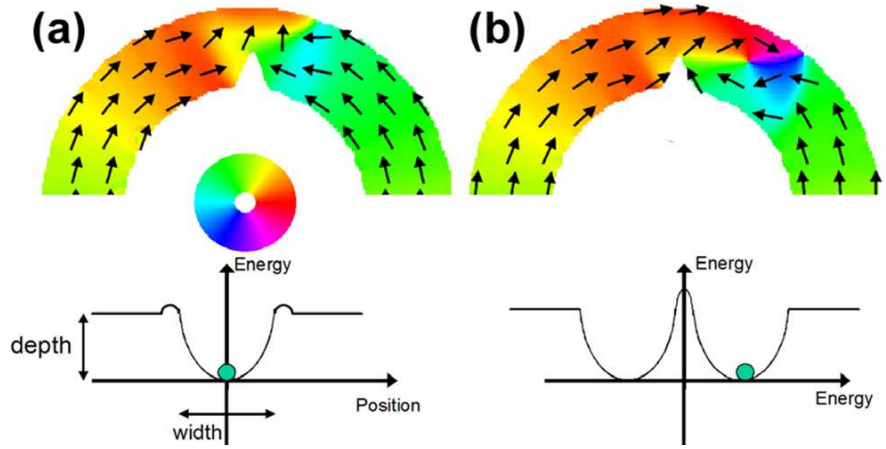

Figure 1.3: Image from reference [17] showing the influence of the nature of the domain wall on the energy landscape it sees due to the constriction.

1.1.2 Magnetism and resistance

In order to study the electrical signals generated by the ferromagnetic resonance , one has first to understand static properties. This also has to be extended to the extreme geometry of atomic contacts where some effects can be enhanced. So in this part we will discuss the influence of static ferromagnetism on the resistive behavior of the ferromagnetic nanostructures, with the notable exception of Hall effects which will be discussed in part 6.1. The two main relevant effects are

anisotropic magneto-resistance (AMR) and domain wall resistance (DWR), but for completeness we will also give here the basics of giant magnetoresistance (GMR) and tunneling magnetoresistance (TMR).

1.1.2.1 Anisotropic magnetoresistance

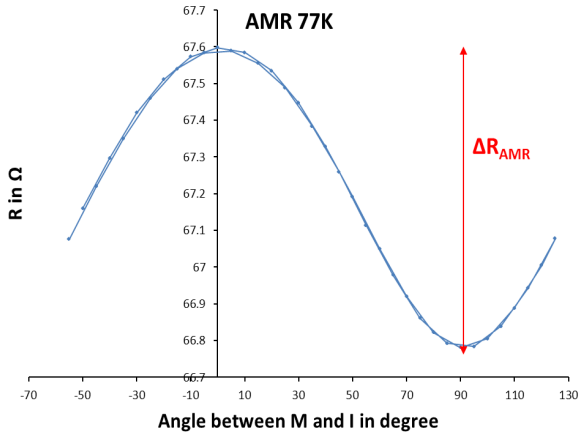

Figure 1.4: AMR measured on a simple stripe permalloy sample.

The main magnetization dependent resistivity in a homogeneous ferromagnet is the AMR. The resistivity depends on the angle between magnetization and current lines. In general and in our samples, the resistivity ρ is lower when the magnetization is perpendicular to the current lines. The AMR has its origin in the spin orbit coupling interaction. The sign of the AMR depends in fact on the band structure of the material, it is in fact negative in manganites. We can generally write the resistivity as

$$\rho = \rho_\perp + (\rho_\parallel - \rho_\perp) * \frac{(\vec{M}.\vec{j})^2}{(jM_s)^2} = \rho_\perp + (\rho_\parallel - \rho_\perp)\cos^2(\beta) \tag{1.10}$$

$$\rho_{AMR} = (\rho_\parallel - \rho_{perpen})\cos^2(\beta) \tag{1.11}$$

where β is the angle between the local current lines $\vec{j}$ and the local magnetization $\vec{M}$, M_s is the saturation magnetization. This is a local definition of resistance and for a full magnetic sample, it should be integrated on the total current lines. For our simple stripe samples at 77 K, we obtain a typical AMR curve like the one shown in figure 1.4, which amounts to about 1.5 % at 77 K in permalloy $Ni_{80}Fe_{20}$ (Py).

1.1.2.2 Giant magnetoresistance

The giant magnetoresistance (GMR) effect was discovered in 1988 by the teams of Fert [19] and Grunberg [20]. The GMR effect occurs in spin-valve systems. The spin-valves consist of a normal metallic (NM) spacer layer sandwitched between two ferromagnetic (FM) layers (thus a FM/NM/FM structure) as in figure 1.5

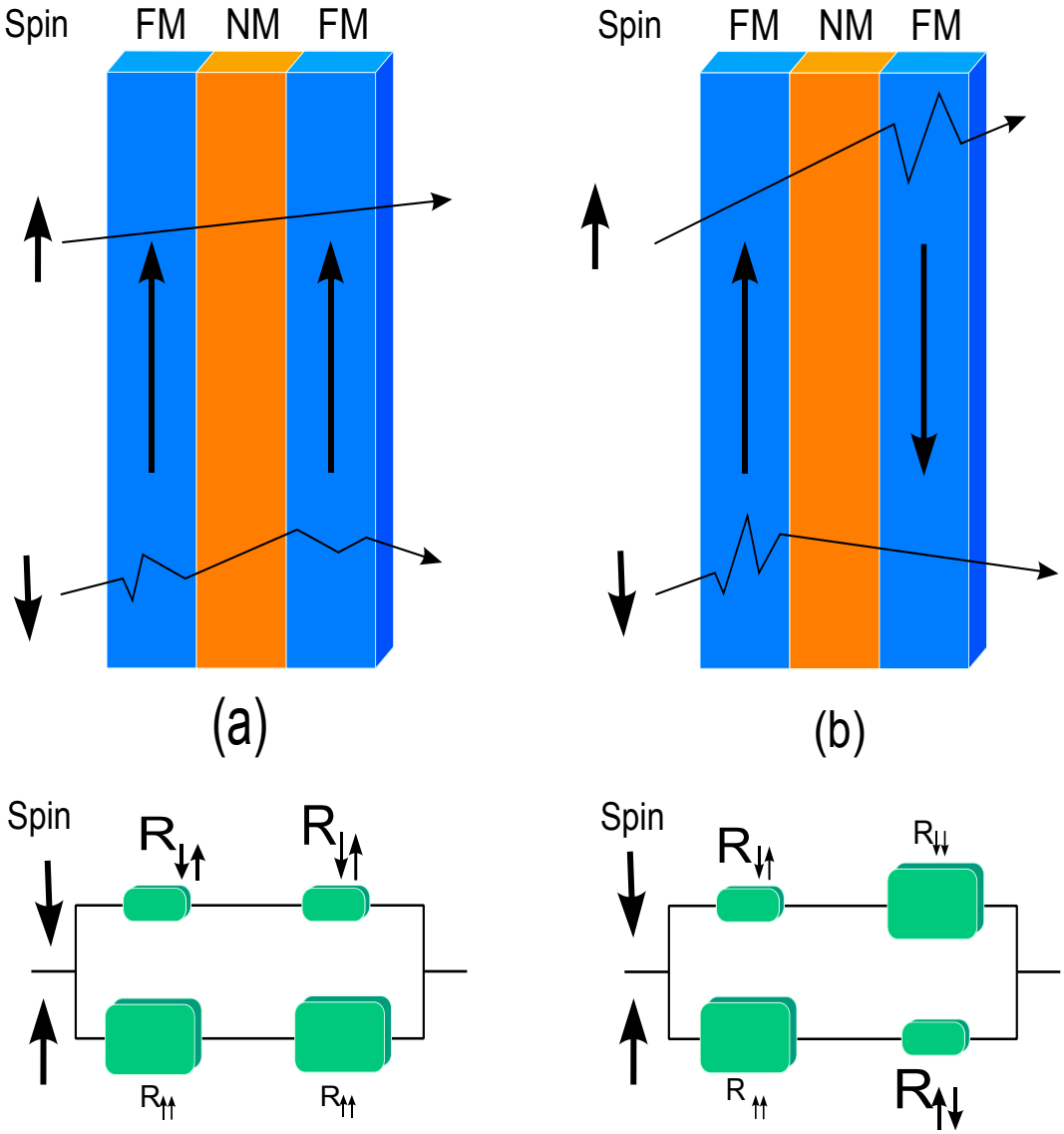

Figure 1.5: Principle of the GMR with (a) the low resistive state and (b) the high resistive state.

The GMR can be described by spin accumulation induced at the interfaces resulting from spin-polarized currents and spin-dependent conductance in a ferro-

magnet. Consider a flow of electrons moving from one ferromagnet into a metallic spacer and subsequently into a second ferromagnet. In a metallic ferromagnet the band structures are spin-dependent. The density of states at the Fermi level is different for majority spins and minority spins, and so the conductance of electrons in each spin state is different, causing any current flowing in the ferromagnet to be spin-polarized. As these electrons move into the normal metal they will retain their spin-polarization for a time called the spin-flip relaxation time. Given the Fermi velocity of the electron, this corresponds to a spin flip length for which the polarization will be conserved in the normal metal. The GMR can be explained as due to spin-dependent scattering at the interface with the second ferromagnet. If the second ferromagnet is magnetized anti-parallel to the spin-polarization direction a spin-flip at the interface is required for the electron to enter the ferromagnet as once again the bands are spin-dependent. If the electron is not able to spin-flip due to scattering by a defect, its entry into the second ferromagnet is impeded, and it can be reflected at the interface. This gererates a spin accumulation and results in a resistance increase. On the other hand, if the second ferromagnet is aligned with the spin of the conduction electrons, a spin flip is not required and the electron can pass into the ferromagnet easily, inducing a low resistance state. Therefore, the GMR amplitude depends on the relative orientation of the ferromagnetic layers on both sides. The resistance can be quantitatively calculated taking into account the exact spin accumulation at the interfaces as in reference [21]. The GMR value is then given by:

$$GMR = \frac{R_{ap} - R_p}{R_p} \tag{1.12}$$

where R_{ap} is the electrical resistance in the anti-parallel state and R_p in the parallel state. The GMR effect can reach several tens of percent at room temperature. It is presently exploited in the read heads of hard disks to electrically measure the relative orientation of the magnetic grains on a hard drive platter that represent bits.

1.1.2.3 Tunnel magnetoresistance

The tunnel magnetoresistance (TMR) occurs when the normal metal spacer between two ferromagnetic layers is replaced by an insulating tunnel barrier (thus a F/I/F structure). As for the GMR effect, we can consider different spin conductances but this in the tunnelling regime. The splitting of the spin dependent band structure can indeed be very important and electrons can tunnel if they have available energy levels on the other side of the barrier[22, 23, 24]. The TMR is defined in the same way as for GMR by :

$$TMR = \frac{R_{ap} - R_p}{R_p} \tag{1.13}$$

where R_{ap} is the electrical resistance in the anti-parallel state and R_p in the parallel state. TMR effects reach up to 600% at room temperature (in MgO barriers where the effect is enhanced because of wave functions filtering by symmetry). The TMR effect is used in the most modern read heads of hard disks and is the basis for MRAMs, i.e. non-volatile memories.

1.1.2.4 Domain wall resistance

A domain wall is a region in space of a magnetic material where magnetization changes are fast. Because of the magnetic nature of the material its resistance has an AMR component which changes in a DW. Moreover, a extra resistive contribution comes from spin scattering. If the DW is large then electron' spin trajectory crosses the DW purely adiabatically. If the width is very small, we obtain the GMR effect as the spin passage is sudden. For intermediate widths the spins see a changing effective magnetic field during its passage. Viret et al. [25] and later Levy et al. [26] have demonstrated that the domain wall resistance (DWR) due to spin scattering can be expressed as:

$$DWR = \frac{2p}{(1-p)^2}\left(\frac{2\pi\hbar v_F}{E_{exc}\Delta}\right)^2 \tag{1.14}$$

where v_F is the Fermi velocity, E_{exc} is the exchange energy, p represents the asymmetry of spin scattering in the ferromagnetic material and Δ the width of the domain wall. So the DWR depends on the square of the magnetization gradient. In figure 1.6 we show locally the two contributions of AMR and DWR in a vortex wall. Depending on the domain wall and the material, the main contribution can be of DWR or AMR origin.

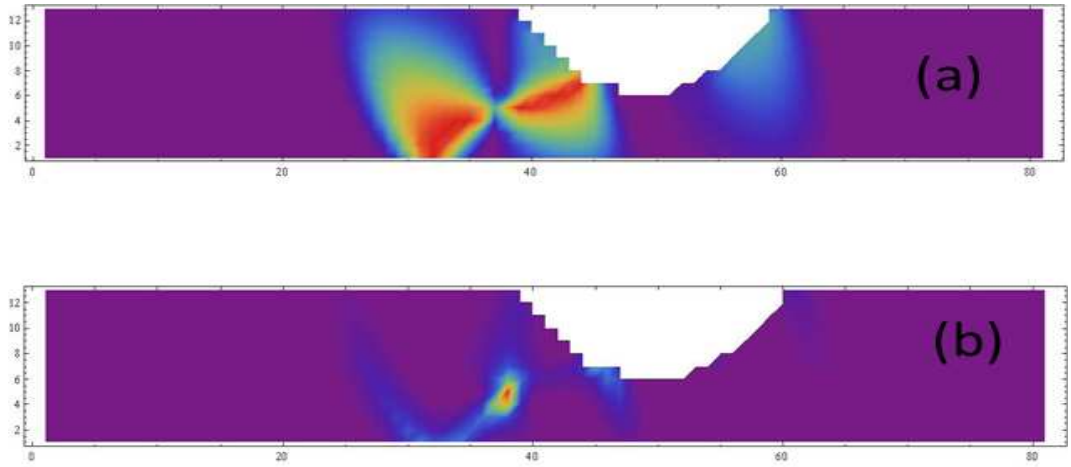

Figure 1.6: Level mapping of the resistance of the domain wall with (a) the AMR contribution and (b) the DWR due to spin scattering for a vortex wall. In both cases purple is for no change on the magnetoresistance and red maximum influence in absolute value (DWR increases the magnetoresistance and AMR decreases it).

1.2 Magnetization dynamics

In the previous section we have given a concise description of static ferromagnetism. Here, the basics of magnetic resonance are tackled and more specifically the ferromagnetic resonance.

1.2.1 Quantum origin

Quantum mechanism establishes that the evolution of the magnetic moment $\vec{\mu}$ of a particle in an applied uniform magnetic field $\vec{B}$ is given by

$$\frac{d}{dt}\vec{\mu}(t) = \frac{1}{i\hbar}\left[\vec{\mu}, \mathcal{H}\right] + \frac{\partial\vec{\mu}}{\partial t} \tag{1.15}$$

The hamiltonian $\mathcal{H}$ to be considered is the Zeeman one and the magnetic moment is a constant of motion $\frac{\partial\vec{\mu}}{\partial t} = 0$. Hence, the equation of evolution of the magnetic moment is given by:

$$\frac{d}{dt}\vec{\mu}(t) = -\frac{gq}{2m}\vec{\mu}(t) \wedge \vec{B}(t) \tag{1.16}$$

where q is the charge, m the mass of the particle and g the dimensionless Landé factor. In the case of an electron in an atomic electronic cloud, this factor depends on both orbital and spin moments. For example, a free electron (i.e. with no orbital moment and a 1/2 spin) has g=2 in a good approximation. In the case of a ferromagnetic metal, the magnetic moment is almost entirely due to spins as the total orbital moment is almost zero. The obtained Landé factors in these materials are only slightly higher than the value for free electrons. The magnetic moment precesses then along the applied magnetic field $\vec{B}$. For an electron the gyromagnetic factor γ is given by

$$\gamma = \frac{ge}{2m_e} = \frac{g\mu_b}{\hbar} \tag{1.17}$$

where μ_b is the Bohr magneton and $\hbar$ the reduced Planck constant. For a free electron, g is equal to 2 and so $\gamma/2\pi \cong 28$ GHz/T.

1.2.2 Ferromagnetic resonance

In a ferromagnet only the electronic spin moments contribute to the total magnetic moment as the orbital one is blocked by the bonds between the atoms. There can be two types of precessions: a uniform one when the spins are all in phase, and a non uniform one when there is a phase between neighboring spins.

1.2.2.1 Uniform mode

In a ferromagnetic material, the effective magnetic field H should account for all the energy terms of part 1.1.1. The magnetization $\vec{M}$ is defined by

$$\vec{M} = \frac{\sum \vec{\mu}}{V}$$

and so its motion is given by the Landau Lifshitz equation:

$$\frac{d}{dt}\vec{M}(t) = -\gamma\mu_0 \vec{M}(t) \wedge \vec{H}(t) \tag{1.18}$$

An interesting property of this equation 1.18 is the conservation of the magnetization norm (it can be verified by projecting both sides of the equation along $\vec{M}$. A notable fact is that this equation does not take into account energy losses. Gilbert added a phenomenological term in this equation to take into account the coupling to the external world which induces a relaxation of the magnetization to equilibrium. The Landau-Lifshitz-Gilbert equation is given by:

$$\frac{d}{dt}\vec{M}(t) = -\gamma\mu_0 \vec{M}(t) \wedge \vec{H}(t) + \frac{\alpha}{M_s}\vec{M} \wedge \frac{d\vec{M}}{dt} \tag{1.19}$$

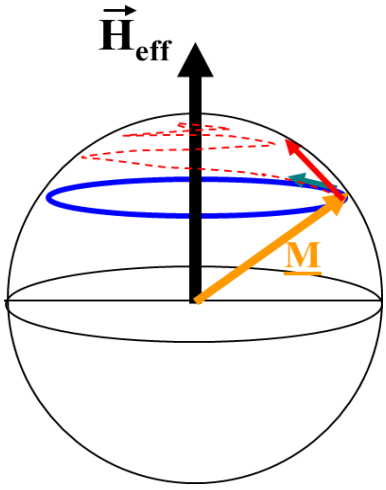

Figure 1.7: Schematics of the precession with the Gilbert damping term in red

where α is called the Gilbert damping coefficient. A way to put the system in precession is to irradiate it with a rf magnetic field $\vec{h}$. Then the magnetization will change at this frequency, $\vec{M}(t) = \chi * \vec{h}$. We can calculate this susceptibility χ for an ellipsoide where the demagnetization factors are constant, in the macrospin model where all spins can be considered to form a unique macro spin. The magnetization

and the applied static magnetic field H_0 are both aligned along x. The rf field h_{rf} is perpendicular to this axis.

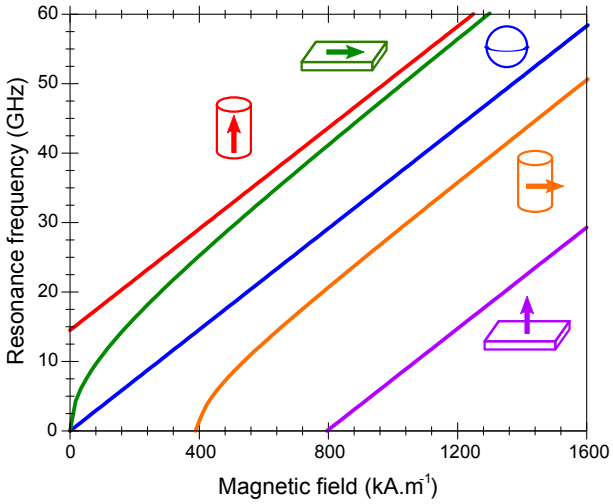

Figure 1.8: Shape influence on ferromagnetic resonance frequencies ($\gamma/2\pi = 28\text{GHz/T}$ and $\mu_0 \text{M}_\text{S} = 1\text{T}$)

The Landau-Lifshitz-Gilbert is not a linear equation, but in the case of small precession angles it can be linearized. As only a uniform precession is considered, the exchange field can be neglected in calculations (all spins are aligned) despite its key role in keeping the magnetization precession uniform. Magnetocristaline anisotropy is also neglected because only random micro-cristalline materials were used during this work. In the following, uppercase H and M_S mean respectively static magnetic field and static magnetization, whereas lower case h and m mean dynamic (time dependent) magnetic field and magnetization. The subscript D means demagnetizing. Both static and dynamics magnetic fields are the sum of applied and demagnetizing fields:

$$\begin{aligned} \vec{H} &= \vec{H}_0 + \vec{H}_D \\ \vec{h} &= \overrightarrow{h_{rf}} + \vec{h}_D \end{aligned}$$

So keeping only linear terms in $\overrightarrow{m}$ and $\overrightarrow{h}$, in the case of forced oscillations, Landau-Lifshitz-Gilbert equation becomes:

$$\frac{d\overrightarrow{m}}{dt} = -\gamma\mu_0 \vec{m} \wedge \vec{H} - \gamma\mu_0 \vec{M}_s \wedge \vec{h} + \alpha \frac{\vec{M}_s}{M_s} \wedge \frac{d\vec{m}}{dt} \tag{1.20}$$

with for the time dependent terms:

$$\begin{aligned} \vec{m}(\vec{r};t) &= \vec{m}(\vec{r})e^{-i\omega t} \\ \vec{h}(\vec{r};t) &= \vec{h}(\vec{r})e^{-i\omega t} \end{aligned} \tag{1.21}$$

and, $\vec{M_s}$ is the static part of magnetization here approximated to be the saturation magnetization in the case of linear dynamics, and $\gamma\mu_0 = \gamma_0$. For the demagnetization field we will consider an ellipsoid with so a diagonal demagnetization factor. The magnetic field $\vec{H}_0$ is applied along the axis X and equilibrium magnetization is also along this axis. The rf field $\overrightarrow{h_{rf}}$ is in the plane (y,z).

Thus equation 1.20 can be written in tensorial form:

$$\begin{pmatrix} h_y \\ h_z \end{pmatrix} = \frac{1}{\omega_M} \begin{pmatrix} \gamma_0 \left[H_0 + (N_y - N_x)M_s\right] - i\alpha\omega & i\omega \\ -i\omega & \gamma_0 \left[H_0 + (N_z - N_x)M_s\right] - i\alpha\omega \end{pmatrix} \begin{pmatrix} m_y \\ m_z \end{pmatrix} \tag{1.22}$$

where:

$$\omega_M = \gamma\mu_0 M_s$$

The ferromagnetic susceptibility tensor χ is the inverse of the previous tensor. Indeed it is defined as:

$$\begin{pmatrix} m_y \\ m_z \end{pmatrix} = \chi \begin{pmatrix} h_y \\ h_z \end{pmatrix} \tag{1.23}$$

$$\tag{1.24}$$

It is important to note that precession can become nonlinear when the precession angle is large enough or when h is larger than the static magnetic field H. Non linear precession can lead to dramatic effects like magnetization reversal. Expressing nonlinear precession resonance requires to solve the full nonlinear equation 1.19 .

This leads to the following ferromagnetic susceptibility :

$$\chi = \frac{\gamma_0 Ms \begin{bmatrix} \gamma_0 \left[H_0 + (N_z - N_x)M_s\right] - i\alpha\omega & -i\omega \\ i\omega & \gamma_0 \left[H_0 + (N_y - N_x)M_s\right] - i\alpha\omega \end{bmatrix}}{\omega^2 - (\gamma_0 \left[H_0 + (N_z - N_x)M_s\right] - i\alpha\omega)(\gamma_0 \left[H_0 + (N_y - N_x)M_s\right] - i\alpha\omega)} \tag{1.25}$$

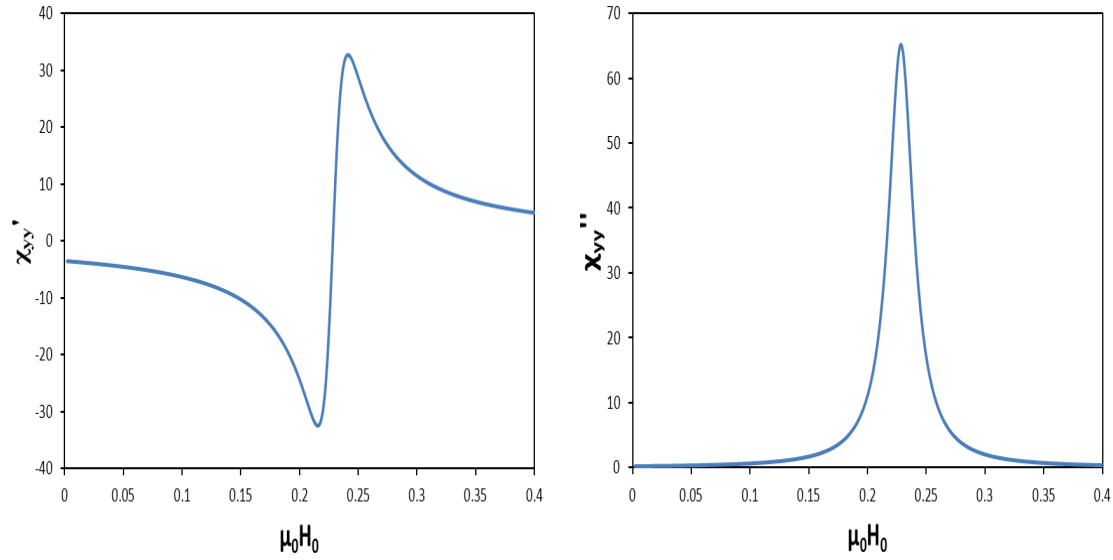

Figure 1.9: Real χ'_{yy} and imaginary χ''_{yy} parts of the susceptibility χ_{yy} in the case of a stripe with N_x=0.001, N_y=0.008, N_z=0.991, $\mu_0 M_s = 1T$,$\alpha = 0.024$, $\gamma/2\pi = 28GHz/T$ and with a rf frequency of 15 GHz

Only y and z components are written here because the linear dynamics occurs in this plane perpendicular to the static magnetization $\overrightarrow{M}_S$ (assumed to be along x-axis). This is why components of the susceptibility tensor related to the x-axis are zero.

The y and z components are not the same when the related demagnetization factors are different, this implies that the precession trajectory is not a circle as for a free spin, but it has an elliptical shape. Indeed, equation 1.25 allows one to calculate the ellipticity factor $\frac{m_y}{m_z}$.

Another interesting consequence of equation 1.25 is the calculation of the resonance frequency. When $\chi \xrightarrow{\alpha \to 0} \infty$ i.e. $\det\left[\chi^{-1}\left(\alpha = 0\right)\right] = 0$, the resonance is established. So the dispersion law (known as the Kittel formula) giving the frequency and the corresponding magnetic field to fulfill the resonant condition, can be expressed(resonances dispersion law of most usual elliptic shapes are plotted on figure 1.8):

$$\omega_r = (\gamma_0)^2 \sqrt{(H + (N_z - N_x)M_s)(H + (N_y - N_x)M_s)} \tag{1.26}$$

One should also notice that the ferromagnetic susceptibility is complex $\chi = \chi' + i\chi''$, the real part χ' corresponds to the magnetization in phase with the rf field and the imaginary part χ'' is out of phase. In figure 1.9 we represent the real

and imaginary parts of χ_{yy} in the case of a stripe with N_x=0, N_y=0.008, N_z=0.991, $\mu_0 M_s = 1T$,$\alpha = 0.02$, $\gamma/2\pi = 28GHz/T$ and a frequency of 15 GHz(It correspond to the parameter found in part 4 on the thin sample).

Another feature must be noted about this uniform mode: as in real systems finite dimensions make the amplitude not being uniform in the entire ferromagnet, this amplitude is lower in the border when the device is not a pure ellipsoid (e.g. a thin stripe). However, we will keep talking of uniform mode when all the spins precess in phase and the macrospin model gives a good description of this mode of resonance.

1.2.2.2 Non uniform resonance

As mentioned already, there exist other modes of resonance in ferromagnets where neighboring spins possess a slight phase between them. In that case the calculation of the susceptibility is far more complicated (see reference [27, 28] for some example) as the demagnetization tensor is not constant in the structure. The demagnetization factor should be simulated locally, taking account of the entire structure with its exact shape. All these modes are spin waves modes. They can also be enhanced if the rf magnetic field is not completely uniform. In our case the rf magnetic field is generated by a wire so its value varies with the distance to the wire (see next part). The rf current is homogeneous in the final wire so the rf field is given by the formula of Ampere:

$$B = \frac{\mu_0 I_{rf}}{2\pi(d + 1.5 * 10^{-6})} \tag{1.27}$$

where d is the distance to the border of the antenna and 1.5 μm is half of the antenna wire width. The part nearest to the antenna sees have typically 25% more rf field than the farthest one. This will promote the excitation of spin waves along the stripes width. The precession amplitude in the width varies as:

$$A_n \cos(k_n y) \tag{1.28}$$

(y=0 is the center of the ferromagnetic stripe, $k_n w/2$ is near zero and n=1 is the uniform mode) from reference [10, 28]. Due to the inhomogeneous rf field even modes with zero average dipolar moments can indeed be excited the energy given by the rf field being not zero.

In general non uniform modes are at higher energy, which translates into higher frequencies at a given static magnetic field or a lower field for a given rf frequency. In the case of a stripe, the static field along the ferromagnetic stripe (supposed to be infinite i.e. $N_x = 0$) has the following shape:

$$\mu_0 H_n - \mu_0 H_{n+1} = \frac{\mu_0 M_s t \pi}{2\sqrt{1 + 4\omega/(\gamma \mu_0 M_s)}} \frac{1}{w} \tag{1.29}$$

with w the width of the stripe and t the thickness.

Depending on the excitation system and its detection [29, 10], one could enhance, extinguish, detect different modes. For the techniques used in this thesis work, the uniform mode gives the highest signal. So we concentrate on the highest signal mode but accept the possibility to detect modes that are not the uniform ones (see part 4.2.2.3 for example).

1.3 Atomic contacts

In atomic contacts, magnetic atoms are in a low dimensional state which can be quite different from the bulk situation. In particular, the orbital moment can be recovered. Thus both electrical and magnetic properties of atomic contacts depend on the contact geometry and the nature of the atoms. In this chapter, we will first recall the basics of ballistic transport and then, in a second part, the magnetic properties of atomic contacts.

1.3.1 Electrical resistance

Historically, conductance quantization has been measured and understood first in 2D gases where Fermi wavelengths are large. In metals where the Fermi wavelength is of 2 Å, one needs to reach atomic dimensions in order to observe such effects. In atomic contacts sizes of a few angstroms are low enough to preserve the phase coherence. Indeed as electronic transport is ballistic, the conductance G is quantized with the number of electric conductance. In 1965 Sharvin [30] explained with the semi-classical theory that the problem is similar to movement of diluted gaseous molecules through a small hole. In that case the conductance G does not depend on the length of the contact and is determined by:

$$G = \frac{2e^2}{h}(\frac{k_F a}{2})^2 \tag{1.30}$$

where a is the radius of the contact and k_F the Fermi wave vector. When dimension of contact are really low the Sharvin conductance is no more correct as it does not take into account of quantum interference. In that case, the conductance is then given by the Landauer formula:

$$G = \frac{e^2}{h}\sum_{(k,\sigma)} T_{k,\sigma} \tag{1.31}$$

where the sum is on the electrical channels k and the spin σ(up or down) and T is the transmission of the channel between 0 and 1. The quantity

$$G_0 = \frac{e^2}{h} \tag{1.32}$$

is the quantum of conductance and it corresponds to a resistance of about 25800 Ω. In atomic contacts the number of channels is roughly given by the number of valence electrons, i.e. twice the number of bands crossing the Fermi level. For example in Au atomic contacts, only the s band (with two electrons of opposite spins) conducts and its transmission is one so the conductance of a Au atomic wire is 2 G_0. Scheer et al.

in 1998 [31] have measured that in an atomic contact of Al there are three channels with different conductances given rise to a full conductance close to 2 G_0. This is now well understood [32] and systematic measurements for various non magnetic elements have been performed [33]. This quantization of the electric conductance is observed for cross sections of several atoms.

1.3.2 Magnetism and atomic contacts

1.3.2.1 Magnetoresistance

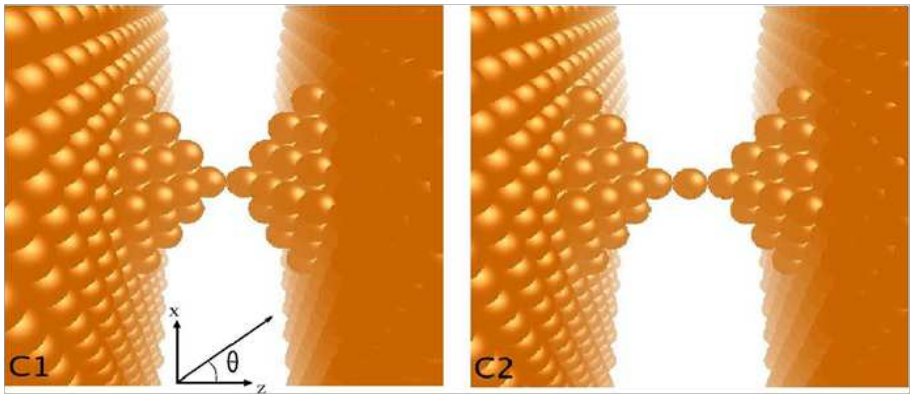

Figure 1.10: Two realistic contact geometries in iron [2] illustrating the importance of the locale dimensionality. On the left, two *half atoms 1D* (they have 3 neighbours in one side) and only a tiny AMR is generated from the contact. On the right, the central atom in a purely 1D configuration and the AMR can reach 50%

With magnetic materials the transmission coefficients depend on the spin because of spin orbit coupling. Thus it can be influenced by a magnetic field. The magneto resistance has been calculated *ab initio* for Ni,Co,Fe ideal wires [1, 34]. In the case of a Ni atomic wire the magnetoresistance goes from 7 G_0 to 6 G_0 when magnetization changes from transverse to longitudinal. This value of anisotropic magnetoresistance is much higher than in the bulk. It is due to a conducting channel passing through the Fermi level. In a more realistic geometry Autès et al. [2, 35, 36] have demonstrated the importance of the exact contact geometry (see figure 1.10) where one atom in a fully 1D geometry is essential for a large 'ballistic' anisotropic magnetoresistance. They also demonstrated that when a defect is introduced in an iron wire (in the form of a different distance between two atoms), the conductivity can change continuously from 7 G_0 to 0. Thus a pure quantification is only obtained in purely periodic systems and often, defects or scattering centers can significantly modify this property. Experimentally using the break junction technique it has been shown than the AMR can be increased greatly for contacts close, or even below, the

value for the conductance quantum [1]. Interestingly, it has been predicted that some 'border line magnets' like platinum would be magnetic in one dimension due to the recovery of its atomic orbital moment.

1.3.2.2 Domain walls in atomic contacts

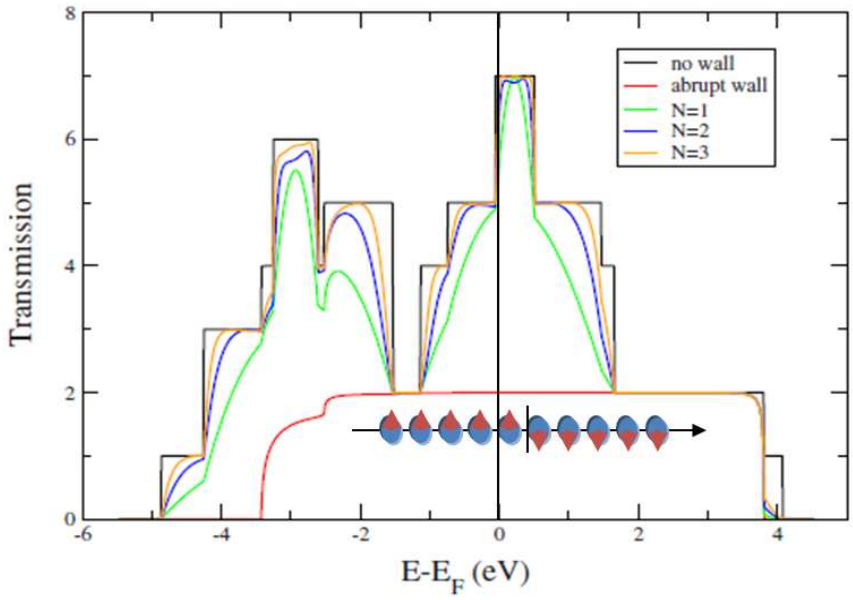

Figure 1.11: Transmission in G_0 for different domain wall widths (in number of atoms) versus energy from reference [36, 35] (the Fermi level is at the zero). The relevant quantity for transport is the transmission at the Fermi energy.

We have just stated that we need special configurations to obtain a large AMR in an atomic contact. One can wonder what happens to a domain wall in the atomic contact state. The references [35, 36] have calculated that in an ideal iron wire for an infinitely abrupt domain wall the conductance decreases from 7 G_0 to 2 G_0 (all 3d channels are closed). However, as shown in figure 1.11, when the size of the domain wall increase, its effect on the conductance is greatly reduced. The domain wall magnetoresistance in atomics contacts yields estimates in the 10% range. The increase of DW resistance has been observed experimentally in [3, 4]. It has to be noted that the sign of the domain wall contribution to magneto resistance has been observed to change compared to the bulk one from negative to positive (i.e. from AMR like to GMR like).

1.3.2.3 Magnetization dynamics

The dynamics of magnetization in such low dimensional materials has never been explored, probably because of detection sensitivity problems. Indeed, using inductive techniques, the signals scale with the samples volume. Thus, in order to probe the magnetic properties of a very limited number of atoms it is essential to find a measurement that amplifies their response. This can be achieved in a resistance measurement because current lines are forced through constrictions which can represent the greatest (series) resistance and hence dominate the potential drop. Atomic contacts can be magnetically very different from solids as the bonds between two atoms depend sensitively on the local geometry. Therefore all the usual magnetic parameters are redefined very locally: magnetization, dipolar field, Landé factor g and anisotropy. The only accurate magnetic object is the magnetic moment which is now a combination of the orbital moment (it is no more quenched) and the spin moment.

As a consequence, dynamical properties should be modified and a ferromagnetic resonance study of atomic contacts should provide key information regarding local magnetism. However, as FMR is a collective phenomenon to a magnetic excitation, the exact response is not easy to determine. Indeed the atomic contact is magnetically coupled to its bulk electrodes and local properties such as orbital moment or anisotropy would not show up in the simplest way. However, dynamical measurements should provide some of the basic information regarding magnetism in low dimension which cannot be accessed with static conductance measurements.

Chapter 2

Sample fabrication

2.1 Device conception

This part is devoted to a description of the design and elaboration of the antenna, which is a key element of the experimental work of this thesis. We will finally obtained the design of figure 2.5.

2.1.1 General conception

Before my arrival in the group, there was already a set up dedicated to studying mechanical break junctions (MBJ), see ref [3], but without the necessary wiring for radio frequency irradiation. For my thesis work, we need to produce a rf magnetic field. The easiest way to produce it is to pass an rf current through a metal wire, thus producing a magnetic field in virtue of Maxwell's equations. This radio frequency (rf) field is an Oersted field, it has a circular geometry and its direction is tangent to the circle around the wire. This magnetic field decreases in 1/r where r is the distance to the wire. So the magnetic material should be positioned as close to the antenna as possible figure 2.1a. An extra complication of the setup originates from the bending of the substrate and thus the wire that produces the rf magnetic field should not break before the junction of the sample. So we chose a width of 3 μm, much larger than the one of all the samples. In order to propagate a rf current to our wire we need to conceive a coplanar waveguide CPW (schemematic in figure 2.1b) adapted for the range of 10 MHz to 40 GHz. In this rf frequency domain, wavelengths are small enough so that we have to take into account possible reflections during the propagation (see part 2.1.2.1). For the dc contact on the sample there is no need as they are only dc measurements see figure 2.1c.

We also wanted to keep the same bending mechanism as before (see part 3.1.1) so the wire, the shorted end of the antenna (CPW + final wire), has to be parallel to the sample. The space allowed for the experiment in an electromagnet under

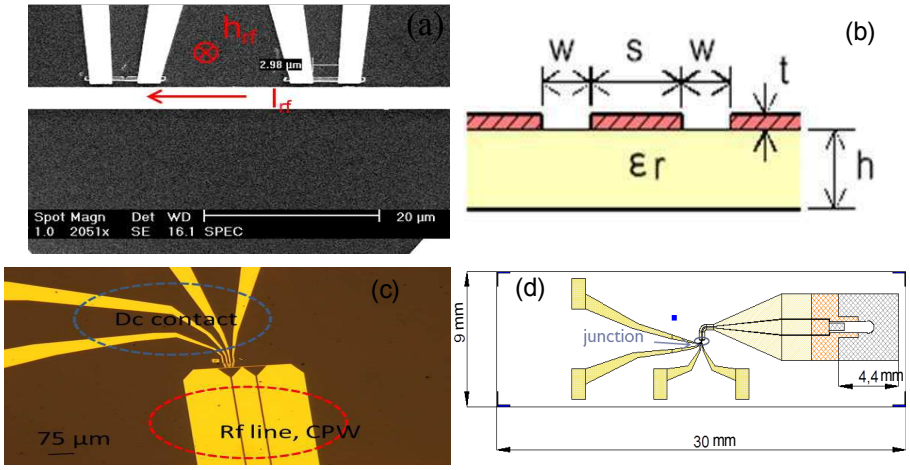

Figure 2.1: (a) SEM image of a wanted sample. (b) Schematics of a coplanar waveguide to propagate the rf excitation. (c) Two kinds of contacts: the rf line for the excitation of the dynamics and dc contacts to the sample (d) Schematics of the desired system

vacuum at 77 K is a cylinder of 5 cm diameter. The smallest rf connector is $1cm^2$, which allows a contact between a microfabricated antenna and mini-SMP rf cables. To avoid strain on the contact between connector and antenna, the connector should be at 1 cm of the final wire in the wire direction. The antenna will have four parts: the rf connector base, a reduction of the lateral dimension, an elbow and the shorted end. The dc contacts linked to the magnetic sample are them positioned in order to be used easily as shown on figure 2.1d.

2.1.2 Conception of the antenna

2.1.2.1 Propagation of a TEM signal

Amongst all the solutions of Maxwell's equations that rule the propagation of the signal, there is one which is a transverse electromagnetic (TEM) mode. For this mode both electric and magnetic fields are perpendicular to the propagation direction. This particularity provides to these fields a simple meaning into a two conductor waveguide (electric field stands for voltage and magnetic field is produced by electrical current in conductors). Indeed, such waves have electrostatic and magnetostatic distributions across the transverse plane. Therefore in a waveguide with TEM mode, a classical circuit model can be used. In coplanar strips and waveguides, two effects impede pure TEM modes. The first one is the finite conductivity of the metal used. It produces instead a longitudinal electric field. The second one

is the asymmetry of the insulating layer used above and beneath the waveguide. Fortunately, the propagating waves in these structures are quasi TEM mode. So they can be treated as TEM.

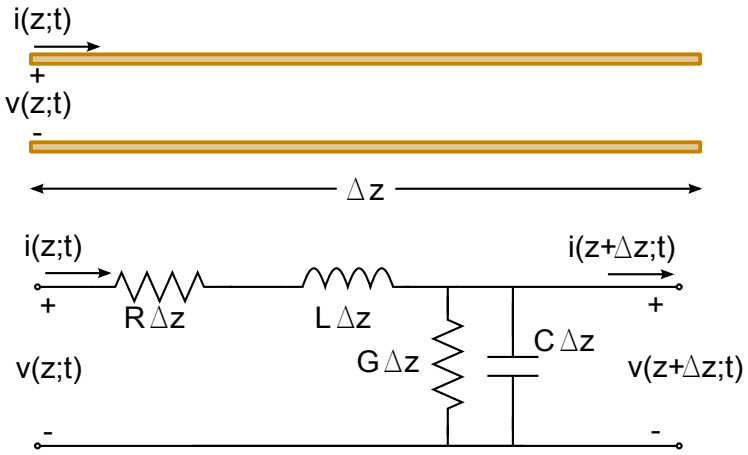

Figure 2.2: top: Wave guide – bottom: lumped element equivalent circuit (taken from ref [37] p. 50).

In figure 2.2 a schematic view of a small portion of a propagation line and its lumped element circuit equivalent are represented. This is possible as only TEM modes are considered. In this circuit, all R, L, G and C are quantities per unit length.

-R represents the losses by Joule effect in conductors ($\Omega.m^{-1}$).
-L stands for both conductors inductances ($H.m^{-1}$).
-G represents the dielectric losses of conductance in the insulator ($\Omega^{-1}.m^{-1}$).
-C is the capacitance due to the proximity of both conductors ($F.m^{-1}$).
According to Kirchhoff laws:

$$\begin{cases} 0 = v(z;t) - i(z;t)R\Delta z - \dfrac{\partial i}{\partial t}L\Delta z - v(z+\Delta z;t) \\ 0 = i(z;t) - v(z+\Delta z;t)G\Delta z - \dfrac{\partial v(z+\Delta z;t)}{\partial z}C\Delta z - i(z+\Delta z;t) \end{cases} \tag{2.1}$$

By passing to continuous equations, the previous system becomes:

$$\begin{cases} 0 = -\dfrac{\partial v(z;t)}{\partial z} - i(z;t)R - \dfrac{\partial i}{\partial t} \\ 0 = -\dfrac{\partial i(z;t)}{\partial z} - v(z;t)G - \dfrac{\partial v(z;t)}{\partial z}C \end{cases} \tag{2.2}$$

These equations are called telegrapher's equations. They describe both voltage and current in a transmission line as a function of distance and time. Let us now suppose that there are harmonic solutions and switch to frequency space:

$$\begin{cases} 0 = -\dfrac{\partial v(z;\omega)}{\partial z} - (R + Lj\omega)i(z;\omega) \\ 0 = -\dfrac{\partial i(z;\omega)}{\partial z} - (G + Cj\omega)v(z;\omega) \end{cases} \tag{2.3}$$

These two equations lead to:

$$\begin{cases} 0 = -\dfrac{\partial^2 v(z;\omega)}{\partial z^2} - (R + Lj\omega)(G + Cj\omega)v(z;\omega) \\ 0 = -\dfrac{\partial^2 i(z;\omega)}{\partial z^2} - (R + Lj\omega)(G + Cj\omega)i(z;\omega) \end{cases} \tag{2.4}$$

In the following of this part, the propagation constant γ will stand for:

$$\gamma = \alpha + j\beta = \sqrt{(R + Lj\omega)(G + Cj\omega)} \tag{2.5}$$

Solutions of these equations are the following:

$$\begin{cases} v(z;\omega) = V_0^+ e^{-\gamma z} + V_0^- e^{+\gamma z} & (2.6) \\ i(z;\omega) = I_0^+ e^{-\gamma z} - I_0^- e^{+\gamma z} & (2.7) \end{cases}$$

It appears clearly here that β represents the propagating part and α the losses (indeed when R and G are zero, i.e. when there are no losses, α is also zero). Terms in $e^{-\gamma z}$ are the forward propagating waves(+z direction). On the contrary, terms in $e^{+\gamma z}$ are the backward propagating waves (-z direction). When these solutions are injected in equations 2.3, Z_0, the characteristic impedance of the line is defined as:

$$i(z;\omega) = \frac{1}{Z_0} v(z;\omega) = \sqrt{\frac{R + Lj\omega}{G + Cj\omega}} v(z;\omega) \tag{2.8}$$

This impedance is seen both as the entrance and exit impedance as:

$$\frac{V_0^+}{I_0^+} = \frac{V_0^-}{I_0^-} = Z_0 \tag{2.9}$$

2.1.2.2 The transmission line

This impedance Z_0 depends on geometric and dielectric characteristics: the ratio between w and s (see figure 2.1), the dielectric constant of our kapton substrate $\epsilon_r = 3.2$, finite conductivity of the metal and vacuum properties. To simulate and

optimize our antennas we used the software Sonnet to calculate the dimension for a 50 Ω adapted CPW antenna. the software also took account of deviation from TEM modes. Due to fabrication limitations we chose a gap of w=4.75 μm for the propagation before the shorted end. Due to size and time of calculation we cannot simulate all the antenna, and thus we focused on propagation along a short ended line. Then we realized these small parts of antenna to measure their rf characteristics and compare with the simulation. To do so we used a vectorial network analyzer (VNA).

A VNA has in general two input/output ports called port 1 and port 2. Each port can produce a signal and measure what it receives. The port 1 emits a monochromatic rf voltage u1 in the measured device. In the device, a part of the signal is transmitted and measured with its phase shift on port 2, an other part is reflected on port 1. This determines the coefficients S_{21} and S_{11} of the scattering matrix S. Inversing the function of the two ports gives us the two other coefficients of the S matrix. There are other parameters than the scattering matrix to characterize rf devices, but you can pass from one to another [37]. To avoid errors in measurement due to probe or internal VNA reflections, first a calibration step with known impedances is carried out. This protocol consists in plugging in four reference devices instead of the network to study. In this work these reference devices were, open, short, 50 Ω load and 50 Ω through line.

Figure 2.3 shows measurement and simulation for a propagation line with a gap of 4.75 μm and 75 μm for the central part. The dimension 75 μm correspond to a 50 Ω CPW with a gap of 4.75 μm on a substrate with a permittivity as the one of kapton. The measured velocity 2.00 $10^8 m/s$ is only a little lower than the one simulated. The main difference is that there is more losses due to the real resistance of the line. Indeed Sonnet was used in 2D mode and did not take account of the thickness.

For the asymmetric shorted end, here too simulations and measurements are in good agreement see figure 2.4. The role of the asymmetry is to increase the antenna's life time. Indeed the part of symmetric antennas with no magnetic device in front of it is easier to be destroyed by the rf power.

Finally the antenna mask is designed as in figure 2.5. It is fabricated using optical lithography. On the same layer, we added the design for the large scale contacts to the sample in order to save time for the fabrication process.

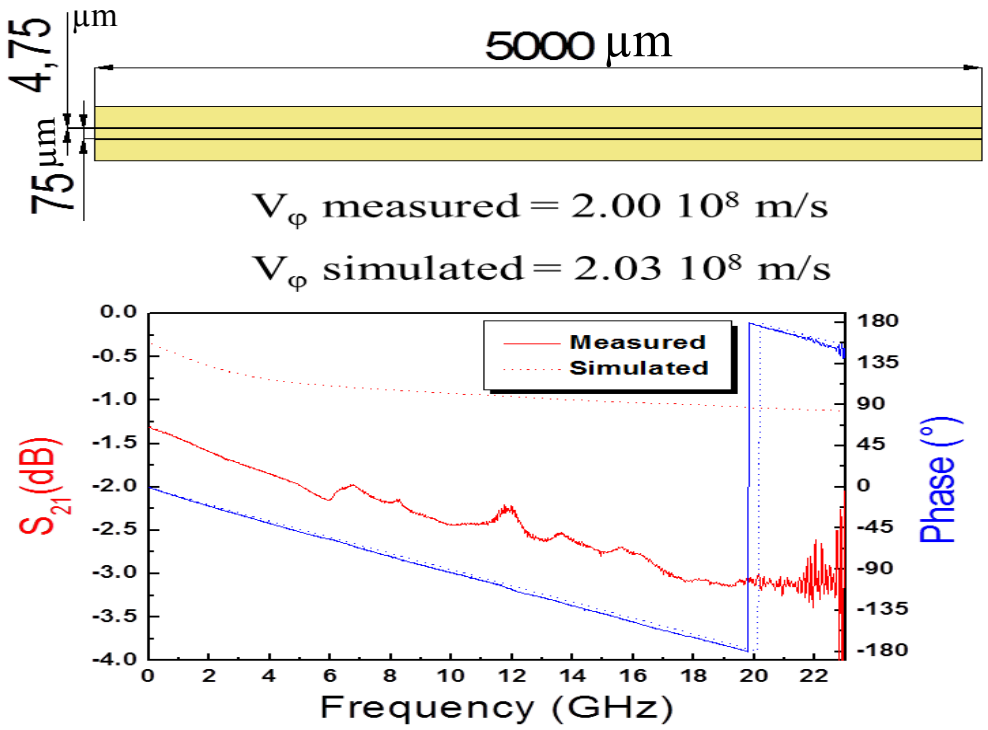

Figure 2.3: A 50 Ω transmission line with both measurement and simulation of the transmission coefficient versus frequency.

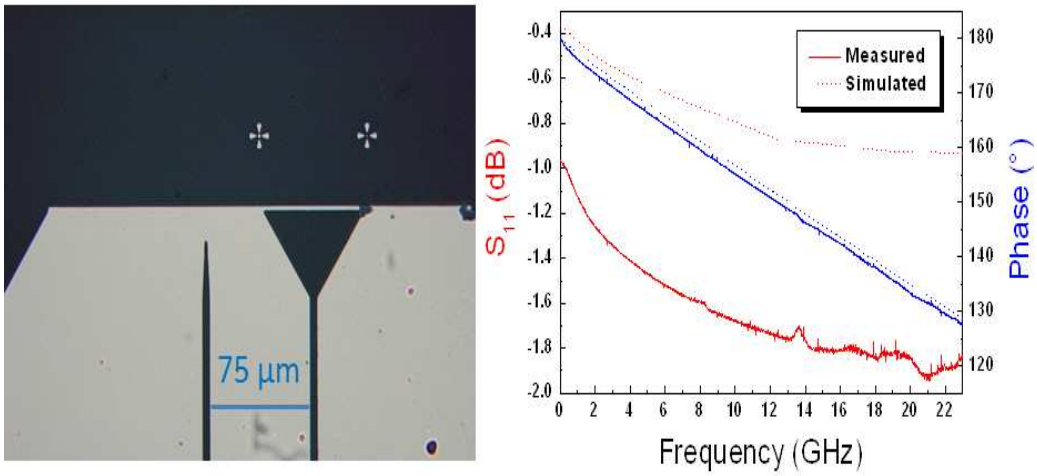

Figure 2.4: An asymmetric shorted end with both measurement and simulation of reflection coefficients.

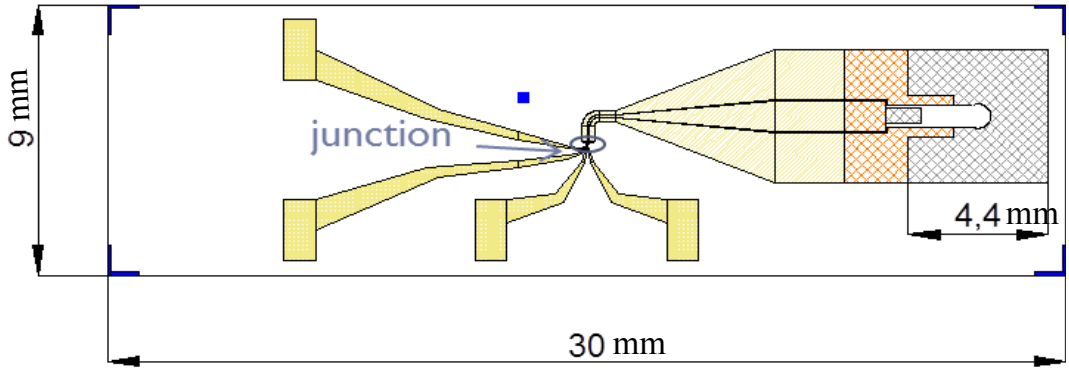

Figure 2.5: Image of the optical mask for an antenna. In gray is the area in contact with the connector.

2.2 Samples fabrication

We realize our samples in three main steps: the preparation of the substrate, the realization of the antenna, and the magnetic specification. This last step is specific for each sample. Most of the techniques used to fabricate the samples during this thesis are standard techniques. However the preparation of the plastic substrate deserves some descriptions. For coherence, we give in this part all the processes used to fabricate our samples.

2.2.1 Preparation of the substrate

The substrate is an insulating plastic material, a 500 μm-thick kapton (kapton HN from DuPont). As bought, the kapton is too rough and has too many scratches to allow the fabrication of good rf antenna on it, the natural roughness of the substrate being around 10 μm with local scratches even deeper. Kapton plates are cut into 2 inches wafers. So the first step consists in polishing the kapton. Kapton wafers are polished three by three using a polisher P320 MECAPOL from PRESI. First the wafers are glued with wax on a large metallic block. During the different steps of polishing we change the roughness of the polisher disks, the diamond paste and the number (1 or 2) of metallic blocks. For example:

-9 μm 2 blocks during 10 min at 140 rpm

-9 μm 1 block during 10 min at 140 rpm

-6 μm 1 block during 5 min at 140 rpm

-3 μm 2 blocks during 3 min at 140 rpm

-3 μm 1 block during 3 min at 140 rpm

-1 μm 2 blocks during 3 min at 140 rpm

-1 μm 1 block during 3 min at 140 rpm

After the polishing stage, we obtain a mirror polished substrate as in figure 2.6, where the roughness is less than 10 nm over 25 μm areas. Flatness of the surface is then improved by spinning a polyimide layer. As a first layer we spin a solution of PI2611 (HD MicroSystem) 30 g with 30 g of NMP(N-methyl-2-pyrrolidone) at 4000 rpm during 90 s terminated by 3 s at 6000 rpm and finally baked 60 s on the hot plate at 140°C. This first layer allows us to better spin the more viscous second layer. This second layer is a solution of pure PI2610 spun at 2000 rpm with 3s at 4000 rpm to limit edge effects. The wafer is then baked at 180 °C during 1 hour in an oven and then cured for 1 hour at 350 °C in a vacuum chamber with a residual pressure of 10^{-6} mbar. The final thickness of the polyimide layer is typically 3 μm. The local roughness is below 3 nm over 25 μm and most of the scratches are filled.

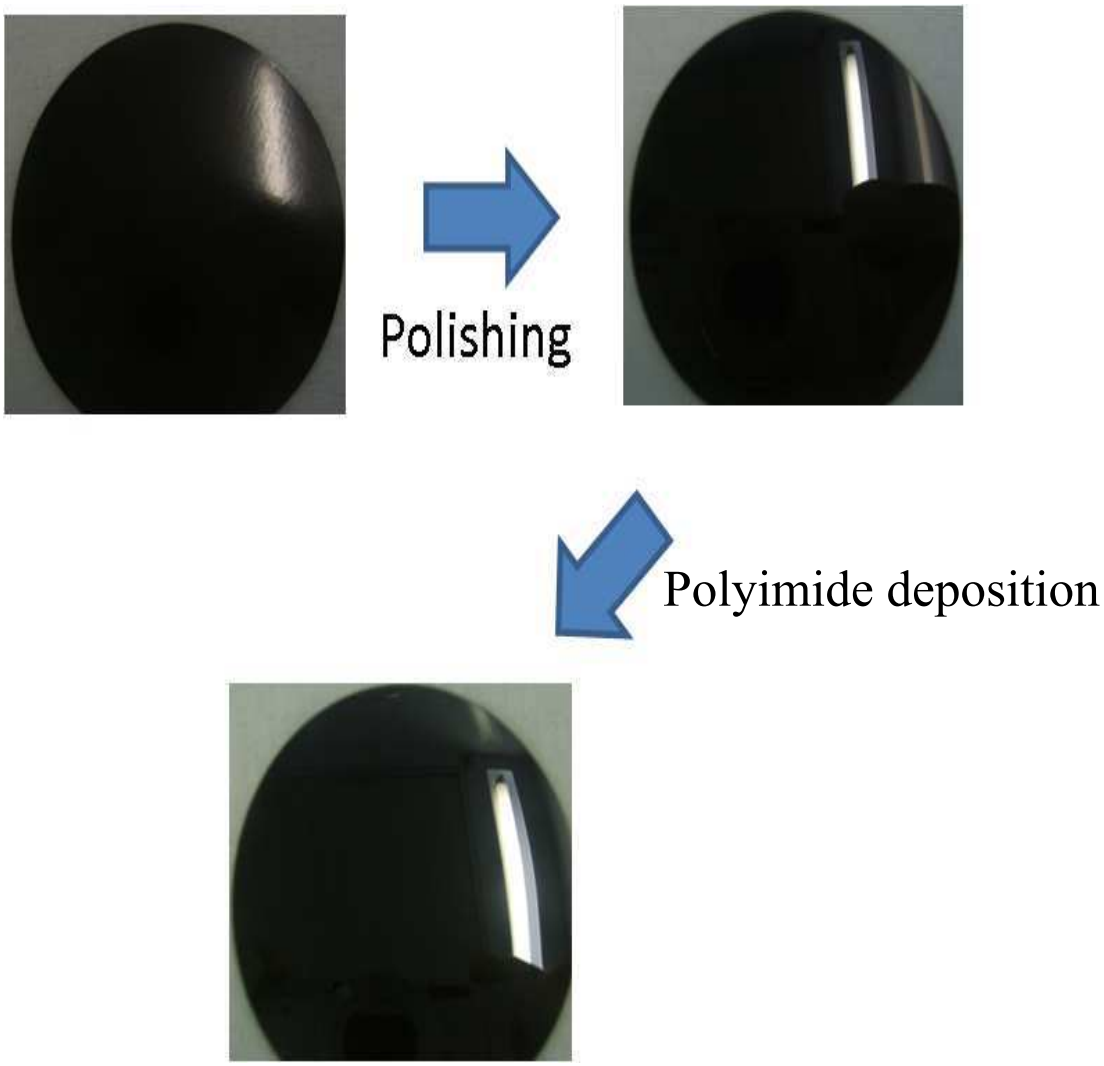

Figure 2.6: Images of a 2 inch kapton wafer at different steps of the substrate preparation.

2.2.2 Fabrication of the antennas

The antennas are realized using optical lithography, metal deposition and lift off techniques. Six antennas, following the design obtained in part 2.1.2, are optically lithographed on a kapton wafer, hence giving 6 samples per wafer. We get three symmetric short end antennas and three asymmetric short end antennas per wafer see figure 2.7. Prior to the main optical resist deposition, a resit to help for the lift off process (LOL) is first spun. The LOL2000 of Shipley is filtered, spun at 3000 rpm during 60 s, baked during 5 min on a hot plate at 155 °C resulting in a

thickness of 200 nm. Filtered Shipley resist S1805 is then spun at 4000 rpm during 60 s, baked at 115 °C during 5 min on a hot plate resulting in a thickness of 400 nm.

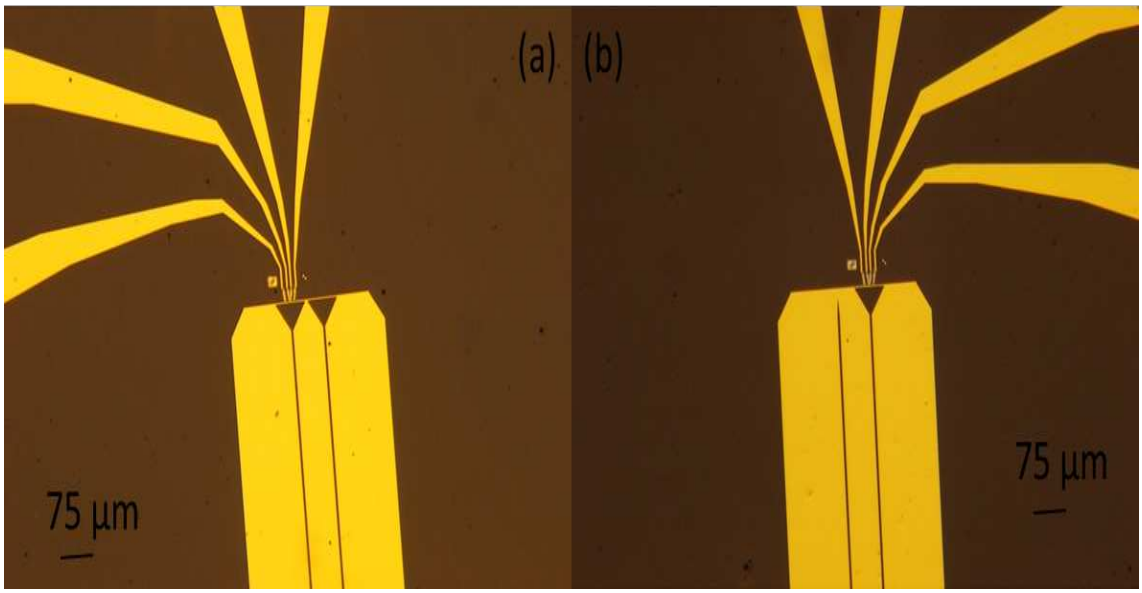

Figure 2.7: (a) optical image of the shorted end of a symmetric antenna and (b) of an asymmetric antenna.

The exposure is realized in UV lithography with a MJB3-SUSS Aligner. The power density of the lamp is 5 $mW.cm^{-2}$. The lamp is a Hg lamp not filtered so all UV wavelength of Hg are preserved. The obtained resolution is around 1 μm and the exposure is through a chromium mask. As the resist is a positive resist the antennas are the holes in the mask. Therefore patterning is done by transferring the mask. The exposure time is 10.5 s. The wafer is developed using MF-319(Shipley): 30 s and after dipped 30 s in deionized water.

Before the metal deposition, a 10 s ion milling is performed to clean the surface and insure a better contact. The metal layer is deposited with an e-beam evaporator. A beam of electrons is focused on a crucible of the targeted material, which is hence heated, melted and so a small vapor pressure of the material is emitted. This vapor condensates on the wafer and on a calibrated quartz balance to measure the obtained film thickness. The residual pressure is typically of 10^{-7} $mbar$. Considering the target-sample distance, this technique is quite directional, and the obtained layer has a low defect density as the atoms are deposited with a low kinetic energy. Our antennas are in two layers: Ti 5 nm to stick to the substrate and Au 140 nm. Au is to avoid oxidation of the antenna with good conducting properties and the 140 nm thickness is used in order to tolerate high rf current densities therefore increasing the lifetime of the antenna. After the metal deposition, the resist with

LOL2000 is removed in hot remover 1165 (Shipley) during 5-10 min. We then obtain wafers like that shown in figure 2.8.

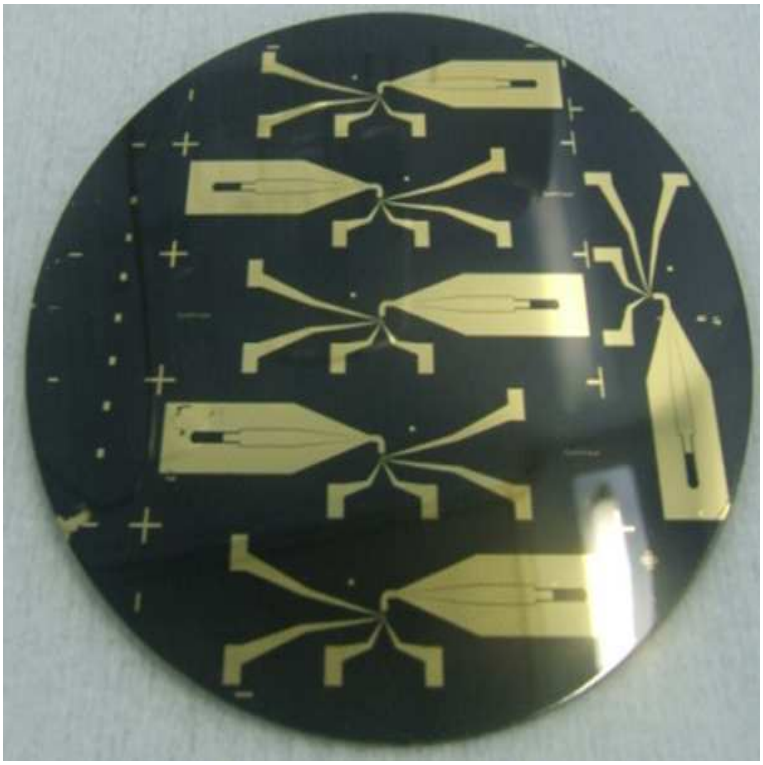

Figure 2.8: Optical photography of a 2 inch wafer after the fabrication of the antennas.

2.2.3 Magnetic specification

After cutting the wafer into 30 mm×9 mm samples, the magnetic part and their contacts are realized using e-beam lithography, metal deposition and lift-off techniques. A scanning electron microscope is used to expose the pattern of a mask on a positive electro sensitive resist.

The resist for e-beam lithography is in three parts. First a bottom layer of MMA(8.5)-MAA EL10 is spun at 5000 rpm during 60 s with 5 s at 6000 rpm to avoid edge effects and then baked 1 min at 170 °C on the hot plate. The typical thickness is 400 nm. Then a PMMA 950 A6 is spun at 6000 rpm during 60 s, baked for 15 min at 170 °C and has a thickness of 240 nm. The bottom layer is more sensitive to electrons and so is exposed on a larger surface by electron diffused by the substrate. This helps the lift off. As our kapton substrate is an insulator as well as the e-beam resists, we must add a layer to evacuate charges during the exposure. So above the

organic resit a thin layer of 6-8 nm of Al is deposited by e-beam evaporation (at a residual pressure of 10^{-6} mbar). The Al has an atomic number low enough for not influencing the pattern of the small structures at small current. The typical sensitivity of the resist is 250 $\mu C/cm^2$.

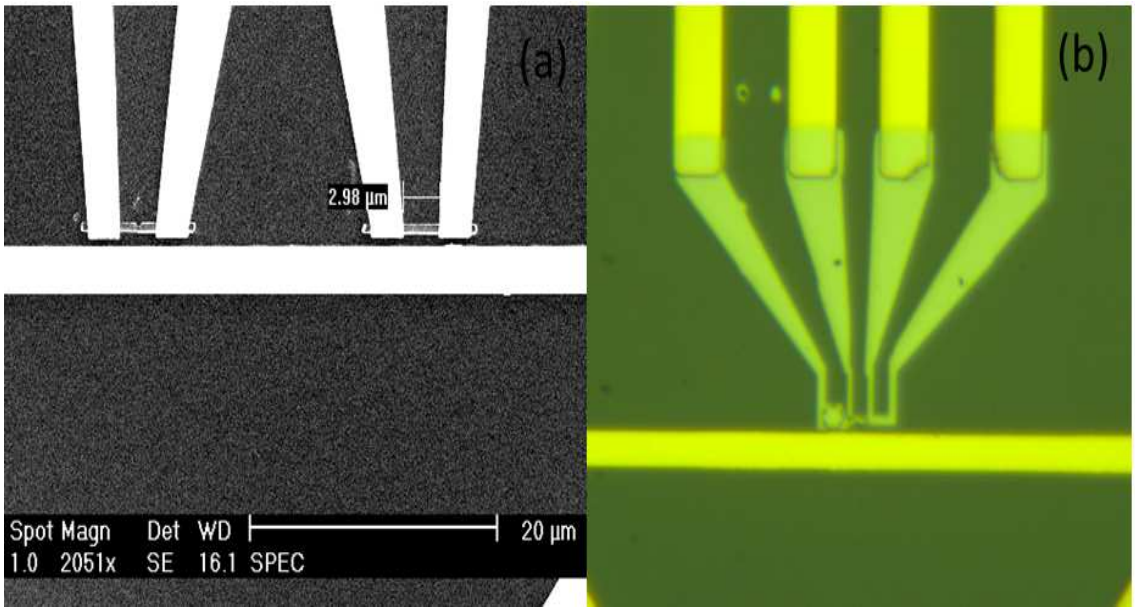

Figure 2.9: (a) SEM image of a sample for FMR measurements of a break junction and (b) optical image of a sample for ISHE measurements.

The e-beam lithography is a direct writing lithography with electrons as the pencil. A beam of electron is moved from pixel to pixel where it stays the dwell time to expose this pixel. When the area should not be exposed the beam is blanked. The main electrons for the exposure are the back scattered electrons. We used two different scanning electron microscope SEM, the first one was a JEOL JSM840 using PROXY^{TM} from Raith, and when it became unavailable we used a Philips XL30 SFEG microscope using Elphy Quantum from Raith. The current used was 10 or 25 pA as we only pattern small structures, big part of the contacts were already done during the optical lithography step. The resolution with our resist and exposure conditions is 50 nm and less than 100 nm precision for alignments. After exposure the Al layer is removed in a bath of KOH during 40 s then cleaned with isopropanol. Then the resist is developed in a bath of methyl-iso-butyl keton MIBK diluted 1:3 in volume with isopropanol for 45-50 s and after dipped 30 s in isopropanol. Due to the bilayer structure and the backscattered electrons the remaining resist has a *mushroom* appearance. This appearance allows to build suspended resist masks for exposure, although it is not essential in our case as our structures are simple enough. There are two steps of e-beam lithography one for the magnetic material and one

for the contact between the magnetic material and the optical gold contacts. The contacts between the two parts are in gold or platinum evaporated by e-beam. We deposit two kinds of magnetic material Co (with 1 nm of Ti below to stick on the kapton) by e-beam evaporation and permalloy $Ni_{80}Fe_{20}$(Py) by rf sputtering.

For the sputtering deposit in a high vacuum chamber ($10^{-7}mbar$), an Ar gas is maintained at 5.10^{-3} mbar pressure. It is ionized because of a RF field generated between a cathode and an anode at a frequency of several 10 MHz. Beneath the cathode, a series of permanent magnets is used to confine the plasma. On the cathode, a target (made of the material to deposit, e.g. Py) is positioned. The system composed of the cathode, the anode and the magnet is called magnetron. In operation, Argon ions crash on the target and extract atoms which are deposited on the sample following the rf circulating flow of argon so there is low directionality but it is very useful to deposit insulating materials. The non directionality broadens the lifted nanostructures compared to those obtained for evaporated materials. For the same e-beam lithography stage, the dimension of the pattern structure are typically increased by 120 nm with a sputtering lift-off compared to e-beam evaporation due to the *mushroom* profile. The remaining resist with its unwanted metal layer above is removed in the lift off process by a bath in hot acetone.

For inverse the spin-Hall effect (ISHE) samples of figure 2.9b the normal metal is below the ferromagnetic material (Py) in order to obtain one well defined interface for the spin pumping (see part 6.2.1). In the sample for FMR in low dimension the ferromagnetic part is under the contacts to have a plane ferromagnet see figure 2.9a.

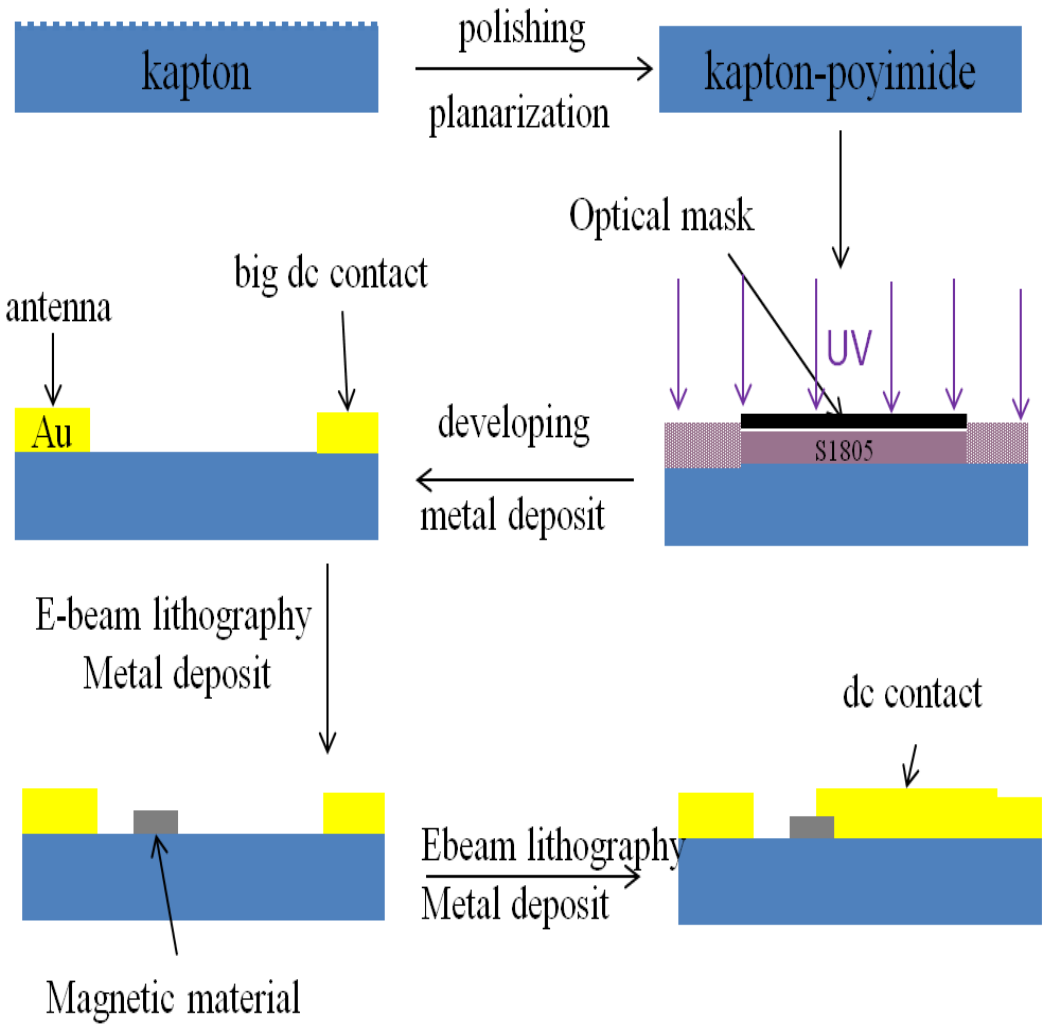

Figure 2.10: Schematics of the samples fabrication as in figure 2.9a

Chapter 3

Measurement techniques

In this chapter, the experimental set up that I used for this work will first be described. The second part is about the characteristics of the antenna, with frequency spectral measurements. Then, the global shape of our signals and the information that could be extracted from them we will explained.

3.1 Experimental set up

3.1.1 The sample holder

3.1.1.1 The MBJ system

In order to produce the atomic contact we want to study, we use the mechanical break junction (MBJ) technique [38] as presented in figure 3.1. We use a three points system schematically described in figure 3.2 to bend the substrate and then break mechanically the metal line at its weaker point. The moving part is displaced using a differential screw, which allows us to control the spacing between the two electrodes with a resolution below the atomic scale. The main advantages compared to electro migration or atomic contact in a TEM is the impressive stability of the system as well as the possibility to go back to contact after breaking. At 77 K, the temperature at which our measurements are carried out, the contacts can last for several hours. This is essential for carrying out field sweeps.

3.1.1.2 The rf part

We want to study the rf behaviour up to 40 GHz, so every cable or connector is designed to work at 40 GHz. The rf connector is a mini smp connector from Rosenberger. As shown in figure 3.3, it is pressed on the sample with a launcher in two parts. The one on the top of antenna, around the connector, is in titanium.

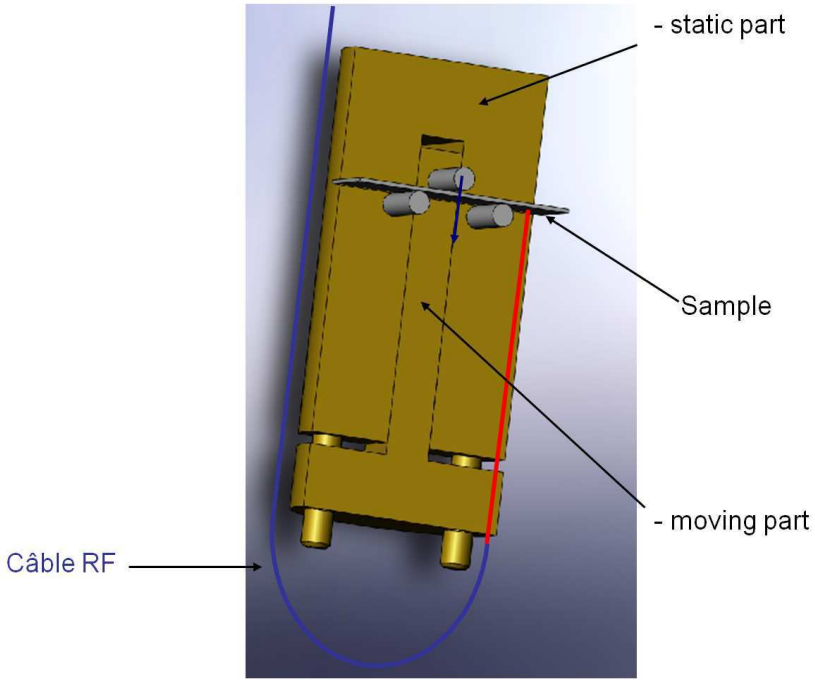

Figure 3.1: Schematics of the sample holder.

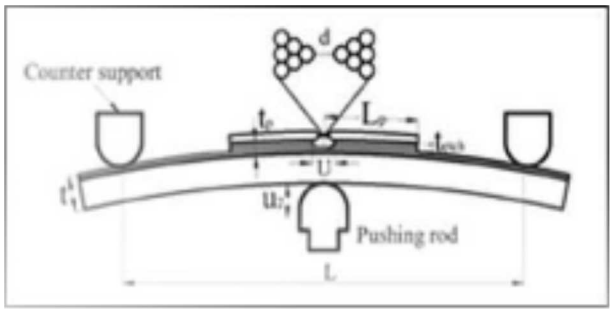

Figure 3.2: Schematics of the three points breaking mechanism.

The other one, on the back of the sample, is in plastic with an ϵ_r near that of kapton to avoid a box effect with the rf. The influence of the choice of kapton instead of titanium is discussed in part 3.2. The two parts are linked by a screw from each side of the kapton.

The last rf cable, shown in figure 3.1, has to be flexible at 77 K and work up to 40 GHz. Indeed mechanical flexibility is essential as the edge of the sample where the rf connector is anchored moves when the substrate is bent. Two rf sources were used. The first one, at the beginning of this work, was an Anritsu rf source from 10 MHz up to 20 GHz. The second source, used for most of the results, is an Agilent

N5183A from 100 kHz up to 40 GHz that was acquired during the course of my PhD. In order to check in real time the state of the antenna, a bias-tee is used just at the source output to allow for a dc measurement of the antena's resistance with a ohmmeter. This bias-tee also protects the rf source from undesirable dc voltages back from the sample space.

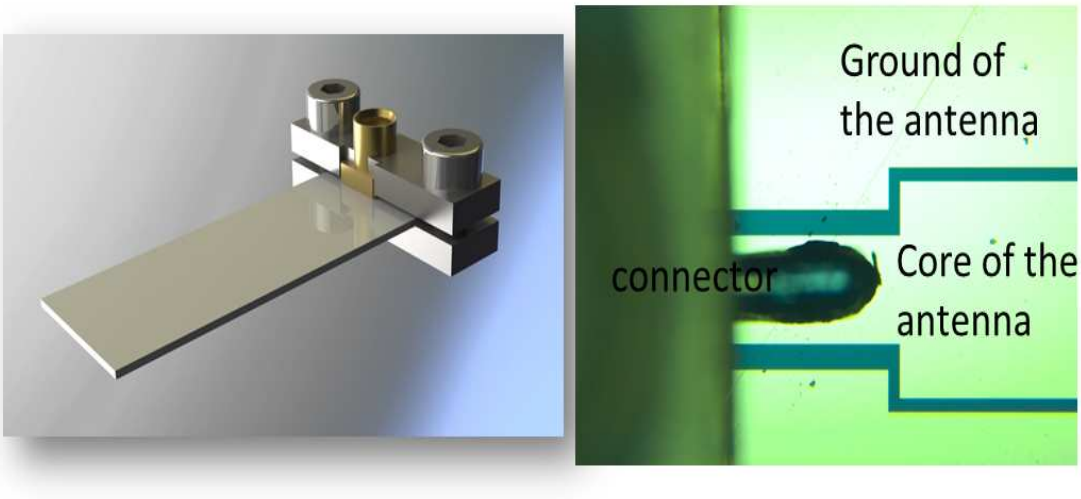

Figure 3.3: Left: schematics of the rf connector on a sample – right: image of the connection between the antenna and the rf connector

3.1.2 Measurement system

To obtain the FMR at different frequencies, a dc magnetic field is required in addition to the rf magnetic field produced by the antenna. In our case dc magnetic fields are applied in the plane of the sample with an electromagnet up to 1.2 T. We measure the FMR electrically, by voltage measurements at the low frequency (below 20 kHz) used to modulate the RF power. For this the FMR is driven by the rf field produced by the antenna. Several kinds of electrical signals are then produced in the sample including rf and dc/ac (below 20 kHz) contributions. The RF one cannot be measured directly with present samples as their contacts are not adapted for the rf propagation. The generated dc/ac voltages are also quite low and they are first amplified by a factor 100 with a LI-75A. A dc/ac contribution due to the rf can occur in case of either a rectified signal [39, 40, 41, 42, 43, 44] or a dc/ac current multiplied by a dc variation of the resistance due to the FMR [39] or else a dc voltage created directly by the rf like the ISHE. These contributions are explained in detail in part 3.4.1, 3.4.2 and 6.2.1 respectively.

We have used a amplitude modulation method of the rf source in order to better isolate signals due to the resonant state, removing the background resistance (without rf excitation) and dc voltage offsets in the amplifier. The amplitude of the rf excitation is modulated by a square wave at the frequency of f_{mod}, the rf power is then on half of the time. The relevant voltage is then measured at this rf modulation frequency f_{mod}, typically near 5 kHz, with a Stanford lock-in amplifier SR830. The sample can be polarized by a dc current using a Yokogawa dc source meter. To follow the resistance of the sample, a superimposed voltage at 17 Hz can be imposed with another lock-in amplifier also used to measure the resulting voltage at the same frequency, i.e. the sample resistance (see figure 3.4). This is essential for the atomic contacts whose stability is only of several hours in the best case. Even in the contact state where the resistance curves are reproducible, this ac polarization gives us information on the macroscopic state of the sample like thermal drift, domain walls and magneto resistance. This superimposed ac polarization is an added voltage sent to the sample, and its 10 $k\Omega$ load resistor in series, by a lock-in amplifier. This added voltage has a gain of 1/10 in the atomic contact state, to reduce the superimposed current To separate voltages at 17 Hz from the one at the frequency of the modulation, we use a Standford560 as selectable bandwidth filter (and selectable amplifier if necessary but noisier than the LI75-A for a gain of 100).

We thus obtain at 17 Hz the full resistance measurement during field sweeps. At the frequency of modulation the effects due to rf are measured. Indeed, the ferromagnetic resonance has been found too small to be measured directly on the resistance see part 3.4.2. We want to underline here that the value of the load resistance does not affect the ferromagnetic measurements, as verified by changing it from 100 Ω to 100 $M\Omega$ (entry impedance of LI75).

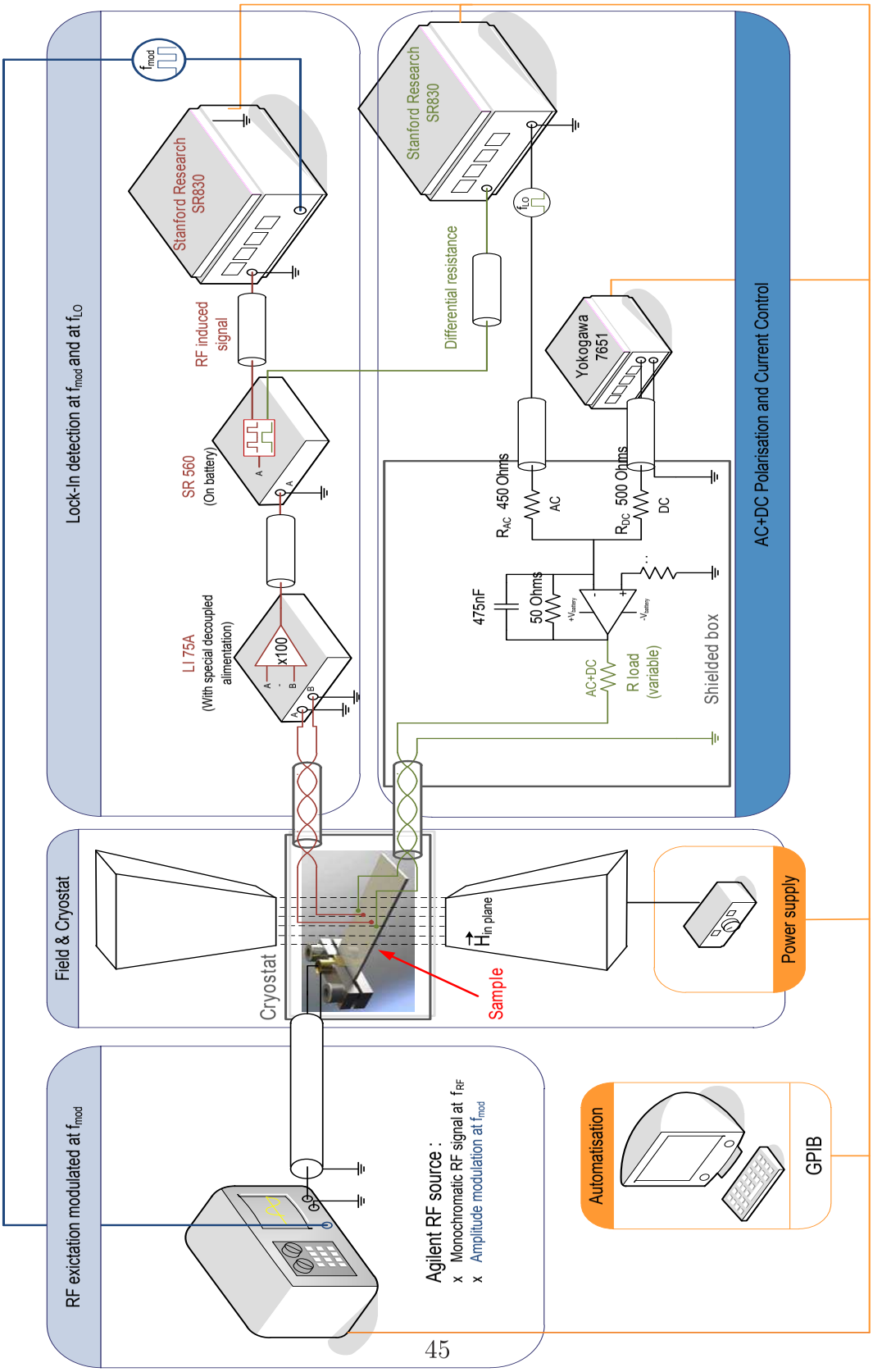

Figure 3.4: Schematics of the measurement system

3.2 Characteristics of the antenna

This section deals with the dependence of our system on the excitation frequency, even in the absence of ferromagnetic resonance. For this the VNA measurements are first addressed and then we will explain what information could be extracted from the measurements at a given static magnetic field when sweeping the rf frequency at a chosen power.

3.2.1 VNA measurements

An important stage to measure the characteristics of our antennas is the use of the vectorial network analyzer (VNA). With the VNA measurements at 300 K, we are interested in the reflection signal from the antenna. As explained in part 2.1.2.2, we first calibrate the VNA with known impedances: short (0 Ω), load 50 Ω and open (infinity). Here we only measure the reflection coefficient S_{11}. (*We will use $S_{11}(dB)$ for power reflexion and* Γ *for voltage reflexion coefficient. We remind here than by definition of dB* $S_{11}(dB) = 20log(|\Gamma)|$ *i.e. 3dB is power divided by 2 and 10 dB by 10*).In the best case our antenna is a short cut to maximize current, and thus the produced rf magnetic field. There are two main possibilities to measure the antenna characteristics. In the first possibility, the antenna and its connector are measured on the VNA. Due to the special mini SMP format of the rf connector, we must add an adapter to pass from SMA to mini SMP. This adapter is not taken into account during the calibration so we measured it alone and then corrected from its reflection coefficient to obtain the one of the antenna and its rf connector. We obtained typically the figure 3.5a.

The second possibility is to measure the antenna, the rf connectors and the rf cables together, which is presented in figure 3.5b. The main difference between these two measurements comes from fast oscillations which make the measurement look noisy with all the rf cables. These oscillations come from the propagation of the signal through the total length of the system (several meters for the return journey of the signal). The low amplitude of these fast oscillations show that cables are well adapted to 50 Ω. The dc resistance of the antenna is typically 13 Ω not 50 Ω and its length is 15 mm from the rf connector, which explains the low and important oscillations. The slight decrease of the average reflection corresponds to a resistance increase with frequency as the impedance Z shown by the VNA at a given frequency is:

$$Z = 50\frac{\Gamma + 1}{1 - \Gamma} \tag{3.1}$$

The other tiny differences are mainly due to the fact that VNA measurements are very sensitive to the quality of the connection between the different parts: the

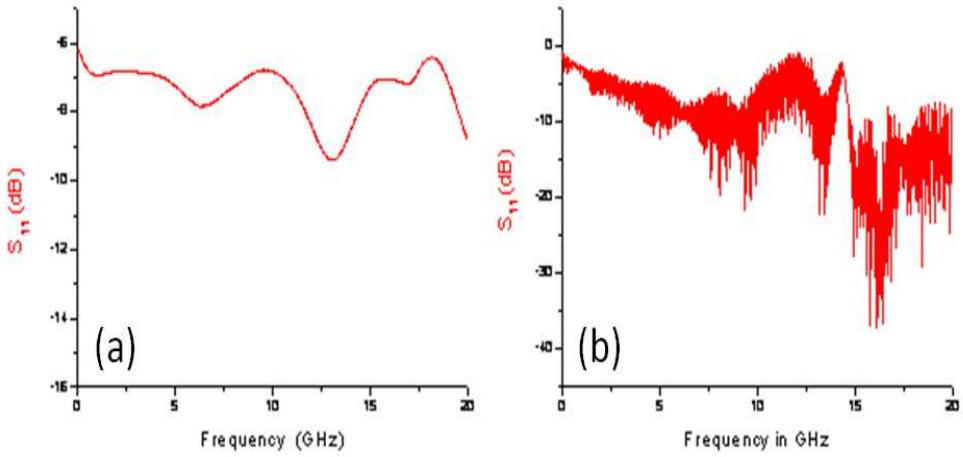

Figure 3.5: (a) Measurement of S_{11} of the antenna and the connnector from 0 to 20 GHz (b) same antenna with all the rf cables.

antenna, the rf connector, the adapter or/and the rf flexible cable.

We can also compare the differences for a same antenna between different launchers in full Ti or mixed Ti/insulator as glass fiber as in figure 3.6. As shown in figure 3.6b the full Ti launcher add a peak at about 5 GHz on the Γ curves. This peak is due to a change in boundary conditions due to the Ti in both sides of the antenna acting like a secondary waveguide. The amplitude 0.6 of Γ at low frequency corresponds to an impedance of 12.5 Ω which is the dc resistance of the antenna. The period of oscillations always corresponds to the length of 15 mm of the antenna and the connector.

This is why we finally used a launcher in *KLF* with the ϵ_r nearest from that of the kapton substrate for the part below the antenna. Indeed above the antenna and around the connector, Ti works well as the connector is already above the antenna. Typically we obtain then the data shown figure 3.7.

So to estimate the power that reaches the end of the antenna, we must remember that we lose 3 dB because it is a CPW with two parts in the extremity (in fact 3 dB when the short end is symmetric and a few more when it is asymmetric see figure 2.7). For the loss due to the antenna characteristics measured with the VNA, we have to use power loss, $|\Gamma|^2$ but without losses after reflection so 3 dB. We obtain in total an average rf power on our short ended decreased by 6dB from the one output by the rf source. Anyway, in the following, we will always mention the power delivered by the source for a load impedance of 50 Ω.

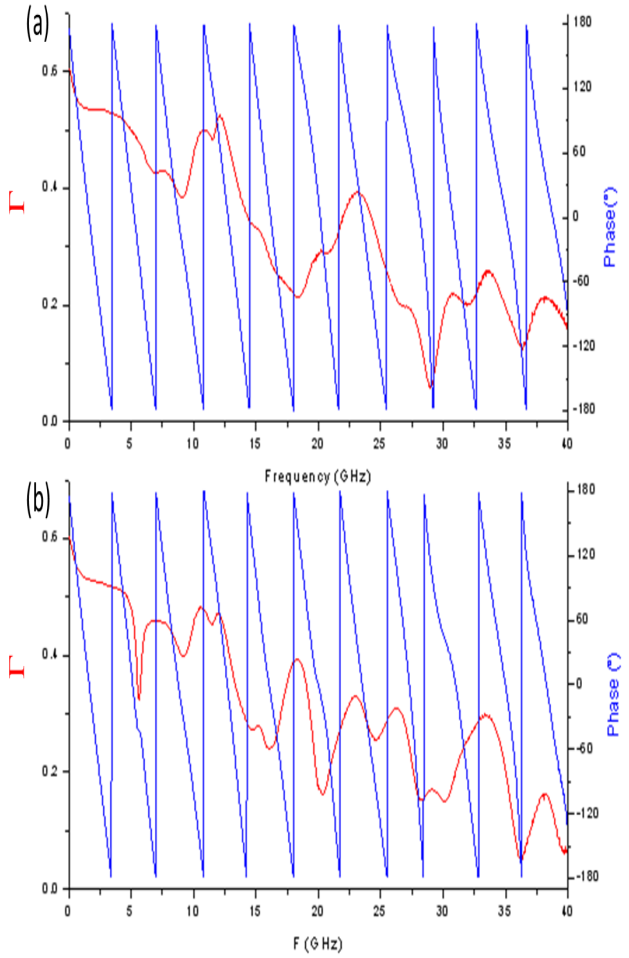

Figure 3.6: (a) VNA measurement with a mixed Ti/fiberglass launcher (b) with a full Ti launcher.

3.2.2 Measurements with a frequency scan

Now we will be interested in the frequency scan measurements, where the frequency is swept under constant static magnetic field and constant power delivered by the rf source. The measurement itself can be the resistance of the sample or the different voltages reporting the effect of the rf irradiation. First results on a non magnetic gold sample will be discussed and then on a magnetic permalloy sample which is not under resonant conditions.

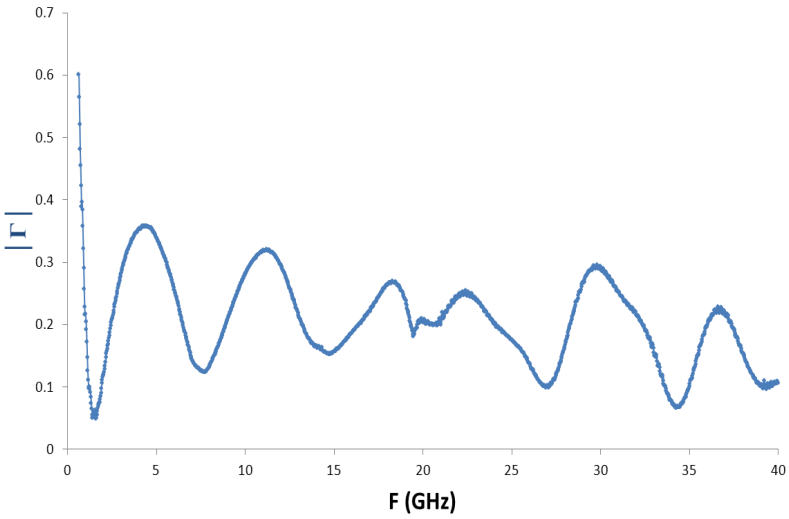

Figure 3.7: VNA measurements with the best adapted launcher: mixed Ti/*Klf*.

3.2.2.1 Metal contribution

What is measured with the resistance is essentially heating due to the power that reaches the end of the antenna. For this we realized a sample fully in gold, without any magnetic part. The image of this gold sample is shown in figure 3.8. We have checked that there is no dc contact between the stripe and the antenna.

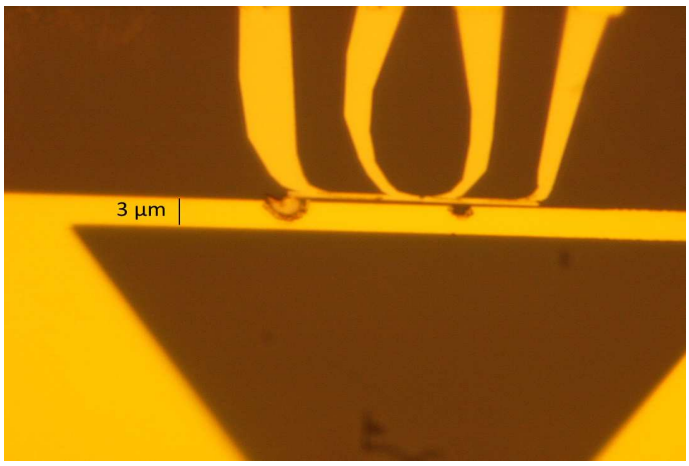

Figure 3.8: Image of a pure gold sample.

When measuring the resistance, we only see a dc change of temperature in the graph, shown in figure 3.9, representing the voltage measured on the load resistance of 10 kΩ. There is a small peak near 3 GHz which is due to a defect of the antenna.

We can also see that the power oscillations measured with the VNA in section 3.2.1 are not really present. However we can still see the reduction of power heating with frequency increase. This decrease is higher than in VNA measurement as the transmission of the bias tee (mentioned at the end of part 3.1.1.2 to measure the resistance of the antenna) is decreasing with the frequency. The different changes with power shown in figure 3.9 is understandable. Indeed when the applied power is decreased by two, the resistance heating is divided by two and when the source square modulation is turned on, the average rf power in time is divided by a factor two and so is the heating.

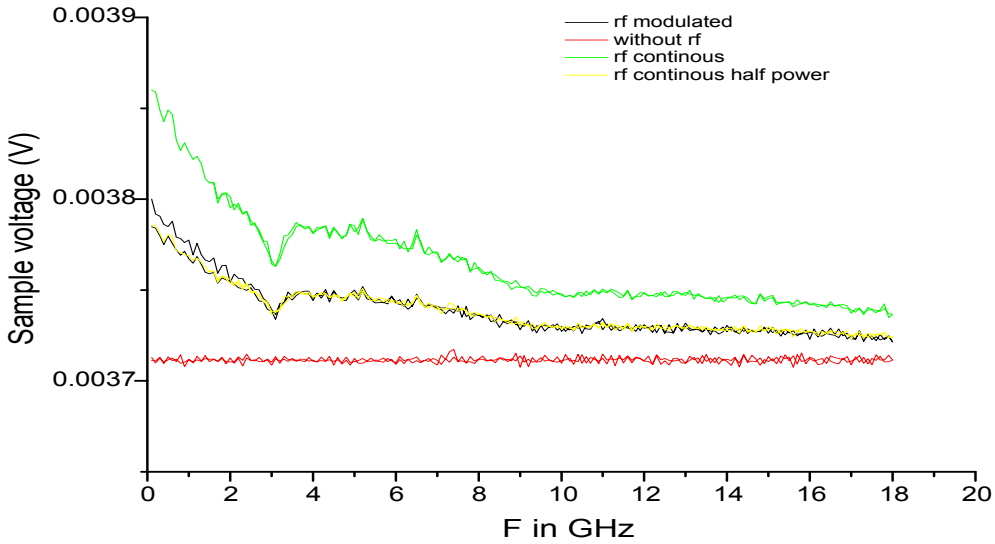

Figure 3.9: Frequency dependence of resistance voltage; each curve corresponds to a different power supplied.

We can also measure a voltage, baseline at the rf modulation frequency f_{mod} that does not depend on the applied static magnetic field as the sample is not magnetic. The level of this base line depends on the rf power. As shown in figure 3.10 the dependence in frequency of this voltage is similar to the one due to the resistance. However there are some differences as some peaks are present in the baseline voltage and not in the resistance curve. So the base line of this voltage, is not the exact image of the rf power seen by the sample with the frequency.

3.2.2.2 Magnetic contribution

Let us see here what changes in the presence of a ferromagnetic sample. Measurements are performed on magnetic stripes as shown in figure 2.9. We avoided the presence of FMR peaks on the measurements by carrying them out in zero applied magnetic field and after saturation in the parallel geometry to avoid the presence of

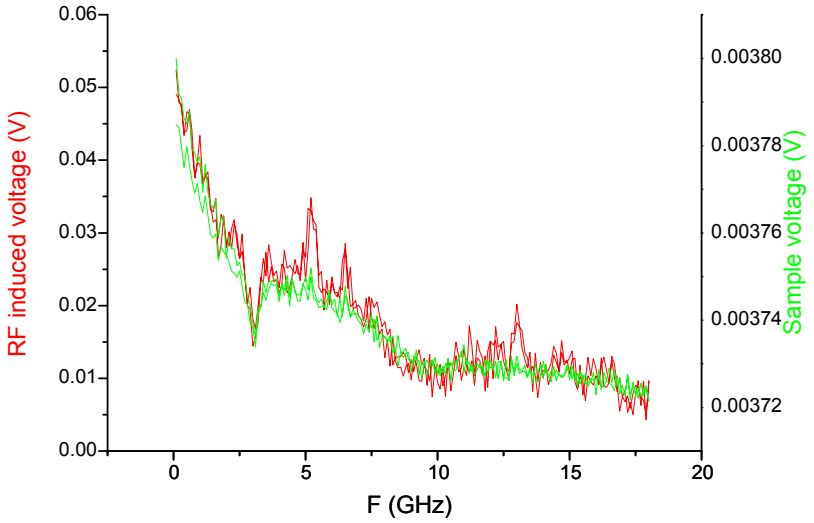

Figure 3.10: Comparison between the resistance spectrum and the rf induced rectified voltage spectrum.

domain walls. We are not able to detect the resonant frequency as we obtained the same curve in a 1 T magnetic field parallel to the stripe.

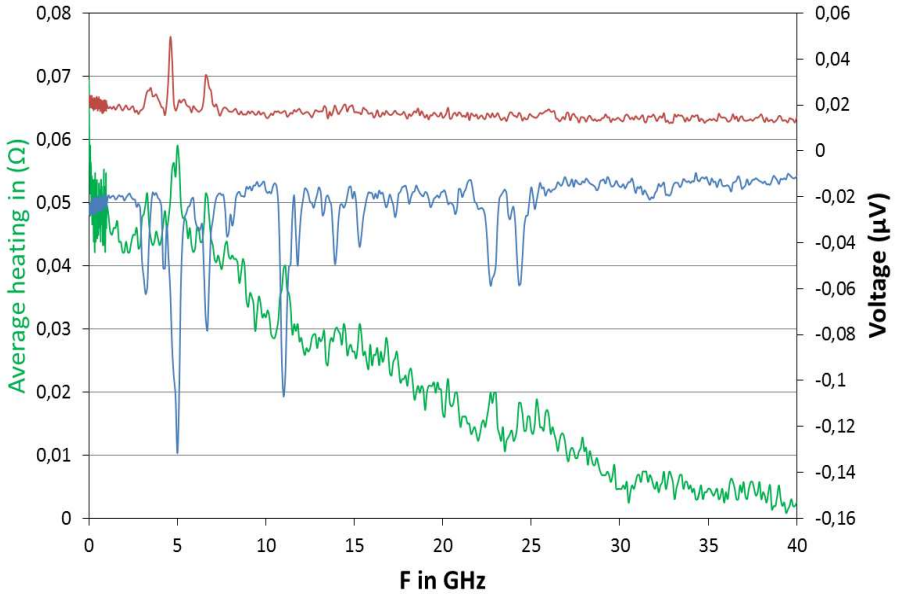

Figure 3.11: Resistance variation due to heating in green and rf induced voltage versus frequency at 77K and zero applied static magnetic field on the sample of figure 2.9 with a power of 0dBm.

In figure 3.11, we have a higher number of sharp peaks than on the non magnetic sample, both on the measured voltage at f_{mod} and the resistance heating. This numerous sharp peaks are a signature of magnetic samples. The red curve corresponds to the voltage at f_{mod} on the 'twin stripe' without constriction (see figure 2.9a). Peaks on the blue curve are due to resistive heating from the stripe with a constriction. And so the rf power seen by the single stripe is not exactly the same as the one with the constriction. This is understandable as the dc contacts are different so they do not lead to the same induced currents. The constriction can also influence the induced currents as evidence by the high number of peaks on the stripe with constriction. An other way to measure the heating, hence the power, is to pass a dc current through the sample. Then the voltage measured at f_{mod} is proportional (after subtraction of the voltage without dc current) to this dc current and the average change of resistance induced by the rf. The background of the resistance value is then eliminated. This time, as shown in figure 3.12, the differences with the resistance measurement are tiny. It should be noted that here at 1T, the uniform resonance frequency is above 40 GHz so there is no peak due to FMR in the curve.

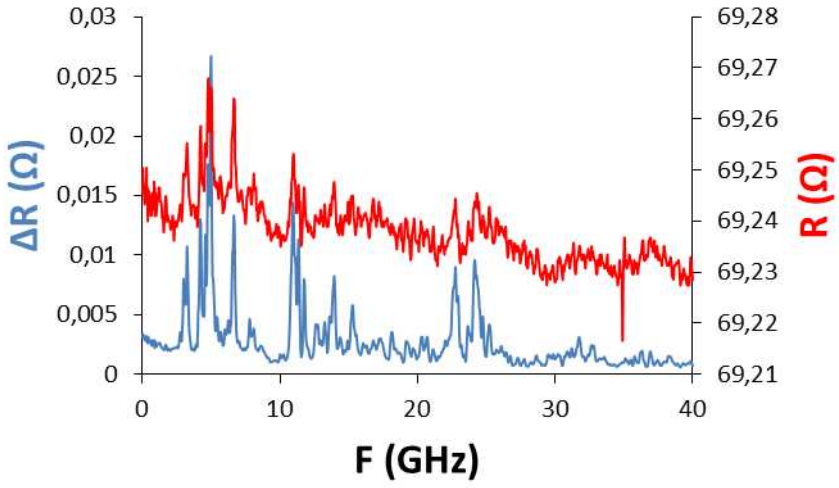

Figure 3.12: Comparison of two different ways to measure the rf induces heating at 1T versus frequency. The red curve is a direct resistance measurement and the blue one is that obtained passing a dc current (see part 3.4.2).

It is interesting to note that the heating of the antenna itself is lower than the one on the sample i.e. below 0.7% compared to 5% on the sample. That is why we used heating measurements carried out on the sample to determine the relative rf power of the antenna at different frequency.

3.3 Dynamics of anisotropic magnetoresistance

In this thesis work, we aim to study the FMR using electrical effects linked to spin dependent transport. Our goal is also to study it in nanostructures and even down to atomic scale where electronic transport properties can be enhanced by atomic configurations. In our devices, the magnetoresistance is generally dominated by AMR effects. Let us calculate here the variations of resistance due to AMR when the magnetization is slightly moved from its equilibrium position [6].

By definition the AMR is proportional to the square of the magnetization projection along the local current lines $\vec{j} = j\vec{x}$. For the notation x is the direction of the current x' that of the magnetization (in the xy plane)at equilibrium and z is perpendicular to the plane defined by xy. The xyz and x'y'z referentials are orthonormal.

$$AMR \propto \frac{(\vec{M}.\vec{j})^2}{(jM_s)^2} \tag{3.2}$$

$$AMR \propto ((\frac{M_{x'}}{M_s}\vec{x'} + \frac{M_{y'}}{M_s}\vec{y'} + \frac{M_z}{M_s}\vec{z}).\vec{x})^2$$

where $M_{x'}$ is the magnetization along x', $M_{y'}$ along y' and M_z along z.

$$AMR \propto (\frac{M_{x'}}{M_s}\vec{x'}.\vec{x} + \theta_{y'}\vec{y'}.\vec{x})^2$$

where $\theta_{y'} = \frac{M_{y'}}{M_s}$ and $\theta_z = \frac{M_z}{M_s}$ The conservation of the magnetization norm allows us to express $\frac{M_{x'}}{M_s}$ as a function of $\theta_{y'}$ and θ_z. At equilibrium, the magnetization is along $\vec{x'}$ and we are in the limit of small deviations i.e. $\theta_{y'}$ and $\theta_z << 1$:

$$\theta_{x'} = \frac{M_{x'}}{M_s} \approx 1 - \frac{1}{2}(\theta_{y'}^2 + \theta_z^2)$$

Which gives for the AMR

$$AMR \propto (\vec{x'}.\vec{x} - \frac{1}{2}(\theta_{y'}^2 + \theta_z^2)\vec{x'}.\vec{x} + \theta_{y'}\vec{y'}.\vec{x})^2$$

Developing to second order

$$AMR \propto ((\underbrace{\vec{x'}.\vec{x}}_{\cos\beta})^2 + 2\theta_{y'}\underbrace{(\vec{y'}.\vec{x})}_{-\sin\beta}(\vec{x'}.\vec{x}) - (\theta_{y'}^2 + \theta_z^2)(\vec{x'}.\vec{x})^2 + \theta_{y'}^2(\vec{y'}.\vec{x})^2)$$

At equilibrium and zero rf field, the magnetization makes an angle β with the current lines. Now we can express the variation of resistivity due to the AMR effect with the small motion of magnetization around its equilibrium position:

$$\delta\rho_{AMR(t)} = \Delta\rho_{AMR}\left[-\sin(2\beta)\underbrace{\theta_{y'}(t)}_{at\omega} - \underbrace{(\theta_{y'}^2(t)+\theta_z^2(t))}_{\text{at dc and } 2\omega}\cos^2\beta + \underbrace{\theta_{y'}^2(t)}_{\text{at dc and } 2\omega}\sin^2\beta\right] \tag{3.3}$$

where $\Delta\rho_{AMR}$ is the difference of resistivity between $\vec{M}$ parallel and perpendicular to $\vec{j}$. In equation 3.3, the frequency of each term is indicated in the case when the motion of magnetization is harmonic, i.e. for the experiments of this thesis work.

It is worth noting that this represents a local variation of resistance as current lines are only defined locally. To estimate the full variation, one should integrate on the current lines. This formula can be used without any particular hypothesis about a resonant excitation or about the direction of the rf magnetic field. It is however true that these effects are enhanced when the FMR conditions are fulfilled. We can notice that the resistance variation is of first order in θ with the ω component whereas dc and 2ω components are of second order in θ. It is important to note here that the ω component can be measured as a dc voltage using a rectifying technique (part 3.4.1), which is the basis of the work presented in this thesis. On the other hand, the dc component of the resistance can be measured directly using a dc current (part 3.4.2).

3.4 Measured signal

In this part we will describe the signal measured, explain what we could extract as characteristic of magnetization and its dynamics. The exploitation of the measurements will be presented in the next three chapters of this thesis. We will consider here a thin magnetic stripe along $\vec{x}$ and parallel to the shorted end of our antenna (and its current lines). The static magnetic field is applied with an angle ψ from the $\vec{x}$ direction. The rf source is modulated at f_{mod} by a square signal, meaning that the rf source is alternatively turned on and off. The measurements are performed with lock-in amplifiers (which give voltages in RMS value and not the peak voltage). We will always plot the lock-in voltage as the measured voltage however in the calculus, there will be a factor $\sqrt{2}$ to convert it into peak values. An other factor comes from the rf amplitude modulation.

Basically there are two possible measurements. The first measurement (part 3.4.1) is the rectified signal which gives us information on resistive magnetization dynamics at the rf frequency. The second measurement (part 3.4.2) requires a dc current in the sample to extract the average change of resistance induced by the magnetization dynamics.

3.4.1 Signal at zero dc current

In this part it is discussed how to exploit the term in ω of equation 3.3. For this we only need the rf irradiation and no biased voltage on the sample is required. To be measurable at as a dc signal, the resistive AMR contribution at ω should be multiplied by a current at the same frequency, this is the rectification technique[41, 45, 42, 43, 44]. Such a current I_0 already exists in our samples due to capacitive and mainly inductive coupling [46] to the CPW. With the software Sonnet we calculated the capacitive part and found that it was negligible compared to the current generated by inductive coupling. We can then measure the resulting voltage versus the applied field at a given angle ψ. Figure 3.13 presents an example of such a measurement.

Using equation 3.3, the rectified measured voltage is defined by :

$$V_{rectified} = \frac{1}{\sqrt{2}} * square(t) * -\Delta R_{AMR} \sin(2\beta)\theta_{y'}(t) * I_0 \cos(\omega t + \Phi) \tag{3.4}$$

with Φ the angular phase between the induced current and the rf magnetic field. The term square(t) represents the square amplitude of modulation whose fundamental component has a value of $2/\pi$. ΔR_{AMR} is the difference of sample resistance between magnetization parallel and perpendicular to the current lines.

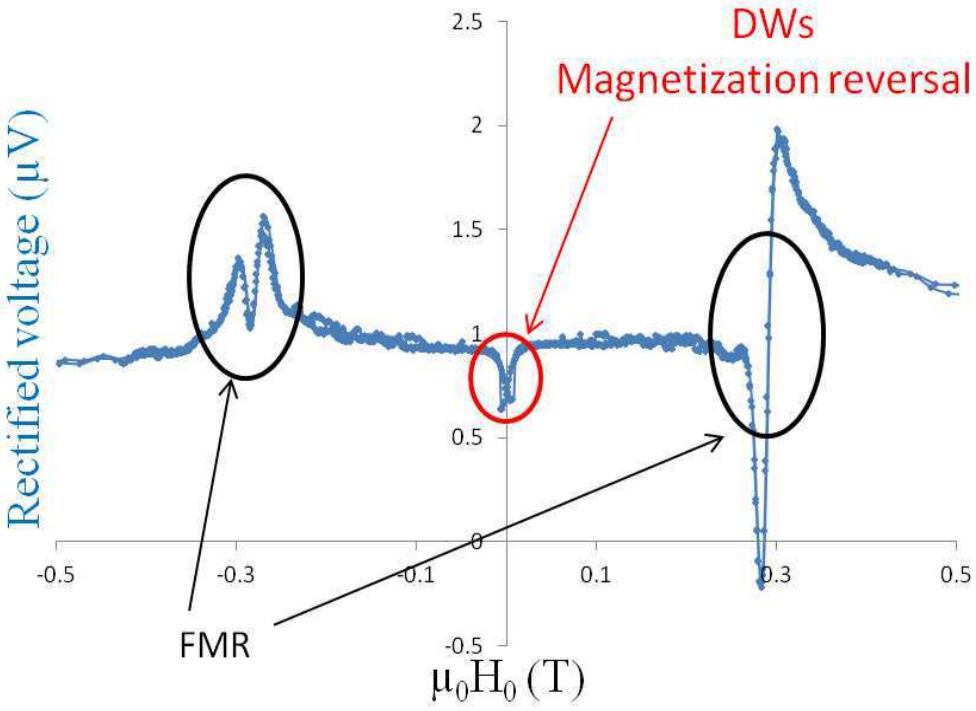

Figure 3.13: Evolution of the rectified voltage versus external magnetic field swept from -1T to 1T and back to -1T.

$M_{y'}(t)$ can be expressed for a rf magnetic field h_z perpendicular to the device along $\vec{z}$

$$M_{y'}(t) = \theta_{y'}(t) * M_s = \chi'_{y'z} h_z \cos(\omega t) + \chi''_{y'z} h_z \sin(\omega t) \tag{3.5}$$

and for a transverse rf magnetic field h_y

$$M_{y'}(t) = \chi'_{y'y} h_y \cos(\beta) \cos(\omega t) + \chi''_{y'y} h_y \cos(\beta) \sin(\omega t) \tag{3.6}$$

The term in $\cos(\beta)$ is due to the projection of h_y along y'. Experimentally if we take account of the antenna thickness the applied rf field makes an angle of 3° with the perpendicular of the sample plane. So there is both planar and perpendicular rf fields. Finally we obtain two terms for the measured rectified voltage. The first one is due to a perpendicular rf magnetic field:

$$V_{rectified} = \underbrace{\frac{1}{\sqrt{2}}}_{Lock-in} * \underbrace{2/\pi}_{modulation} * -\frac{1}{2}\frac{I_0 \Delta R_{AMR}}{M_s}\sin(2\beta)(\chi'_{y'z} h_z \cos(\Phi) + \chi''_{y'z} h_z \sin(\Phi)) \tag{3.7}$$

and the second one is for transverse planar rf magnetic fields:

$$V_{rectified} = \underbrace{\frac{1}{\sqrt{2}}}_{Lock-in} * \underbrace{2/\pi}_{modulation} * -\frac{1}{2}\frac{I_0 \Delta R_{AMR}}{M_s}\sin(2\beta)\cos(\beta)(\chi'_{y'y} h_y \cos(\Phi) + \chi''_{y'y} h_y \sin(\Phi)) \tag{3.8}$$

Using this equation let us study which information could be extracted from the FMR peaks of figure 3.13.

A very interesting observation is that equation 3.8 is odd (maximal for $\beta = 35^o$) with the applied static magnetic field ($\beta \Rightarrow \beta + \pi$) whereas equation 3.7 is even (maximal for $\beta = 45^o$). Thus, as shown in figure 3.13, the FMR of saturated domains is not symmetrical with the applied field. Due to the dephasing between induced currents and AMR variations (the angle Φ), the FMR peaks obtained with the rectified technique do not have simple shapes like Lorentzian or its derivative, but contain all their *linear* combinations. The dephasing Φ depends a lot on the frequency and can be fitted using results of simulations of the susceptibility, to lead reasonable shapes for the signals. We want to emphasize that the FMR peaks, using the rectified technique, are well defined and perfectly reproducible. Hence they are very useful to determine the dispersion law (M_s, γ, demagnetization factor) and the factor $I_0 h_{rf}$, although without the possibility to differentiate the two terms of the mixing by a simple measurement. The good signal quality allows us to study the dependence of the FMR on the angular variation of the static magnetic field. The sensitive dependence of Φ with the frequency makes measurements of the FMR peak in frequency scans very difficult to interpret correctly. This is why nearly all studies presented in the following chapters use measurements of rectified voltages in field scans.

The second feature of this type of measurement concerns the shape of the hysteresis at low field. It can be understood considering how the magnetization relaxes from saturation to zero field or reverses from an opposite direction. In these two cases, the β angles are initially opposite. Hence, as the susceptibility is not equal to 0, we can observe a hysteresis of an amplitude and sign depending on Φ values. Interestingly, the reversal can be achieved with or without the presence of domain walls (see reference [47]), but features associated to this presence must be observed in this region. Indeed DWs can induce a signature on the rectified signal if their

dynamical properties modify the ω component of resistance.

The third characteristic of figure 3.13 is the position of its base line. One contribution to the base line could be the evolution of the susceptibility out of resonance. The other part is likely to be due to thermal effects in the contacts. A rough calculation actually gives the right order of magnitude from thermoelectric effects. It should be noted that the base line is the only part of the signal affected by the value of f_{mod} with a small decrease when f_{mod} increase. However this is not the object of this thesis work and we did not study it in detail.

There is a last signal which can appear in this kind of measurement. Indeed if a magnetic effect generates a dc voltage while the sample is under rf irradiation, this adds a contribution to the measured rectified signal. This is the case with the inverse spin hall effect(ISHE), which is the object of chapter 6 where we will see how the two contributions can be separated.

This zero current signal is called the *rectified signal* in this manuscript, except in the ISHE section where it is called the AMR contribution in order to differentiate it from the ISHE contribution which is also measured without running a current through the sample.

3.4.2 Signal in presence of a dc current

In this part we are interested in the signal measured at f_{mod} when a dc current is passed through the magnetic sample, similarly to the work of ref [39]. This dc current can interact with dc variations of resistance, induced by the rf field, and thus be measured at f_{mod}. This, of course, adds up to the rectified signal without dc current presented in part 3.4.1. The contribution due to the dc current is extracted by subtraction with the voltage without dc current (in that case we suppose that the dc current is not large enough to affect the magnetization and its dynamics). Then we divide the voltage by the dc current value and obtain the average resistance change measured. Figure 3.14 shows an example of such a measurement. The signal is proportional to the power, as it is in second order to magnetization dynamics and so first order in power.

Using equation 3.3, we can express the resistance measured as follows:

$$\delta R_{measured} = \underbrace{\frac{1}{\sqrt{2}}}_{lock-in} * \underbrace{2/\pi}_{modulation} * \frac{1}{2}\Delta R_{AMR}\left[-(|\theta_{y'}|^2 + |\theta_z|^2)\cos^2\beta + |\theta_{y'}|^2\sin^2\beta\right] \tag{3.9}$$

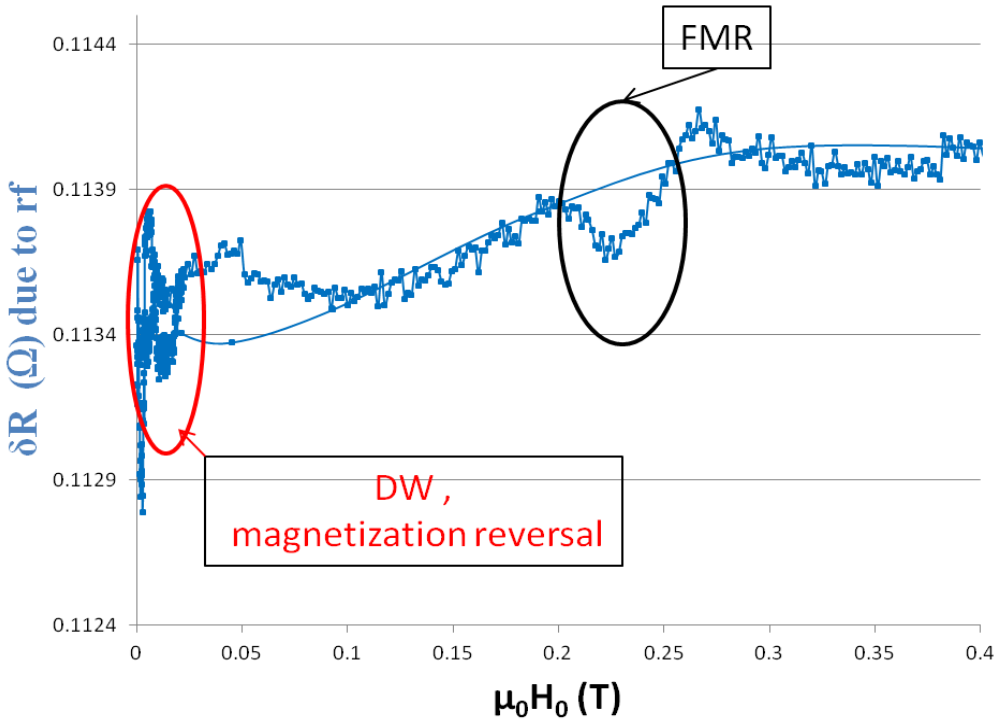

Figure 3.14: Example of the resistance change due to rf irradiation (measured using a dc current), versus the applied static magnetic field. The global resistance is 400 Ω and $\psi = 0$.

In this measurement, the FMR peaks are really smaller. Indeed in figure 3.14 the angle β was set to zero in order to optimize the measurement sensitivity and the current density was also high, an essential requirement to extract the peaks from noise. Also, this measurement does not work at all frequencies so the dc variation of resistance is less useful to establish a dispersion law. Moreover, as θ_z^2 is negligible due to aspect ratio of the stripe, equation 3.9 can be rewritten:

$$\delta R_{measured} = -\frac{1}{\sqrt{2}} * \frac{\Delta R_{AMR}}{\pi}(|\theta_{y'}|^2 \cos(2\beta)) \tag{3.10}$$

Fortunately we can determine $\theta_{y'}$ and so using a simulation we have access to the rf magnetic field h. We can note that the amplitude of FMR peaks is so low that it can not be measured directly on the resistance. Indeed the base value of the sample measured in figure 3.14 was ~ 430 Ω.

The low field region where magnetization reverses shows higher rf induced resistance variations than the FMR signal at higher field. So using a dc current to probe the resistance variations can unveil some information on reversal or domain

wall dynamics.

The base line is again mainly due to heating. Indeed when the rf is turned on the sample gets heated by this power. Therefore as said in part 3.2.2.2 this heating is an image of the rf power delivered by the antenna at a given frequency.

The major problem with this kind of measurement is that it can not be used in an atomic contact regime. Indeed in atomic contacts, a high current density induces electro migration and often results in breaking the contact. So we avoid it. For the atomic contact we only use the rectified effect, probing the dynamics at ω_{rf}. The effect of dynamic on the dc resistance (measured with the superimposed current of $\sim 20\ nA$ at 17 Hz and so without $\sqrt{2}$, π term) can only be seen if it is large enough compared to the ballistic resistance.

Chapter 4

Ferromagnetic nanostructures

Before studying the FMR in the atomic contact regime, we must first try to understand the behavior of FMR in the as produced samples, before bending our device to produce atomic contacts. This chapter is thus devoted to a study of the magnetic excitations in the unbroken nanostructures. We will first see that the behavior of thin nanostructures is well understood. In a second step, measurements in thicker nanostructures are presented, and we will se that these are more difficult to understand. Interestingly, we will point out that magnetic excitations can occur in saturated domains but also during magnetization reversal, i.e. it is influenced by the presence of domain walls. Both signatures (from equation 3.3) in voltage at ω_{rf} and dc variations of resistance will be studied.

4.1 A thin sample

The sample is constituted of two stripes, one with a constriction and one without constriction. The stripes are 5 nm thick 620 nm wide permalloy with a 300 nm wide notch for the stripe with a constriction. The distance to the antenna is 700 nm see figure 4.2. Measurement are carried out at 77 K with a rf delivered power of 0 dBm.

The AMR was measured in the first place with a magnetic field of 1 T while changing the applied angle ϕ. We obtained 0.75 % of AMR, which corresponds to 3.4 Ω for the resistance value. First the uniform FMR modes of saturated domains will be explored. Then, the dynamical behaviour of domain walls under rf irradiation will be discussed but without rf induced propagation.

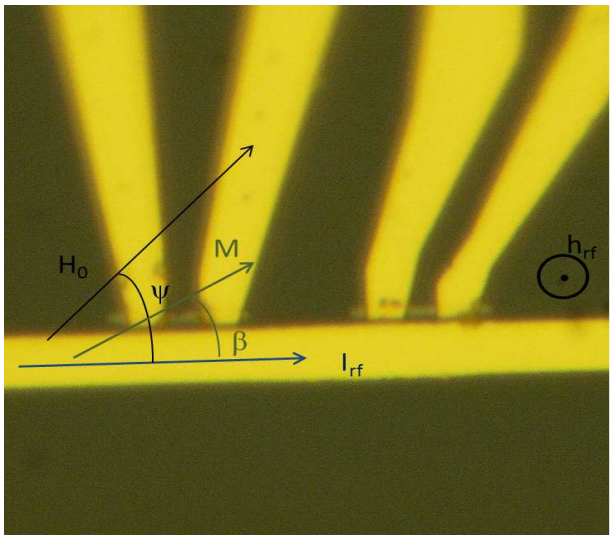

Figure 4.1: Optical image of a typical sample with the main notations. The bottom gold stripe is the antenna and two 'twin' Py samples are electrically connected. The left one has a constriction and the right one is the reference sample composed of a simple stripe.

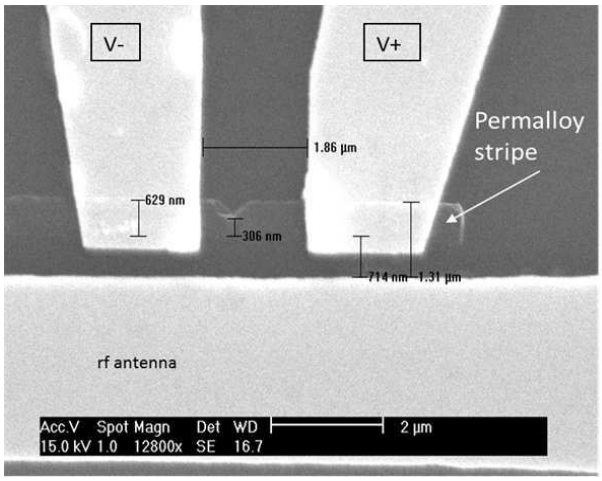

Figure 4.2: SEM image of the subsample with a constriction.

4.1.1 FMR of saturated magnetic domains

4.1.1.1 Characterization of the excitation with a dc current

As explained in part 3.4.2, when a dc current is passed through the magnetic sample, we can measure the change in resistance due to the rf field. This allows us to quantify the average in plane angle of precession and in turn, to estimate the

amplitude of the rf magnetic field. A typical measurement is shown in figure 4.3.

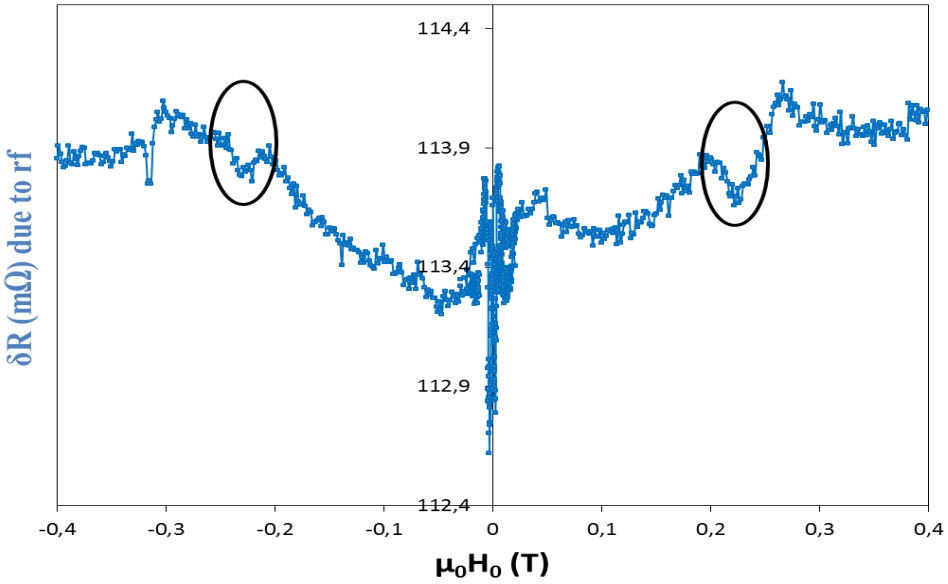

Figure 4.3: Measurements of the average resistance variation for a frequency of 15 GHz with the static magnetic field parallel to the main direction of the stripe. The peaks due to the FMR of the saturated sample are shown by the black circles. The measurements were carried out on the stripe with a constriction.

We can see that FMR peaks are not completely symmetric in amplitude, probably due to the importance of the noise, so we measured an average value of 120 $\mu\Omega$ induced by the rf irradiation for the amplitude of the FMR peak at 0.23 T. The base value of the resistance is 430 Ω for this sample. The change in resistance corresponds to 2.8 10^{-7} of the base value. The current through the sample is 60 μA, corresponding to an average current density in the constriction of 5 $10^6 A/cm^2$. Assuming that AMR is responsible for the signal and using equation 3.10, the in plane angle of precession is determined by equation 4.1:

$$\theta_y = \sqrt{\sqrt{2} * \pi * \frac{|\delta R_{\mathrm{FMR}}|}{\Delta R_{AMR}}} \tag{4.1}$$

with δR_{FMR} the measured resistance variation. For this sample at 15 GHz of rf frequency excitation, we obtain 0.73°, which corresponds to a rf magnetic field $\mu_0 h_{rf}$ of about 0.2 mT. The small values for the angle and the rf field indicate that we are in the linear regime of ferromagnetic resonance. Indeed when the precession angle is too large, the changes of the peak shape are no more proportional to the rf power.

4.1.1.2 Magnetic properties with the rectified signal

Let us now investigate the rectified signal. We have demonstrated in part 3.4.1 that it measures the voltage at the rf frequency but it depends on an angular phase Φ between the induced current and the rf magnetic field. Assuming that the fundamental resonant mode is the uniform one, we aim to simulate the resonance of the simple stripe for different angles ψ of the applied static field and different frequency.

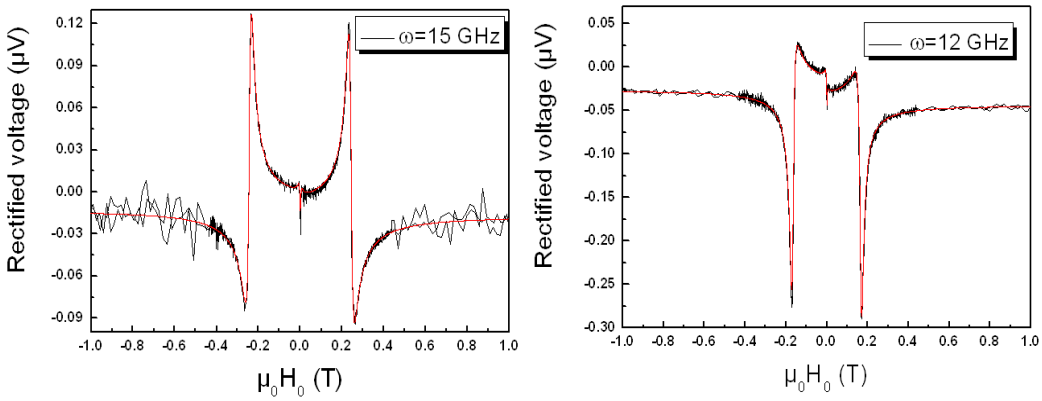

Figure 4.4: Experimental data and simulation for two frequencies 15 GHz and 12 GHz. The measurements have been carried out on the stripe without constriction for an angle ψ of 68°.

The phase Φ and the level of the base line are taken as as free parameter in our simulations, but these only depend on the frequency and not on ψ. To increase the efficiency of the model we simulate the behavior of a simple stripe without constriction, in which the demagnetization factor is likely to vary only very little. In figure 4.4 we show the results of both measurements and simulations with two frequencies 12 GHz and 15 GHz for an angle ψ of 68°. The fitting parameters characterizing the material were the followings for all the frequencies (not only 12 and 15 GHz):

-For the saturating magnetization $\mu_0 M_s = 0.9950$ T
-The damping parameter $\alpha = 0.024$
-The demagnetization factor $N_y = 0.008$ $N_x = 0.001$

These parameters are usual parameters of our permalloy stripes, and one will notice that the damping is quite high. The demagnetization factors are in good agreement with the stripe dimensions. Thus we obtain an excellent agreement between simulation and experiments for the dispersion relation as represented in figure

4.5. The difference with a pure Kittel's law is that in our case β, the magnetization angle, depends on the applied field. Hence, the demagnetization field varies when the resonant frequency changes. From the ratio between odd and even parts of the signal, we infer a small angle of 3° to a full perpendicular rf magnetic field, which is consistent with our geometry. For 12 GHz, we obtain a rf current of 277 μA with a phase of 136° versus 222 μA and 75° respectively for 15 GHz at the resonance. These currents and phases are the same for all the angles ψ. Surprisingly, these rf currents are far too high for a simple induction due to the flux of an excitation field of 0.2 mT inside our device which would give us a current of about 2 μA. This is understandable as at the resonance more rf power is absorbed by the magnetic device, thus dramatically increasing the rf current in the magnetic device at resonance. These current and phase depend highly on the frequency but not on the angle of the applied magnetic field.

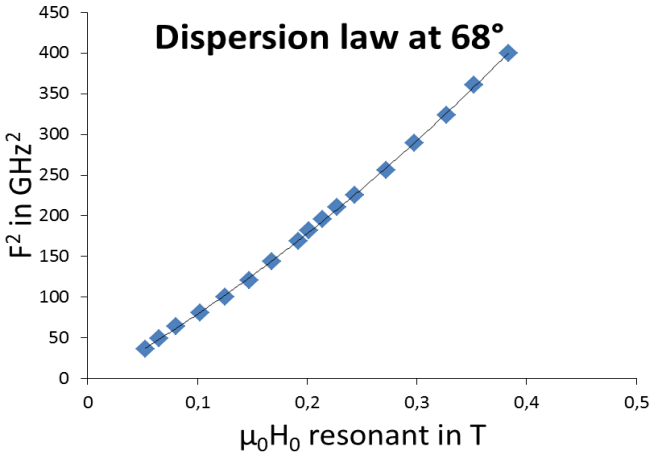

Figure 4.5: Dispersion law of the fundamental ferromagnetic resonance with Ψ=68°. The experimental points are the blue squares and the fit is the thin dark line.

The model used for the simulation is a macro spin model. It is working very well in thin samples as the approximation of thin layer is justified. In the stripe with a constriction, one can expect the constriction to slightly change locally the value of the demagnetization field. However this change seems very low with the present dimensions, as the measured resonant fields are the same for the two subsamples as shown in figure 4.6 for two frequencies 15 GHz and 7 GHz (this is true for all frequencies). It has to be noted that there is a difference of shape between the two subsamples. This is due to a phase difference between the rf currents of the two samples and it is expected as their dc contacts are not at all symmetric.

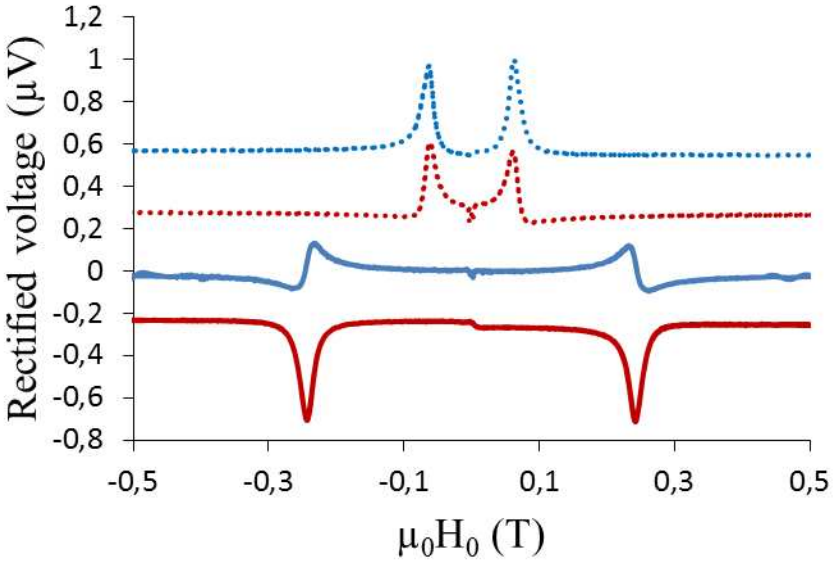

Figure 4.6: Rectified signals for two frequencies, 15 and 7 GHz, in solid and dotted lines respectively. Blue curves are for the stripe without constriction and the red ones for the stripe with a constriction. The static magnetic field is applied at an angle of 68° with the parallel state.

4.1.1.3 Conclusion on uniformly magnetized domains

These results, on a uniformly magnetized thin sample, demonstrate that our set up is able to measure correctly the fundamental uniform mode of ferromagnetic resonance of very thin layers. The magnetic properties determined with the measurements are in good agreement with the known properties of our Py. The dc variation of resistance measured can be as small as 3 10^{-7} of the base value i.e 0.7° of precession angle. The corresponding rf magnetic field is about 0.2 mT. With a high sensitive but not qualitattive measurement, the rectified signal, we can detect resonance with a precession angle even 30 times lower in the best conditions when the angle between current and magnetization is near 45° using the rectified technique.

4.1.2 Dynamics in domain walls

We are know interested in the susceptibility of the system when magnetization reverses, especially in the presence of domain walls (DW). We have seen in figure 4.3 that the resistive response of the system during the reversal gives a signal significantly higher in amplitude than the FMR peaks. After a description of what has

already been done in the literature on the interaction of rf fields and currents with domain walls, we will present our measurements on the response of a domain wall to rf excitation at high frequency. Indeed, most published works deal with frequencies around the GHz that help to depin the DWs whereas the present study addresses the interaction with higher frequencies. The dc current used to measure the resistive signal was kept below the depinning one. This part has already lead to the published article of reference [48], but more details can be found in this manuscript. We mainly use a dc current to study the dynamics in domain wall so one should remind than there is a factor $\sqrt{2} * \pi$ given by equation 3.10 between the measured and plotted change of resistance induced by rf and the peak value induce by the precession.

4.1.2.1 State of art on rf excitation of domain walls

As domain propagation reverses the magnetization, its understandings and control is of great interest for spintronics. That is why domain walls have been largely studied this last decade see references [49, 50, 17]. In particular, their dynamical properties in response to an RF field or current have been the recent focus of a significant research effort. Most studies aimed at affecting the domain wall (DW) depinning field by an RF excitation [51, 27, 17, 52, 53, 18]. The efficient frequencies depend largely on the domain wall type (e.g. vortex or transverse) or pinning properties [51, 27, 54, 52, 18]. Other measurements were concerned with finding the right width of a current pulse to optimally decrease the density required to push the domain walls [50, 27]. The frequency of importance are mainly those for an oscillation of the center of the domain wall. In the next part we will be interested in the rf induced resistive answer of the domain wall above relevant frequencies to propagate it(i.e. no change due to the rf excitation on the full resistance measurement).

4.1.2.2 A transverse domain wall

We use the (asymmetrical) constriction of our sample as a nucleation center to generate a domain wall. For this we use the fact that to go back to equilibrium the magnetization relaxes with the minimum change of energy. This means that after a planar transverse or near transverse saturation, the magnetization will relax along the border of the constriction thus generating a transverse head to head domain wall. The exact field angle is found to be very important in the reversal as any longitudinal component would tend to saturate the sample. Here, we choose an angle of 92° for the bell shaped resistive measurement of figure 4.7a. Indeed we obtain a high resistance level at zero field when the magnetization lies parallel to the stripe because of shape anisotropy. The curve is saturated above 10 mT but presents an opening between 4.5 mT and 6 mT.

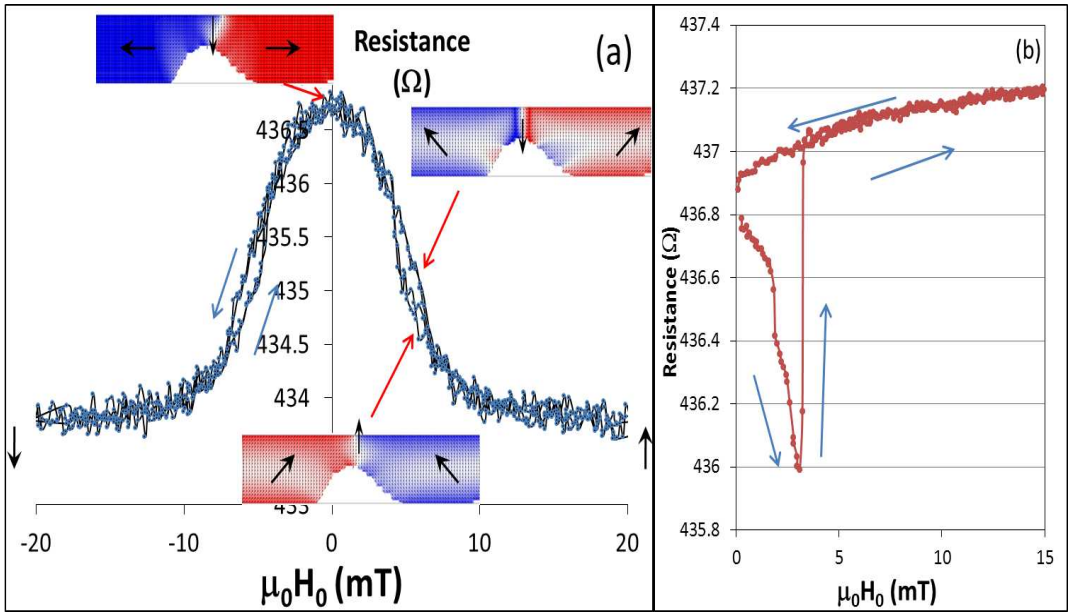

Figure 4.7: (a) Experimental measurement of the stripe resistance versus transverse magnetic field. The applied rf frequency as well as the dc current amplitude (here 15 GHz and 5 μA respectively) do not affect the shape of the curve. The resistance variation is consistent with simulations using the oommf package showing that a transverse domain wall nucleates as the field is reduced from the saturated state to zero field (blue and red are for magnetization pointing respectively left and right). This DW can then either be compressed or widened depending on (transverse) field direction resulting in a saturation at a different positive or negative field, thus generating the opening in the curve. (b) Resistance saturation as the applied field direction is changed to a longitudinal configuration. The starting level (low resistance) is thus the remanent state after saturation in a transverse field. The low resistive level (as compared to that of the zero field saturated state obtained on the way back from longitudinal saturation) provides evidence for the existence of a transverse DW decreasing the total resistance by about 0.2 Ω. Blue arrows indicate the direction of sweeping field.

Micro-magnetic simulations using the oommf package [55] helped us to understand the details of reversal and relaxation. For the simulation we used a cell size of 10 nm and as in the experiment the magnetic field is swept up to 1 T but zooming for points below 20 mT. We also added a small asymmetry in the designed notch to eliminate an artificial high symmetry of the problem not reflecting the real structures. The nucleation is due to the asymmetry of the constriction which forces the transverse magnetization to relax in opposite directions on each side of the notch (parallel to its sides and in the general direction of the applied field). Thus, a trans-

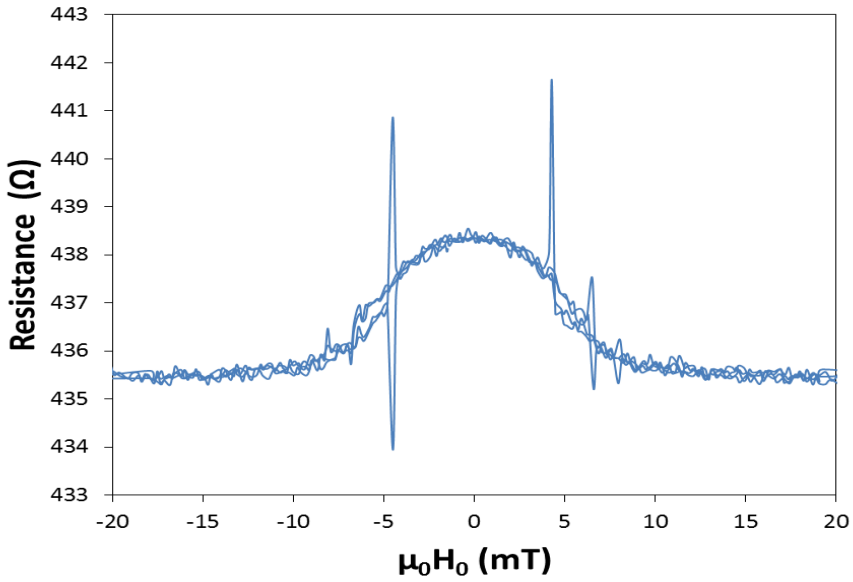

Figure 4.8: Experimental measurement of the stripe resistance without rf but with a dc current of 90 μA. We observe peaks, dynamical in nature, either positive or negative (compared to the global shape on the border of the hysteresis) when domain walls disappear or nucleate. The magnetic field is applied transverse.

verse domain wall (TW) can be stabilized at zero field in contrast with the saturated state obtained after a large longitudinal field was applied (see figure 4.7b)[17]. The difference in resistance state at zero field in figure 4.7b confirms the presence of a remanent domain wall after a saturation with an applied field of 92°. The domain wall is created gradually as magnetization relaxes in decreasing field but below 4.5 mT things suddenly accelerate producing a steeper resistance decrease which finishes the complete nucleation of the domain wall. The resistive contribution here results mainly from a slight change of internal field in the domains, due to the presence or absence of DW, able to slightly affect their magnetization angle. The information on the DWs is therefore mainly indirect, with nevertheless the contribution of the DW resistance itself. Its value of -0.2 Ω at zero field, as measured between the remanent state of a transverse or parallel magnetic saturation, is consistent with a TW of width around 150 nm.

Interestingly, under applied dc currents (up to 90 μA i.e. 7.5 10^6 A/cm^2), very sharp peaks can appear with the jump in the resistance, at 4.5 mT when decreasing the magnetic field and 6 mT when increasing it. These peaks are not systematically obtained and constituted of only one point in the measurement. Adding a waiting time before each point is acquired makes them disappear, which underlines their

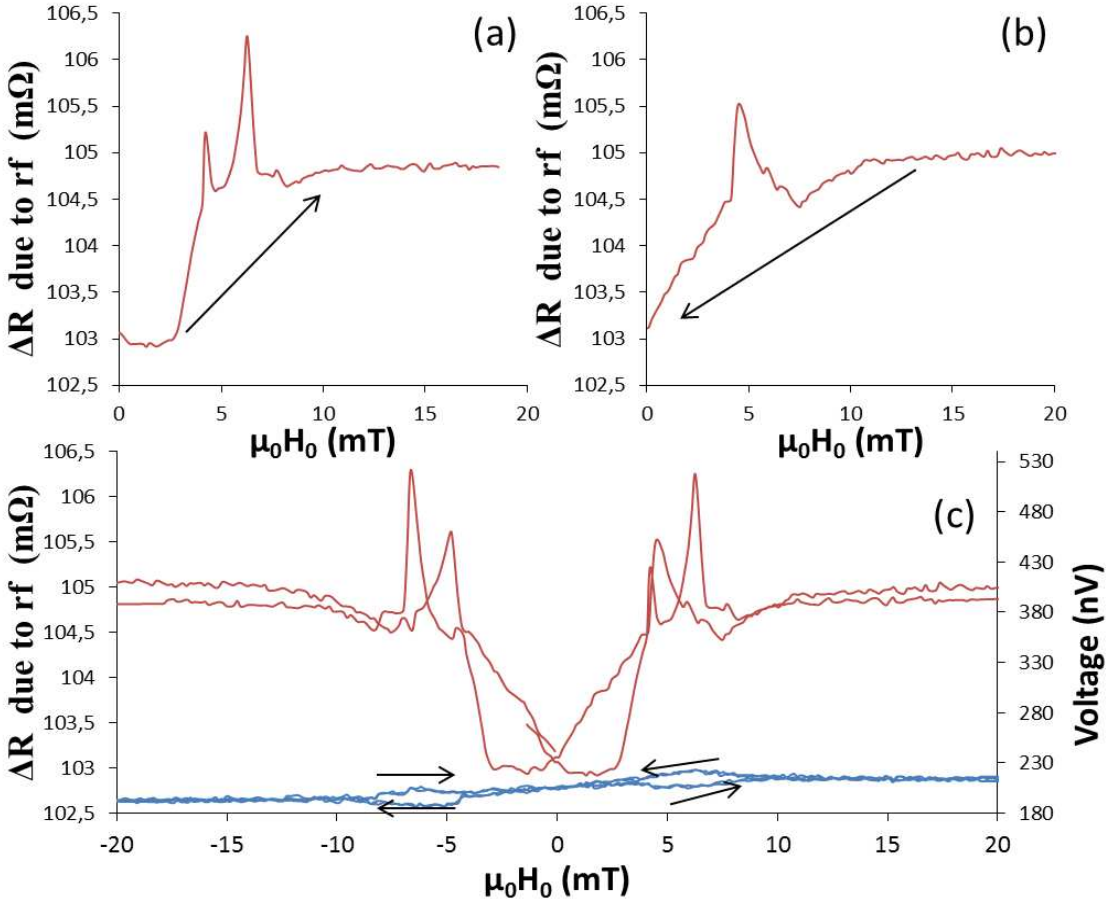

Figure 4.9: RF induced change of resistance measured at the frequency of modulation of the applied RF field with a DC current of 90 μA versus the transverse static magnetic field. (a) increasing the field (b) decreasing the field and (c) full sweep in field at a RF frequency of 15 GHz. Resistance peaks appear at fields where domain walls disappear and nucleate and a clear cycle opening is visible at low fields. The bottom blue curve of (c) is the rectified effect measured at zero DC current which is subtracted from the data in the previous curves to obtain a precise RF induced resistance.

dynamical character. This effect is then attributed to a transient voltage due to a dynamical displacement of an unsaturated part of the sample and enhanced by high current densities (e.g. 7.5 10^6 A/cm^2). The exact origin of this effect is not clear but a DC current and local variation of magnetization are required. We note that this effect does not occur for applied dc currents below 90 μA (all the ones used in this study) and is independent of the presence or not of a superimposed RF field.

The micromagnetic simulations show that when the field is applied parallel to the transverse magnetization of the wall (coming back from saturation), the DW tends to broaden, whereas a reverse field squeezes the TW. Such a difference in internal structure could only be seen in a measurement amplifying the DW contribution, as can be the case for resonant measurements.

Let us now consider in more details the rf induced change of resistance measured at the modulation of the applied rf magnetic field. The measurements are shown on figure 4.9. First of all, the signal of the rf induced resistive contribution behaves rather differently. The rectified contribution that had been subtracted is the blue curve in figure 4.9c. The hysteresis in the rectified signal is due to a coherent rotation of magnetization of the domains while reversing magnetization or relaxing it see part 3.4.1. It is also quite small and we can conclude that the bulk of the signal measured at the frequency of rf modulation is due to the rf induced resistance change, and does not come from a (rectified) variation at ω_{rf}. This dc variation of resistance between rf on and rf off is not due to a mere rf induced temperature increase which would replicate the resistive variations. Instead, one can notice that the zero field level is lower than the higher field one. Moreover, a clear cycle opening can be seen at low field which contrasts from the resistance behavior. The other distinguishable features are the positive peaks observed at the edges of the opening seen in the resistance curve. Hence, it appears that some extra information originates from the domain walls. This demonstrates that DWs, especially near their nucleation and disappearance, are more susceptible to RF radiation than saturated domains. The highest measured DW peaks reaches 1.4 mΩ to be compared to the 120 $\mu\Omega$ of the domains themselves. Presuming that AMR is responsible for the signal in the domain wall of 0.2 Ω, we obtain a resistance difference resulting from an average angular variation of 10° (using equation 4.1) for the wall's magnetization. We underline here that for a permalloy nanostructure of these dimensions, the displacement of the domain wall in the potential of the constriction is obtained at much lower frequency, around or below 1 GHz [18, 56]. We argue that our peaks are due to DW distortion, so it corresponds to a change of the domain width of 3% that is enough low so that AMR still dominates the resistive behavior of the domain wall.

We also analyzed the frequency dependence of the resistive signal and find that it only varies very little between 5 and 20 GHz see figure 4.10. This is at first sight surprising, but it is likely to originate from the variation of internal field inside a domain wall which provides a resonance condition somewhere within the wall for a broad range of frequencies. The fact that, corrected from the real power, the curves are well superimposed also confirm that despite of the low static magnetic field we are still in the linear regime.

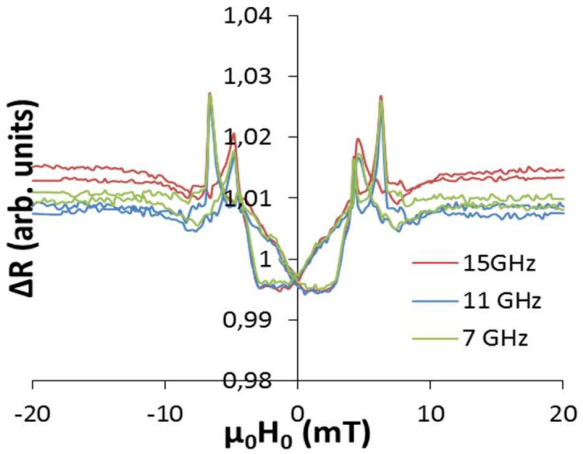

Figure 4.10: Frequency dependence of the measured rf induced change in resistance for the three studied frequencies of 7,11,15 GHz. To correct from the different rf power of each frequency, the resistance variation is scaled by its value at zero field. The obtained peaks have the same amplitude for the three frequencies.

4.1.2.3 Domain walls in parallel state

In this part we study the behavior of the magnetization reversal in a longitudinal magnetic field. There are two main interesting kinds of reversal: pure parallel reversal and reversal from a remanent state obtained after saturation by a transverse field. In that case, a TW is present at zero field as demonstrated above in figure 4.7. The magnetic field is swept up to 1 T.

In figure 4.11 is represented the evolution of the TW with a longitudinal field. The full resistance curve has a first negative jump at 2 mT, it corresponds to the transformation from transverse wall to vortex wall (VW). Indeed vortex walls are more stable in stripes with longitudinal fields as shown by simulations. Vortex are also broader with a magnetoresistance of about -1 Ω consistent with a width equal to the stripe's width. The rf induced change of resistance has also marks of this change with a negative jump and a positive peak just before the disappearance of the VW. The total height measured is this time 1 mΩ, which would correspond to 3° of precession (the vortex wall is larger than the transverse one) if all this change is due to precession inside the VW. Of course when the magnetic field is decreased from saturated state, this time there is no signal as no domain wall is nucleated by relaxation of a longitudinal magnetic field. On the rectified signal of figure 4.12 there is also a peak when the VW is present (resistive curve is flat. However there is only a small peak on the next reversal just before the end when a vortex is trapped on the constriction. It is likely that those peaks on the rectified signal just correspond to a slight change of the base line due to the presence of a vortex wall and not

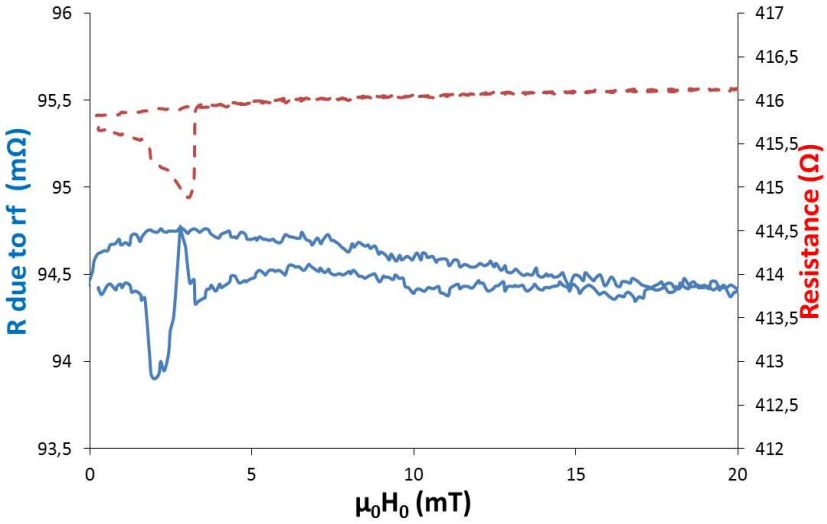

Figure 4.11: Resistance in red and rf induced dc resistance versus the longitudinal applied planar static magnetic field after a saturation with a transverse field. The rf frequency is 15 GHz and the dc current of 90 μA.

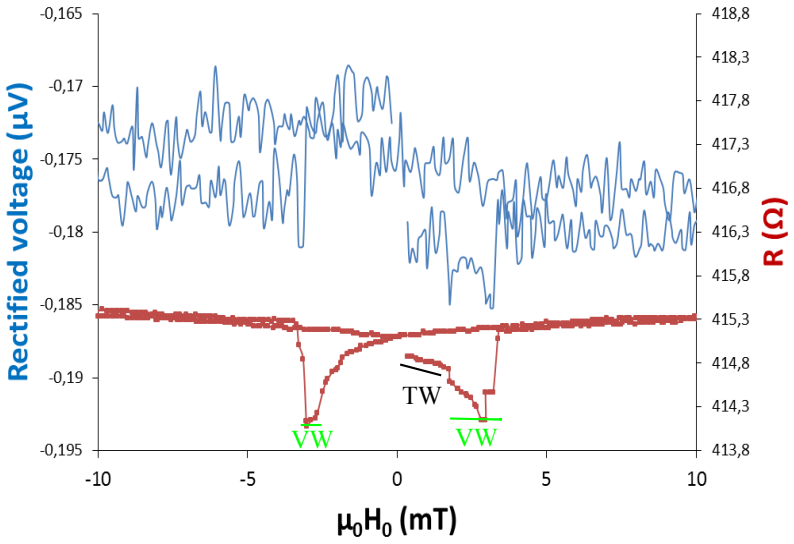

Figure 4.12: Rectified signal at 15 GHz in blue, full resistance in red versus the longitudinal static magnetic field. The starting point is the remanent state from transverse saturation

to magnetization dynamic of the vortex with an effect at ω_{rf} on the resistance. However the rectified signal does not provide more information, if not less, than the

full resistance measurement on the mechanism of magnetization reversal.

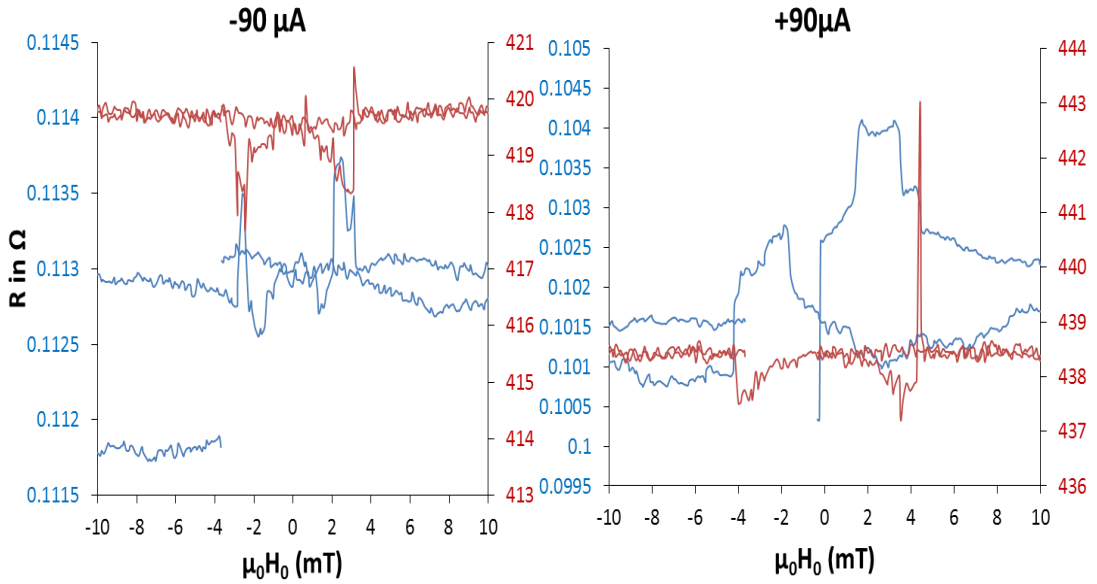

Figure 4.13: In red is the full resistance and in blue is the rf induced dc resistance. With a longitudinal static magnetic field, we compare the behavior for two currents + and - 90 μA and with a rf frequency of 15 GHz.

In figure 4.13, we plotted for a rf frequency of 15 GHz the full resistance and the rf induced dc resistance for two currents +90 μA and -90 μA which correspond to the average density under the constriction of 7.5 $10^6 A/cm^2$. First one notice that there are again dynamical effects at the end of the reversal on the full resistance measurement. The most interesting feature is that the reversal does not occur at the same magnetic field for both current directions unlike with a transverse field. With a positive current the reversal field is 4 mT with a negative one it is slightly above 3 mT (similarly to that without dc current). There is then a spin torque effect on the domain wall. The dc current gives a part from its angular momentum to the domain wall thus thus influencing its size and even pushing it. The symmetry of the reversing field demonstrates that one part of the stripe (always the same) must reverse before the other one and the vortex wall then created is stabilized beside the constriction. The rf induced dc resistance behaves very differently for the two currents. For the positive current there is a large positive peak during the hysteresis of the resistance. With a negative current there is a negative peak at the beginning which becomes positive at the end when a VW is probably present and distorted as in figure 4.11 where the rf induced change of dc resistance is similar. The origin of the large and high positive peak for a positive current should be in the fact that the current is working against the reversal of magnetization and so having

a different dynamic compared to the minus current where effects on the resistive curve are negligible. As for the vortex wall we obtained more information on the magnetization dynamics with the rf induced dc change of resistance measurement than with the full resistance measurement. When changing the dc current from +90 to +45 μA the reversal longitudinal magnetic field decreased to 3.6 mT, the rest remaining unchanged. This behavior (amplitude included after correction of the power)is the same for our two other frequencies 7 and 11 GHz. The amplitude of the magnetization dynamics will so be around 3(-),4(+)° depending on the current sign. And the dynamics itself, related to the shape of the signal, depend highly on the domain wall distortion within a high dc current.

4.1.2.4 Conclusion on domain wall dynamics

The change in resistance due to domain wall dynamics is a dc change of resistance induced by the rf, no significant rf change of resistance at the rf frequency(the one of the excitation) has been measured. The domain wall dynamics has been found to be one order of magnitude higher than the dynamic of saturated domain at the resonance. However in the range study there was no variation from one frequency to an other. The exact amplitude of the dynamics depend on the exact shape VWW or TW of the domain wall. The measured dynamics offer us more information on the domain wall than a simple resistance measurement. It is worth pointing out here that slight changes in the applied field angle lead to different curves especially near the transverse geometry as it change nature and/or position of the domain wall. This is consistent with oommf simulations showing that the stability, position and even presence of the DWs is sensitively dependent on the field direction. Several other measurements have been carried out in the course of this thesis work but we decided to select here the most illustrative one.

4.1.3 Summary for the thin sample

We have a good understanding of magnetization dynamics in uniformly magnetized domain with a sensitivity of at least 0.5° for the precession angle. On domain wall dynamics, the measurements, using the dc change of resistance induced by the rf magnetic field, do not seem to depend on the frequencies (above the pushing one). Therefore it provided more information on the domain wall and its dynamics than a pure full resistance measurement. In addition the DW dynamics seems to be one order of magnitude higher than the domain resonance no matter if the domain wall is a transverse or a vortex domain wall.

4.2 Thicker samples

We study here what changes when the samples are thicker and no longer behave as macrospins. We have tried different geometries with thicknesses between 20 and 40 nm. A large part of the differences from the thin sample is independent from the geometry. The main sample that will be discussed is that of figure 2.9a, made in 32 nm thick permalloy. It is composed of two subsamples: a stripe with a constriction and one without called hereafter constriction subsample and stripe subsample. Its AMR at 77 K is 1.2 % or 0.817 Ω. The measurements discussed in this paragraph concern this sample otherwise indicated.

4.2.1 Induced currents and precession angles

Our aim here is to characterize the amplitude of precession and try to estimate the induced rf current out of resonance.

4.2.1.1 Amplitude of precession

First let us verify that the excitation is roughly of the same amplitude as that of the thin 5nm sample. As in part 4.1.1.1 a dc current is passed through the subsample with a constriction. This time the current is 400 μA. The sample is at 77 K under He exchange gas to improve the temperature stability. We have carried out the measurement in the parallel and perpendicular states for both positive and negative current. This is shown in figure 4.14

First of all we can notice that the FMR peak for the two angles of $\psi = 0^o$ and 90^o are of opposite sign, hence corresponding to the expected change of AMR as described in equation 3.10. The difference in the absolute value of the amplitude (the perpendicular one is higher than the parallel one) is attributed to heating effect. First, one can straightforwardly confirm that the out of plane precession is negligible (even in this 30 nm thick sample) since equation 3.9 predict that otherwise the FMR peak should be bigger in the parallel state. In fact what makes the perpendicular peak larger is the temperature increase of heating at resonance due to the increase of rf power absorption that always increases the resistance. We can first quantify the RF induced heating.

To characterize the increase in temperature, we assume that the resistance changes linearly with temperature between 300 K and 77 K, which means for this sample 0.15 Ω/K. It is important to keep in mind here that the main source of heating is in fact due to the dc current. With a current of 400 μA the temperature of the sample is estimated to reach 98 K. The heating due to the rf power out of resonance is nearly independent from the dc current and amounts to 30 mK at a frequency of 17 GHz. Adding the amplitude of the measured FMR peaks divided by

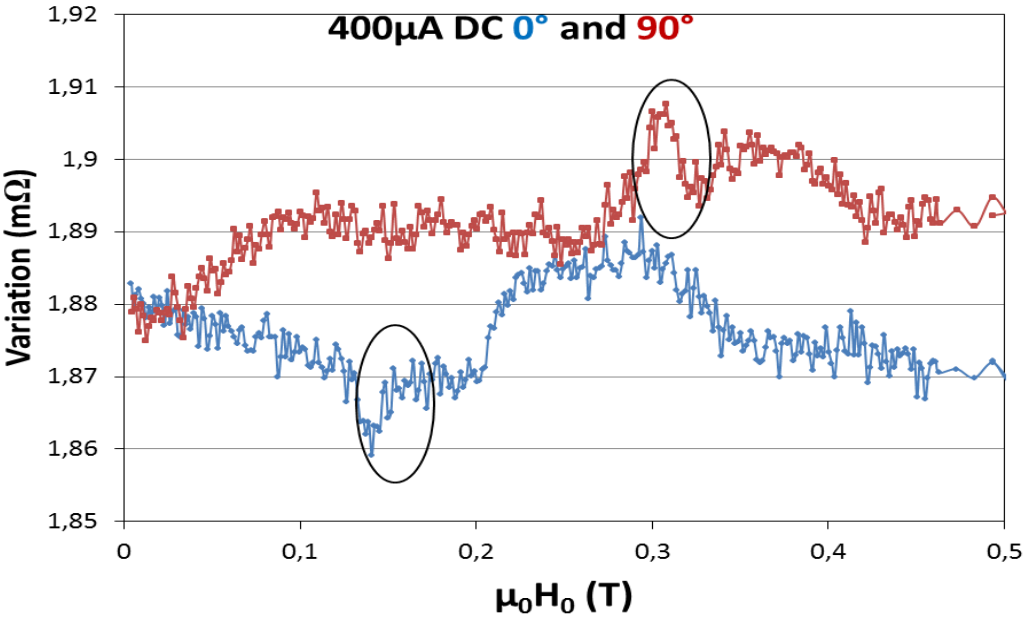

Figure 4.14: Average change of resistance due to rf irradiation measured using a dc current, versus the applied static magnetic field for two angles $\psi = 0^o$ and 90^o. In both cases we have made the average with plus and minus current to improve the signal quality.

two gives us the extra heating induced by the FMR, this value reaches 30 μK and thus is negligible behind the AMR contribution(indeed $30\mu K$ is nearly in the noise). This is very low compared to the prediction of reference [57] where the authors find that the heating dominates their signal.

Finally using equation 4.1 we determine the angle of precession to be of 0.4° (with 5% of error) at 17 GHz corresponding here to a rf magnetic field $\mu_0 h_{rf}$ of 0.12 mT. As expected this value of precession angle is of the same order as the one found in 4.1.1.1 where temperature effects were negligible.

4.2.1.2 Induced current

Figure 4.15 represents typically the angular variation of the rectified base level under the 1 T magnetic field. Its shape resembles a derivative of the AMR curve (also plotted) with the exception of the exact symmetry (the values for + and -90° are different). This shape can be expected for the rf induced rectified signal providing the ferromagnetic susceptibility is non-zero even if the magnetic field is far from the resonant one (1.5 T for 13 GHz on the sample of figure 4.15).

With a non-zero susceptibility when the resonance conditions are not fulfilled,

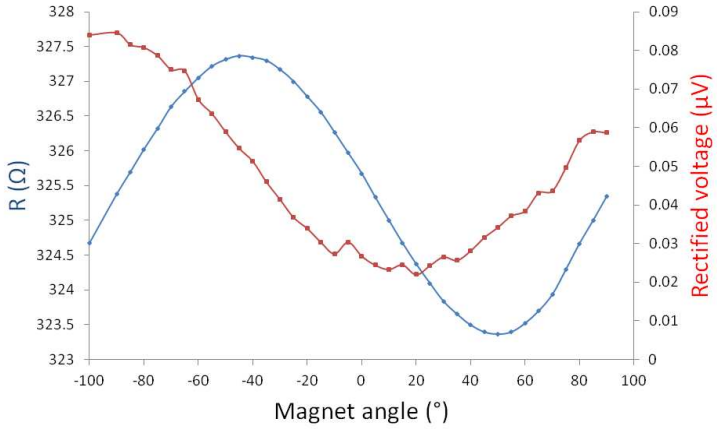

Figure 4.15: Variation of resistance and rectified signal with the applied angle of the 1T magnetic field. The resistance follows a typical AMR curve, and the rectified signal looks more like its derivate. The sample is a 40 μm long 420 nm wide and 25 nm thick stripe. The rf power is 6 dBm and the rf frequency 13 GHz.

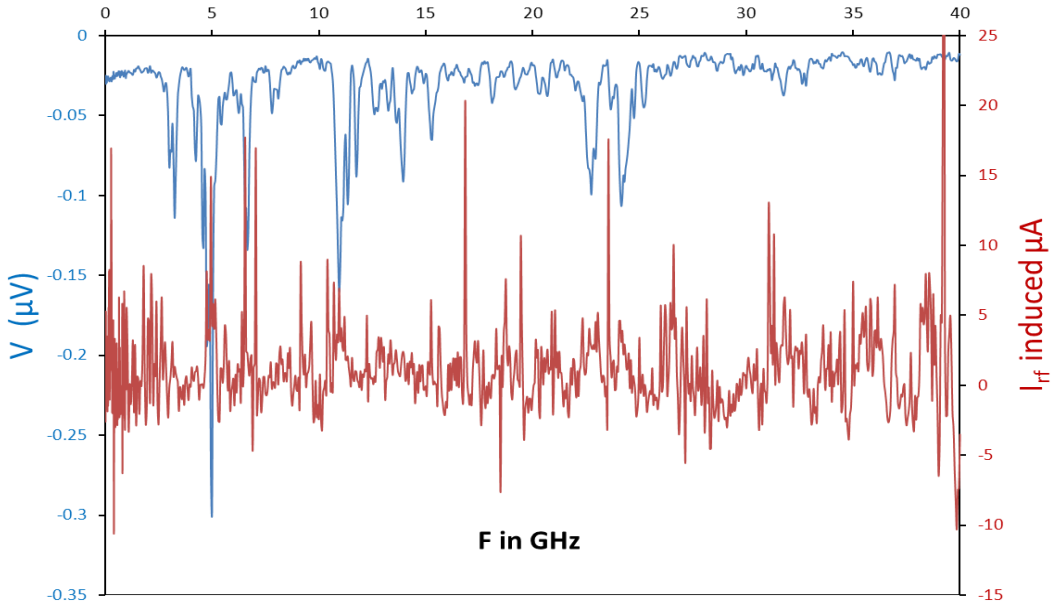

Figure 4.16: Estimation of the induced current versus frequency out of resonance.

we could estimate the induced current. To do so with a static magnetic field of 1 T and an rf power of 0 dBm, we carried out several measurements at 22.5° ($2\beta \approx 45^o$) and 0° with and without applied dc current. At 0° without current, $\beta = 0$ which determines a base line without rf excitation signal. We then use measurements with

dc currents to determine the residual angle of precession. Then we can estimate $I_{induced}$ mixed with the phase term. The results are shown in figure 4.16. It should be noted that even if the bulk of the estimation is in the noise, the average value of a few μA is consistent with a current induced by the magnetic flux variation generated by the rf magnetic field ($\mu_0 h$ $\sim$0.2 mT) through the device. An other interesting feature is that the current was found more important near 40 GHz. This is expected as this gets close to the resonance frequency of this sample for the applied magnetic field of 1T. The raw data were too noisy to determine precisely the non-resonant induced currents but the order of magnitude is consistent with a pure induction of the applied magnetic field as seen earlier.

4.2.2 The rectified signal

This part addresses the variations of the rectified signal. First we will present the RF field influence on the signal as observed through the effect of a damaged antenna. This significantly reduces excitation homogeneity thus influencing the rectified signal. Then the importance of the magnetization angle β will be presented. Finally the shape of the measured signals will be discussed considering the existence of several possible modes other than the uniform one. We will also address the expected field symmetries and in particular the parity of the measured rectified signal.

4.2.2.1 Damaged antenna

When the rf power is too high, the antennas can be damaged after a certain time. There are two kinds of damages. When the entire short end is sublimated, the rf currents are not flowing any more and the sample is useless. However, in the case of a more local damage, a signal can still be measured as shown in figure 4.17. The damage on the antenna influences the FMR spectra and, as it can be seen on the graphs, the amplitude and the shape changed too. Indeed the measured signal amplitude is nearly ten times smaller in that case. The damage on the antenna have also changed the angular phase Φ which in turn changes the peak shape from a nearly Lorentzian one to a more complicated form nearer to a derivative Lorentzian shape. A derivative Lorentzian is expected when the current in the ferromagnet is due to capacitive effects with the antenna (without any influence of the dc contact as there is no current inside) as it correspond to χ' in the susceptibility see part 1.2.2. So we assume that in the case of a damaged antenna like in figure 4.17 the induced current comes from capacitive coupling mainly thus confirming us than in normal conditions the induced current comes from flux variation (as explained in ref [46]). It also seems that in that case we observe a small shift of the resonant field. This could be expected as the damaged antenna produces an even less homogeneous

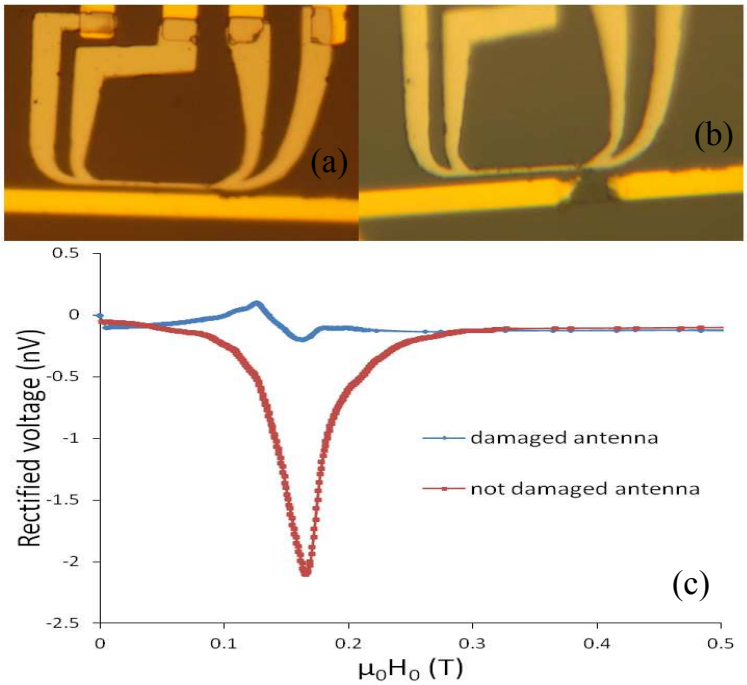

Figure 4.17: Comparison of the rectified signal with the antenna as fabricated or damaged. The Py of this sample is 45 nm thick and the central part is measured.

rf field on the sample.

4.2.2.2 Variation with magnetization angle

Before the antenna got damaged, we measured the evolution of the FMR peak with the applied field angle. We can clearly see that its position depends on the effective angle β. It is also interesting to note that the shape of the peak does not change with the applied angle. Its maximum is obtained for an applied angle of nearly 60^o. This position can be predicted (with the equilibrium position) as well as the global variation of amplitude changing sign for longitudinal and transverse fields. However the amplitude near the longitudinal position is too high when considering a fully perpendicular rf field. Thus, the transverse in plane rf component cannot be neglected as it is found greater than the 3° measured in the thin sample, which correspond to the geometric angle of the antenna field. We think this is the cause for the high asymmetry observed in figure 3.13 which was measured on the same sample (see next paragraph for more details on the origin of this planar rf field). The interest of the angular measurements is that they allow to estimate the effective demagnetization factor seen by the mode, if we suppose it uniform in the measured area. Indeed the demagnetization factor determines the equilibrium position (for a

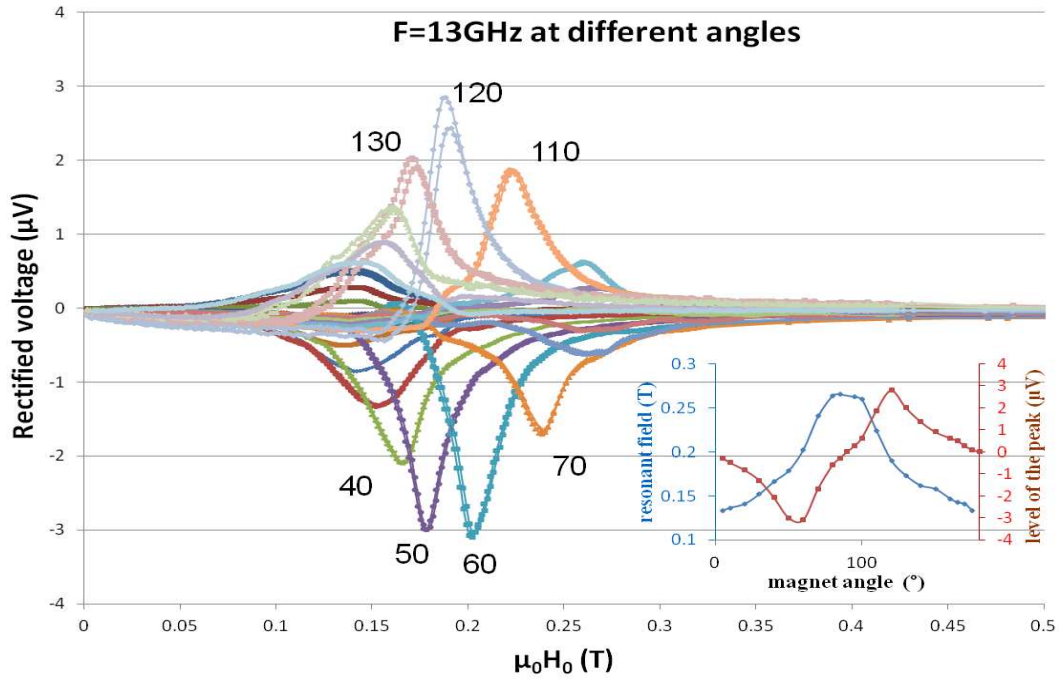

Figure 4.18: Rectified signal versus magnetic field at different angles at a frequency of 13 GHz. The inset shows the result of the resonant field and the amplitude of FMR peak for the different applied angles. The measurement is that of the center part of the image of figure 4.17 before the the antenna was damaged.

given geometry) and so the variation of the resonant field with the static magnetic field.

4.2.2.3 Mode and parity

We would like here to address the odd-even symmetry of the signal as well as the possibility to detect various modes other than the uniform one.

We measured at the same time the rectified signal of the constriction subsample (figure 4.19) and the stripe subsample (figure 4.20). The extraction of the odd and the even contributions is done numerically and it is found to be really useful. First of all the general peaks amplitudes are roughly an order of magnitude lower than those on the thin sample. This is expected as the AMR (in ohms) is 4 times lower, but it implies that the induced currents at resonance are similar (just divided by two in the thick one) in both samples. This implies that the total circuit impedance is roughly the same for the two structures. Considering that the resistance is 4 times lower, this hints at a domination of inductive effects (a capacitive coupling would have increased the rf current in the sample).

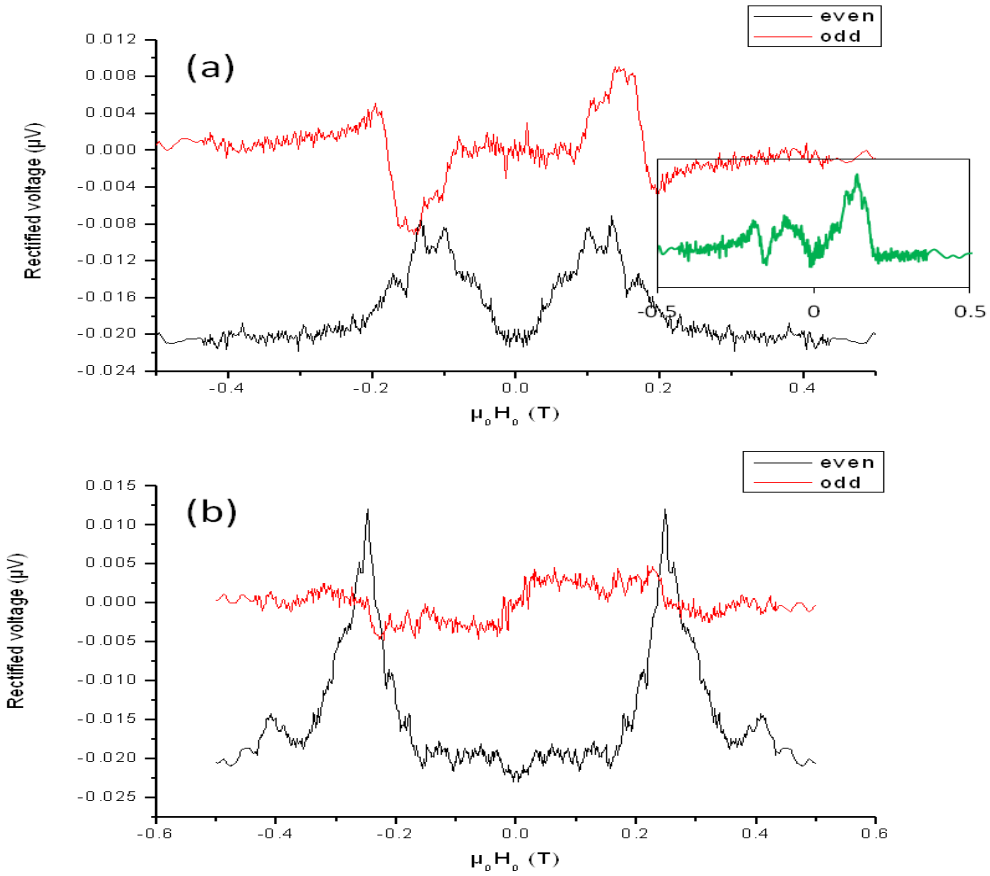

Figure 4.19: Measurement of the rectified signal versus magnetic field on the constriction subsample with (a) an applied angle of 25^o and (b) 80^o for a frequency of 12 GHz. We have separated the odd and even contributions to the signal to assess their relative evolution with the static magnetic field angle. The rf frequency is 12 GHz. The inset in (a) shows the raw data in green.

It is also quite obvious that the measured signal is composed of several peaks, which we attribute to non uniform resonance modes. Although the thin sample (from part 4.1) had a similar shape, its thickness was too low to allow for a visible separation of the modes see equation 1.29. Moreover, the in-plane demagnetizing factors are smaller for the thin sample and, as a result, the internal fields are more homogeneous. Hence, only the uniform mode is measured on the thin sample. The difference in resonant field between nearest mode is 37 mT against 44 mT given by equation 1.29. The difference should come to the fact that we are not able to separate clearly the two modes and that β is not 0° so the relation of equation 1.29 is no more efficient. Surprisingly the mode corresponding to a n even, as in equation

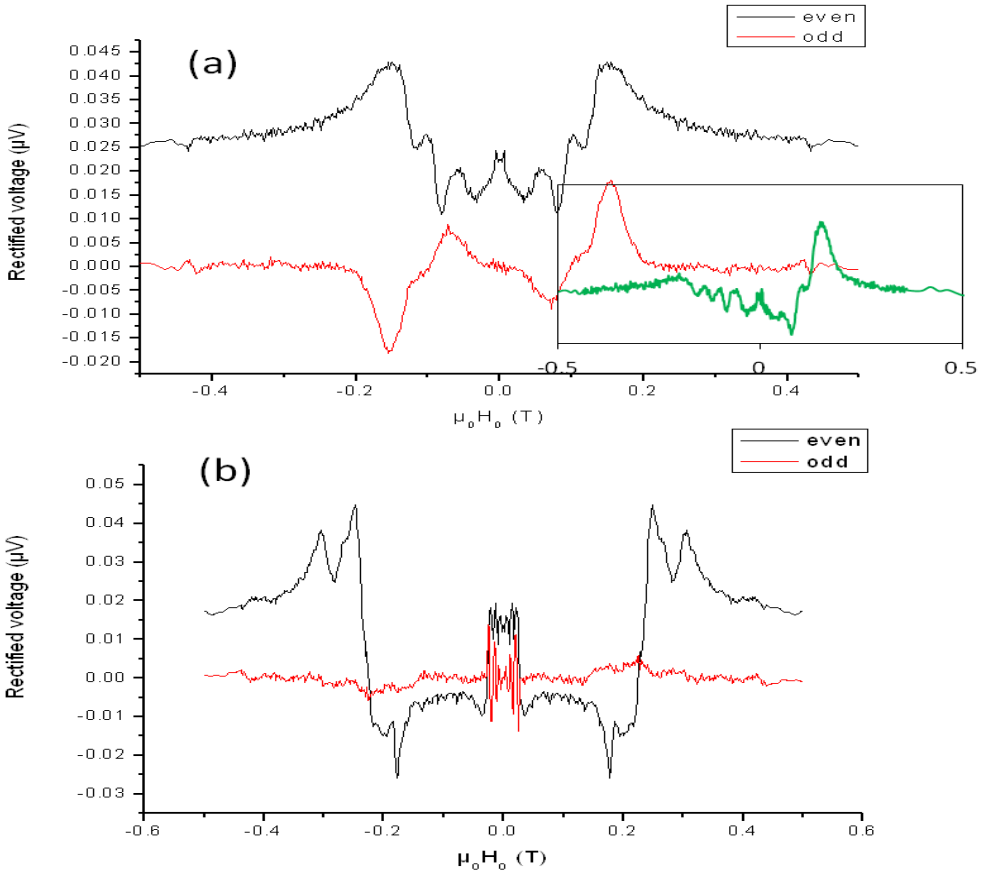

Figure 4.20: Same measurement as in figure 4.19 but on the stripe subsample. The inset in (a) shows the raw data in green.

1.28, can be measured. The excitation of such mode is due to the non uniform rf field (equation 1.27), but the resistive detection should be near zero (and difficult to measure) if the rf current are homogeneous in the sample. For other thicker samples with different geometry where contacts are also magnetic (see 4.17), non uniform modes have not been observed. It is likely that the geometry was not adapted to the establishment of many non uniform modes. Indeed the resonance corresponds to a collective excitation of the spins. If the sample has a too complicated shape, non uniform modes may have a too low susceptibility to be measured efficiently.

On the thick 'simple' stripe sample of figure 2.9a, the modes are broad and it is not clear that the uniform one fulfills its conditions of lowest energy (highest field) and most intense peak. Indeed at e.g. 12 GHz, there is a small mode at a higher energy than what looks to be the most intense mode. A local mode can possibly exist close to the border of the magnetic structure as the demagnetization field is

not uniform. These edge modes could be observed at a higher field. One should notice that at high frequency (30 GHz for instance) the susceptibility is probably too low to observe several modes, or they are less well separated. Mode apparition depends also on the equilibrium position as shown on the stripe at 25° and 80°. For a better understanding of this non uniform mode detection, one should make more simulations and calculus. But as the aim of thesis was dynamics in atomic contact, and so I did not have enough time during this thesis to study these modes in more details. From my point of view a better separation of these modes would be required for a reliable analysis.

The second interesting feature is that the odd part in field is more important for thick samples than for thin ones (of 5 nm in thickness). This odd part is decreasing relative to the even part when the effective angle β between $\vec{M}$ and the current lines is close to $\pi/2$. In terms of amplitude, the odd contribution is maximum for $\beta \approx 35^o$ for a given frequency. This is consistent with the existence of a significant planar component of rf field as can be seen in the expression of the odd contribution given in part 3.4.1. This cannot come solely from the rf magnetic field generated by the antenna. The other source of planar transverse rf magnetic field comes from the field generated at resonance by the rf induced currents themselves, providing they are slightly inhomogeneous in the thickness. These inhomogeneities of the current should depend on the frequency and so would the importance of the odd part at a given β, in consistence with the measurements.

We also performed measurements with cobalt (30 nm) instead of permalloy for the same geometry. As Co has a higher damping, the measured peaks are broader. The saturation magnetization is also larger, which pushes resonant fields at lower values for similar frequencies. We did not study this in much detail before starting the bending procedure as our final goal is the study of the FMR in atomic contacts. The main idea is indeed to compare, in the same conditions, with the ballistic atomic regime presented in chapter 5.

4.2.3 Domain walls

As shown in part 4.1.2 we can control the presence or not of a domain wall and our measurement techniques can provide us with a lot more information on DW magnetization dynamics than the full resistance measurements. In this part we concentrate on the rectified signal generated by the domain walls present as magnetization reverses. In figure 4.21 we tried to measure different states at zero field using the rectified voltage versus rf frequency.

In figure 4.21, the rectified signal of the resistance constriction subsample at zero field is plotted for three different states, versus the rf frequency in the range 0-10 GHz. The transverse domain wall is the remanent state after saturation of the sample by a transverse magnetic field. The vortex domain wall occurs when revers-

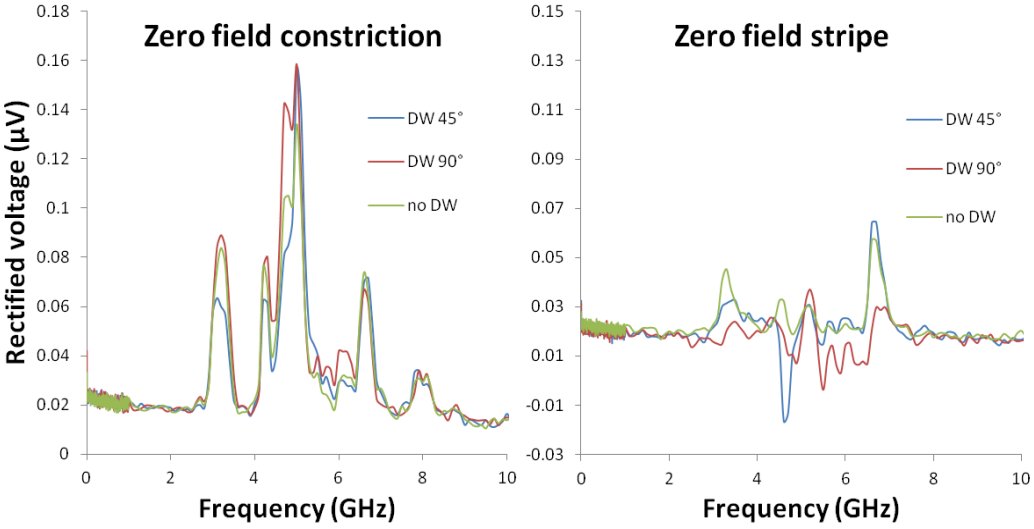

Figure 4.21: Different magnetic states at zero field with different domain walls: transverse walls obtained after saturation at 90^o (transverse field), vortex wall with a short sweep in 45^o field, and no domain wall after saturation with a longitudinal field. On the left the measurements have been carried out on the subsample with a constriction and on the right without; the measurement are taken at the same time on both subsamples.

ing magnetization with an angle of 45^o and then decreasing the field back to zero. The state without domain wall was obtained after saturation in the longitudinal state. The rf power was 0 dBm. We can see on the left part of figure 4.21 that there are large variations with the presence or not of a domain wall. However for the stripe without constriction, we do not expect such different magnetic states, but some differences can also be observed, although lower in amplitude. An interesting feature is that these differences are concentrated at the lower end of the frequency range, i.e. 3-7 GHz, where saturated domains are close to resonance at zero field. The width of the peaks and the number of modes can be distinguished in figure 4.19. For higher frequencies up to 40 GHz, differences are in the noise level if they exist. Let us look, in the following, at how domain walls influence the rectified signal while sweeping the magnetic field, for a frequency of 5 GHz.

The large global odd shapes of the rectified signal from figure 4.22 correspond to the FMR of the domains. There is a hysteresis even at zero field for the rectified signals of both constriction and stripe. Given equations 3.7 and 3.8 for the rectified signal we should not observe a hysteresis at zero field as magnetization is should be parallel to the main axis of the stripe. The only locations where it is not the case are the two extremities outside of the contacts. Thus in resonant condition these might

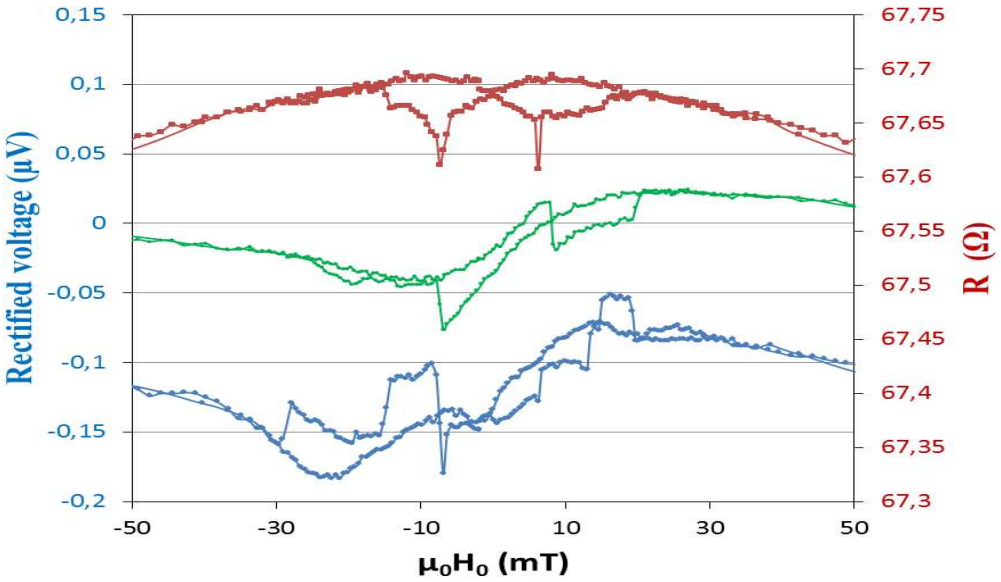

Figure 4.22: Resistance of the constriction subsample in red. Rectified voltage from the constriction and stripe subsamples in blue and green respectively. The frequency of the rf irradiation is 5 GHz, and the angle of the applied static magnetic field is 45^o

give us a small signal with a small hysteresis. Moreover magnetization reversal with domain walls may influence the FMR response of the domains. The hysteresis of the rectified voltage exceeds the one observed on the full resistance, especially in the constriction subsample. This could be explained either by the presence of some localized defects pinning the magnetization probably close to the constriction, or by non linearity effects (see below). For frequencies above the 3 to 7 GHz range, the only hysteresis at low field is due to the coherent rotation of magnetization of the domain. The rectified signals do not provide more information on domain wall mechanisms as peaks are obtained when domains are in resonant conditions.

Figure 4.23 show the rectified signal at 7 GHz from the sample of figure 4.17 where a hysteresis can be seen even without reversing the magnetization. The frequency of 7 GHz is resonant for a small enough static magnetic field and it is possible that the rf magnetic field cannot anymore be considered very small. This hysteresis might change with the rf power, but unfortunately the measurements for different powers have only been carried out for higher frequencies. We have shown in part 4.1.2 that for domain walls, the linearity is observed at low fields as there was no change of behavior for different power irradiating the samples. However for a quantitative analysis of the measured rectified signal of magnetization reversal

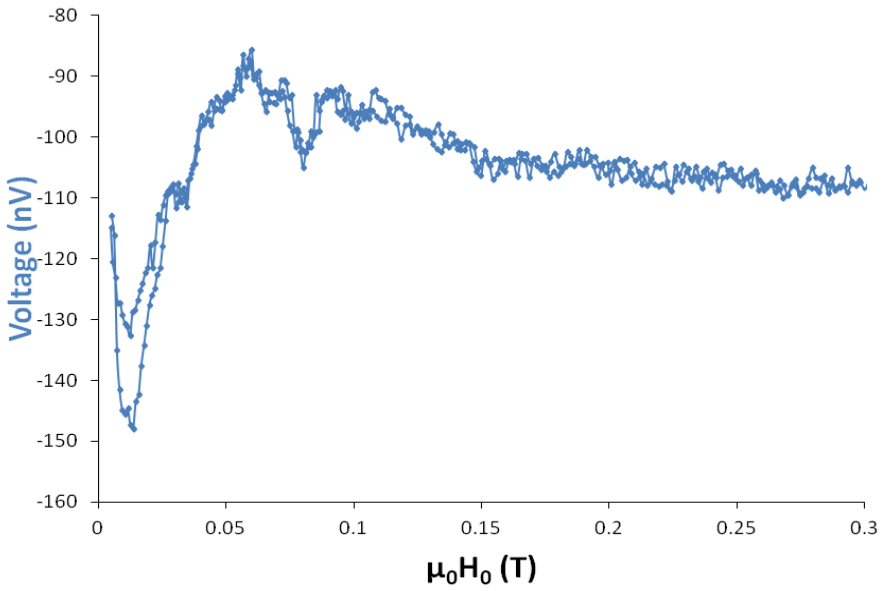

Figure 4.23: Positive field scan at 7 GHz and 9 dBm(sent) on the sample of figure 4.17. The hysteresis of the rectified signal is due to non linearity as the static magnetic field is too low. The magnetic field was swept only in the positive direction and the magnetization was not reversed.

for fulfilled resonant conditions for the domains, one should take into account the possibility of non linear effects on the domains even if for a low power (only 0 dBm output by the rf source for structures with two subsamples).

4.3 Conclusion on nanostructures

4.3.1 Magnetic domains

We have demonstrated our capacity to detect the ferromagnetic resonance of saturated domains. In the case of very thin layers (5 nm in thickness), the rectified contributions were fitted perfectly with uniform precession, leading to peak values of $\approx 200\ \mu A$ for induced currents. The rf field can be measured using the dc variation of resistance induced by the rf. It was estimated so to be a few 0.1 mT for a 1 mW (0 dBm) rf power. Fortunately, we measured the same value of rf magnetic field for thin and thick samples. However in thicker samples we were not able to fit the rectified contribution correctly as this would require an rf excitation field not perpendicular to the sample, with an in-plane contribution of 30^o versus 3^o for the thin ones. In measurements this is shown by the importance of the odd part of the signal with applied static field. This is measured for a small angle between the magnetization and current lines, as at 90^o the transverse rf magnetic field is unable to enhance resonance. This fitting problem seems inherent to samples as thick as 20 nm no matter the geometry. However the geometry (including the ratio width/thickness) plays a important role in our ability to measure other modes than the uniform resonance.

4.3.2 Magnetization reversal

A longitudinal field reversal does not show the same behavior as the transversal one. In both cases the use of dc current to measure the effect of the rf on the dc resistance provides a lot more information than the pure resistance measurement. We measured with rf frequencies above those required to help the propagation of the domain wall and found that the variation of dc resistance induced by the rf does not depend on frequency. The DW susceptibilities are higher when DWs are created or removed, and even higher than the one measured for saturated domain resonance at high field. Indeed if everything is due to AMR effects, an angle of precession of 10^o is obtained for the DW as compared to 0.7^o for the saturated domains.

It should be noted that this resistance variation of the DW is visible in the extra resistance in the dc state induced by the rf, and not at ω_{rf}. In that case, rectified voltages are only observed when domain resonances are expected at these low fields. It is hard to truly extract the contribution of DWs as they are likely to affect the domains dynamics when they are close to resonant conditions. Moreover one should take into account the possibility of non linear effects for the domain resonance.

Chapter 5

Down to atomic size

When dimensions of the magnetic material reach ultimate material sizes, e.g. in atomic constrictions, new behavior should appear because of the reduced dimensionality. The goal of this chapter is to study the evolution of the FMR while reducing the dimension of the magnetic material down to the atomic scale. In order to be sensitive to the atomic contact properties, we use electrical measurements (see part 1.3) and the rectified technique, which allow to probe the few atoms composing the constriction. In the following, we followed the procedure of reference [58] by not suspending the bridges to be broken in order to make sure that magnetostriction artifacts can be neglected. Indeed, this way, the free moving parts are limited to their bare minimum and magnetization induced size changes do not affect the contacts geometry. In a first part the first pulling process is studied and constriction sizes in the few nanometer range are explored. This is done essentially in permalloy samples because in its "bulk" (i.e. thin film) form, Py is the simple material with the best resonant properties. Then the atomic contact regime is studied in Co constrictions. When addressing atomic structures, it is indeed easier to deal with simple elements, as opposed to alloys, in order to circumvent the issue of the real chemical nature of the atoms forming the contact.

5.1 Reducing the constriction size

5.1.1 The FMR peaks

5.1.1.1 The induced current

In order to measure a modification of the rectified signal at resonance, either the resistance at the FMR frequency or the rf currents should change. For the latter, it is important to note that the breaking of a stripe hardly modifies the total electrical circuit geometry i.e. the surface to take into account for the generation

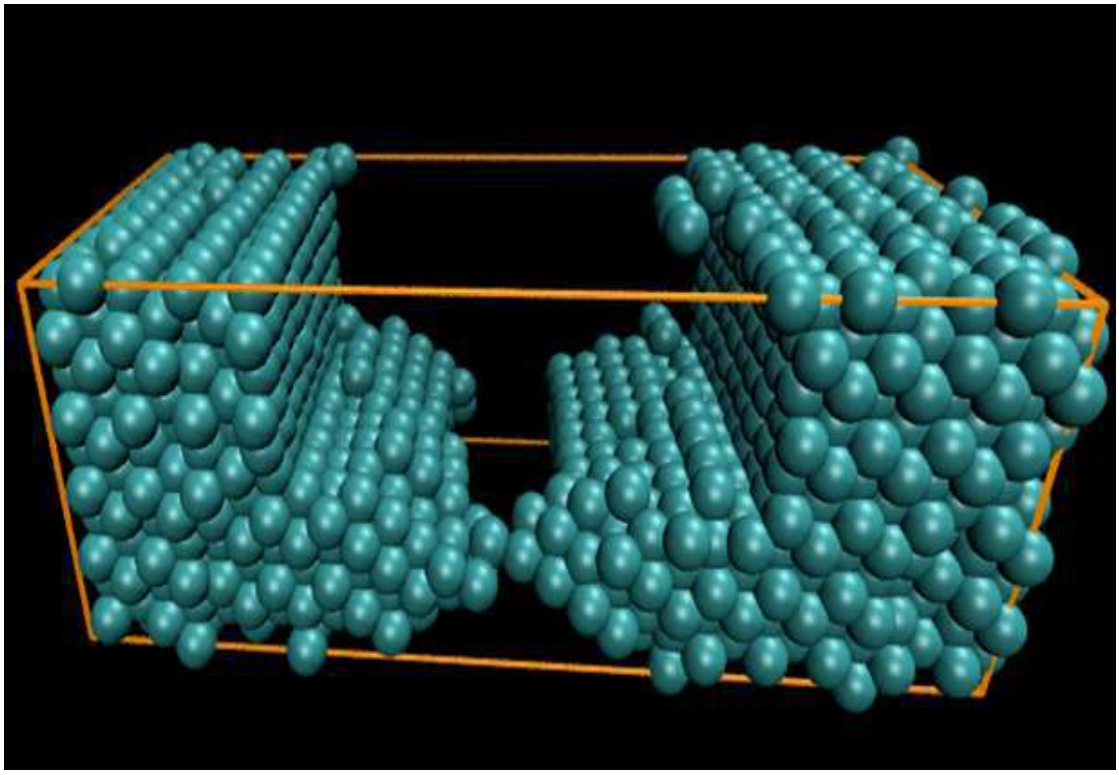

Figure 5.1: Typical geometry of a Co atomic contact as simulated by molecular dynamics by David Beaujouan and Pascal Thibaudeau from CEA Le Ripault. A stripe without constriction was pulled at a finite temperature and the last contact before full breaking is obtained at a random point thus giving an asymmetric atomic contact.

of induction currents. Most of the changes are extremely localized at the breaking point, as shown in figure 5.1. So the local increase of resistance will change the impedance seen by the rf current, but the flux remains constant. Thus the induced currents are reduced. An other change in inductance is given by the capacitance between atoms close to the atomic contact. However, given the small contact surface, the capacitance is too small to influence significantly the impedance compared to the dramatic effect of the local resistance. Moreover, these capacitances should not change at resonance therefore the rf current that is going through the capacitance does not give any contribution to the rectified signal. One can then conclude that the main change on the rf current in the ferromagnetic material comes from the increase of resistance. The domination of the resistive part of the impedance is actually confirmed by the observed constant phase Φ for all measuring frequencies in atomic contacts, in consistence with a negligible imaginary part of the impedance.

5.1.1.2 FMR modes

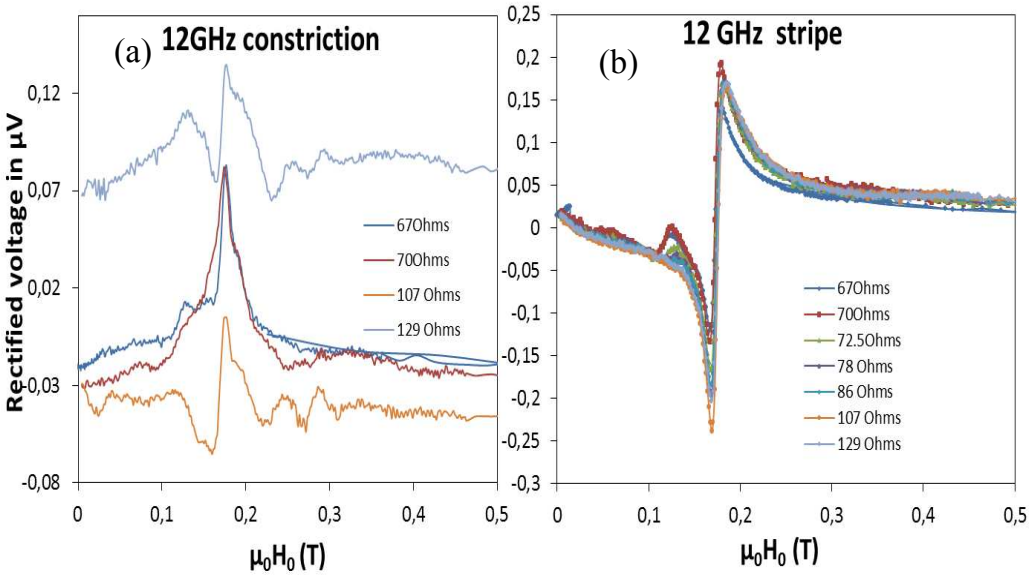

Figure 5.2: (a) Evolution of the raw rectified voltage for 12 GHz versus field applied at 65°, while breaking a Py stripe with a constriction as in figure 2.9(a). The resistance before breaking was 68Ω. The added 60Ω are localized in the narrowest part of the structure, i.e. in the constriction, which can be estimated to be about 3 nm in diameter. It should be noticed that the curves are not shifted and the base level varies with resistance. The FMR of the pure stripe of the reference sample (b) shows (almost) no evolution under similar strain as its resistance increases globally by only 1-2Ω (the color code corresponds to the one of the constriction).

While breaking the stripe, the FMR signal is modified and new FMR peaks appear as shown in figure 5.2(a). The stress is not responsible for these new modes as can be seen on the stripe without constriction, submitted to the same stress, where the FMR signal only slightly decreases. So these new modes on the stripe with constriction are concomitant with the increase of resistance up to 60 Ω, localized on the narrowest constriction. This corresponds to a ballistic constriction of about 3 nm in diameter. The new modes that appear are mainly at higher field, hence at even lower energy than the uniform mode. We attribute this general trend to the decrease of effective magnetic field in the constriction. Indeed, one can consider that at the constriction, the local magnetic geometry becomes roughly more circular which would increase the in plane demagnetization factor compared to that of the electrode.

An other interesting feature, is that the general amplitude of the modes de-

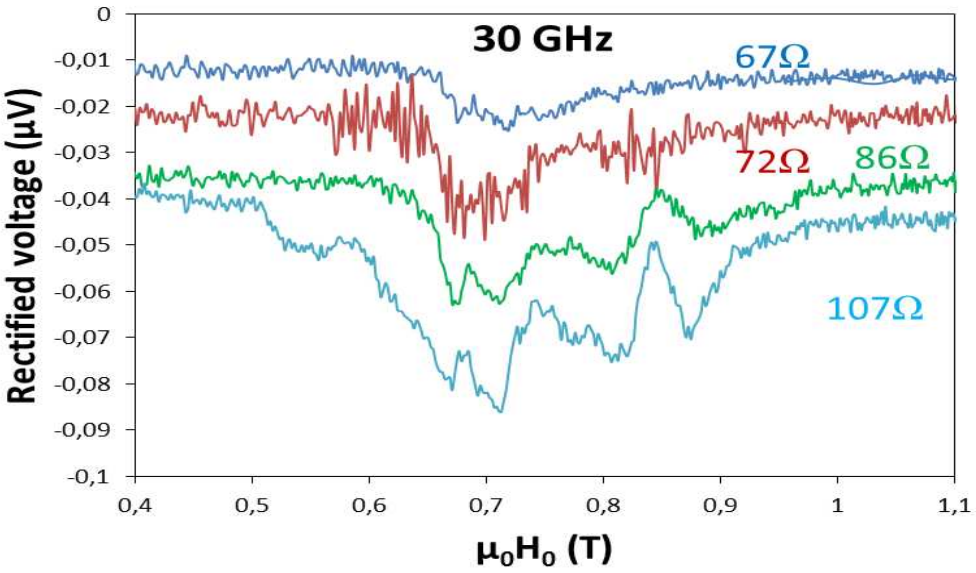

Figure 5.3: Evolution of the raw rectified voltage of the constriction subsample at a frequency of 30 GHz with a field angle of 68°. This time, the amplitude of the rectified voltage increases as the dimension of the contact is reduced. The starting resistance was 67Ω.

creases with the constriction size from the resistance of 107 Ω to 125 Ω. This could reflect the modification of the precession uniformity around the constriction, where the effective field becomes very inhomogeneous(along the constriction). The other contribution to the change of amplitude is that as β was near 45° before bending, an increase of the planar demagnetization field decrease β and so the amplitude measured (see equation 3.7). The slight apparent change of the peak shape also indicates that the rf current is influenced by this narrow constriction. At first, for a small increase of resistance to 70 Ω, the FMR peak is better defined and slightly more intense than that for the stripe without constriction. It is also interesting to notice that a base level increase is also associated to a very small constriction. This is a general trend observed on many samples.

These low energy modes are present at all frequencies, but high frequency measurements show them more clearly as shown in figure 5.3 for 30 GHz. As for 12 GHz, the modes that appear while breaking the stripe are mainly at higher field than before breaking even if a small new one also appears at lower field. Unlike at 12 GHz, the rectified voltage at the FMR field increases by a factor of 3.5 between 67 Ω and 107 Ω. This increase is partially due to the stress because even at a strain small enough to reach 72 Ω on the constriction stripe (and no change of resistance

on the stripe without constriction) the rectified signal at 30 GHz of both subsamples doubles. However the further increase of the amplitude on the narrower constriction (the stripe with only strain is constant after the small initial increase) might be due that at 30 GHz and 68° of applied angle when the domain are in resonance $\beta > 45°$ and the decrease of beta in the constriction increase the amplitude. This effect of the strain on the global amplitude is frequency dependent and its origin is not understood. However the apparition of new modes is not stress related as it only occurs in small constrictions.

5.1.1.3 The parity

The existence of a narrow constriction changes the resonance conditions as new modes are detected. In this part we will take a closer look at the signal, and its shape with the static magnetic field.

We performed measurements on the resistance level of 106 Ω for an applied angle of 80°. The narrow constriction is found to increase the importance of the odd part as can be seen in figure 5.4, knowing that the odd contribution was negligible before the breaking process. This increase of the odd contribution concerns all the modes, even those originated from the electrodes. This indicates that either the demagnetization fields have increased or the Oersted fields generated by the rf current near the constriction, have a significant planar contribution. In both cases, the planar rf field has a greater influence than before bending and the signal is due a collective response of the material to rf excitation. We are not able to fully separate the contribution of the constriction from that of the electrodes in the measurements. Indeed in the case of figures 5.4 at 12 GHz and 5.5 at 30 GHz both parts (electrodes and constriction) have a similar amplitude for their contribution to the resistance and probably also to the rectified signal. One should also notice that the most important peak is no more at the same position as the unbroken uniform FMR peak (still measurable on the stripe without constriction) for the applied angle of 80°. However, this is not the case for 60° where the highest peak was still nearly at the same field. This also hints at the importance of changes in the transverse demagnetization field and so the equilibrium position (i.e. the angle β for a given magnetic field) at the constriction during breaking. The local resonant mode(s) due to the constriction, and their modifications, dominate the FMR spectra with a small constriction between two electrodes.

It should be noted that these new modes were not observed if the magnetic material is submitted to a highly non homogeneous rf magnetic field (We remind you that we consider the field on the stripe as nearly homogeneous). In that case only the decrease of the uniform FMR peak (after a small initial increase) is observed. This decrease is less efficient in the absence of a local constriction in the measurement area i.e. when the deformation of the stripe is homogeneous, indicating the

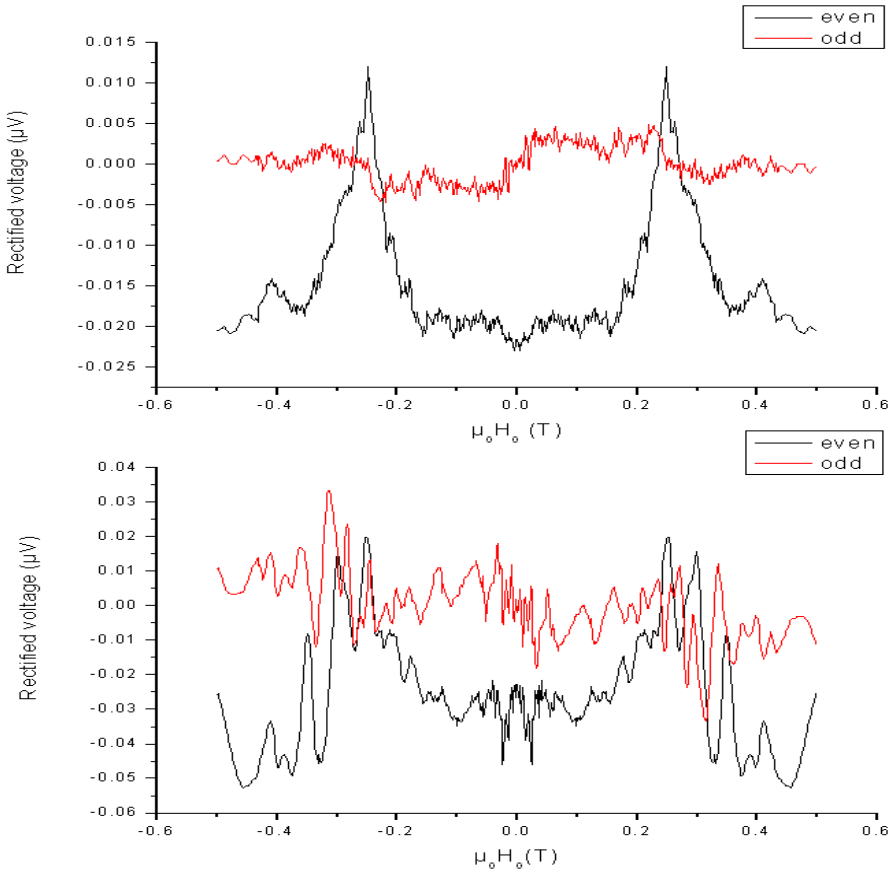

Figure 5.4: Comparison of the odd and even contributions of the rectified voltage in the stripe with constriction at 12GHz before bending at a resistance of 67 Ω (a) and during bending up to 106 Ω (b). The static magnetic field was applied at an angle of 80°.

importance of the magnetic coupling between both electrodes.

So far, we have not considered the potential effect of magneto-crystalline anisotropy. This is generally justified for permalloy nanostructures because of the near zero anisotropy of this material. However, it should be emphasized that at the scale of constriction sizes around 3 nm, it is questionable whether the alloy remains homogeneous enough to keep its property of very low anisotropy. Some preliminary measurements in TEM indicate that the grain size could be of this order and local chemical mapping using EELS spectroscopy also evidence significant stoichiometry departures on this scale. Therefore, it is possible that a reasonable anisotropy (of unknown direction) could be recovered at the contact. Interestingly, measurements

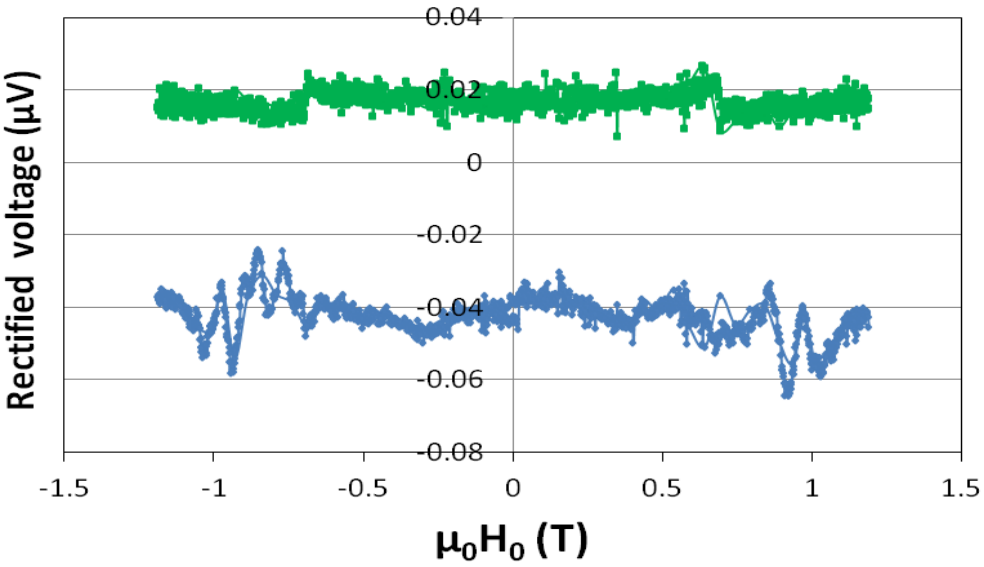

Figure 5.5: Comparison of the rectified voltage on the stripe with (blue line) and without (green line) constriction at 30 GHz for a resistance of 107 Ω. The static magnetic field was applied with an angle of 80°.

on a Co sample with the same geometry show a similar behavior: new mode(s) appear and the odd part of the rectified voltage increases for frequencies in the range from 7 to 26 GHz. The signal is also perfectly superimposed for both field sweep directions above 100 mT.

5.1.2 Magnetization reversal

We can see on figures 5.6 at 14GHz and 5.7 at 11GHz, that the behavior of the rectified signal is completely different from that of chapter 4. Indeed there is now a full hysteresis for some frequencies even at zero static magnetic field. This was not the case in chapter 4 where the hysteresis in the rectified signal was due to the coherent rotation of magnetization. Here, the magnetization relaxation in the constriction is neither completely reversible nor homogeneous, and the magnetic configuration is more susceptible to rf irradiation. We should also notice that the magnetization at zero field is not collinear to the current lines (otherwise there would be no signal at all). However for this constriction size, the values of the reversal fields are not yet influenced by the narrow constriction.

The ability for the (DC) resistance measurement to show a signature (i.e. a negative peak) of the presence of a domain wall depends on the frequency. For instance, we could not see it for 12 GHz in spite of the presence of hysteresis on the

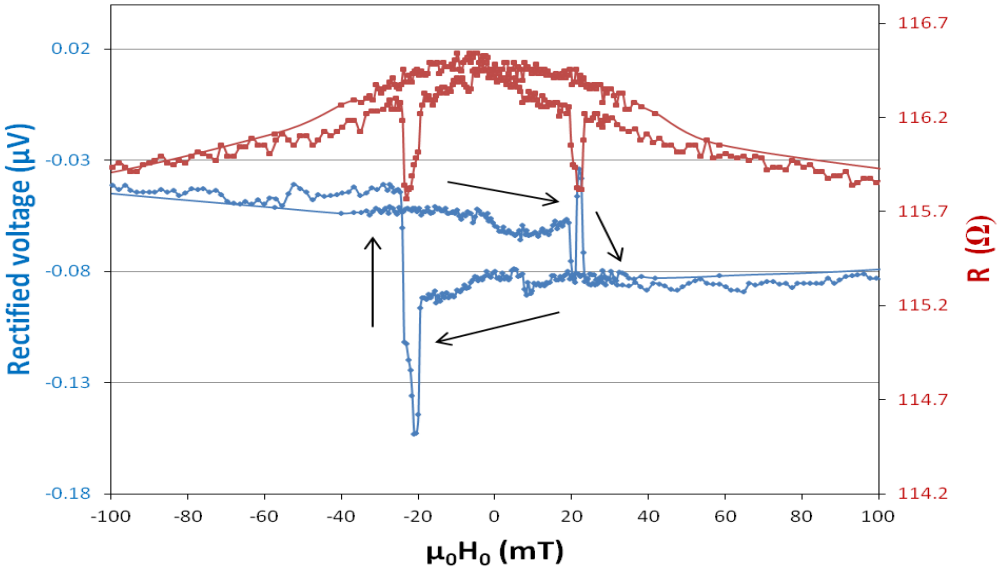

Figure 5.6: Measurement of the resistance (red) and rectified signal (blue), zoomed at low fields, for an applied field angle of 80° at 14 GHz. The hysteresis in the rectified signal is fully opened even at zero field.

rectified signal. The effects on the domain wall also depend on the frequency. For the DW in the negative magnetic field at 11 GHz we measured a positive peak but it turns negative at 14 GHz and its shape is different for a positive field. It is tempting to attribute this to the rf phase between rf current and rf resistance but in that case the position in the hysteresis at zero field should also be reversed; indeed the rectified signal is high after saturation with a 1T negative field for both frequencies, which is inconsistent with an exclusive phase effect. The hysteresis at zero field might be due to a global stronger anisotropy, of shape and magneto-crystalline origin, which prevents a 1T magnetic field to fully saturate the constriction.

In order to find out if this rectified signal is due to the magnetization reversal of the constriction or to the presence of a narrow domain wall, one should study it in more details. In any case, it is not a surprise that the dynamical properties of such small systems differ significantly from that obtained in a smoother geometry. A largely unknown effect concerns the exact influence of thermal properties on the base line: could they be influenced by the geometry of the constriction and if this is the case how could they depend so much on the frequency and magnetization orientation? These are very interesting and timely problems, but we did not have time to specifically address them during this thesis work.

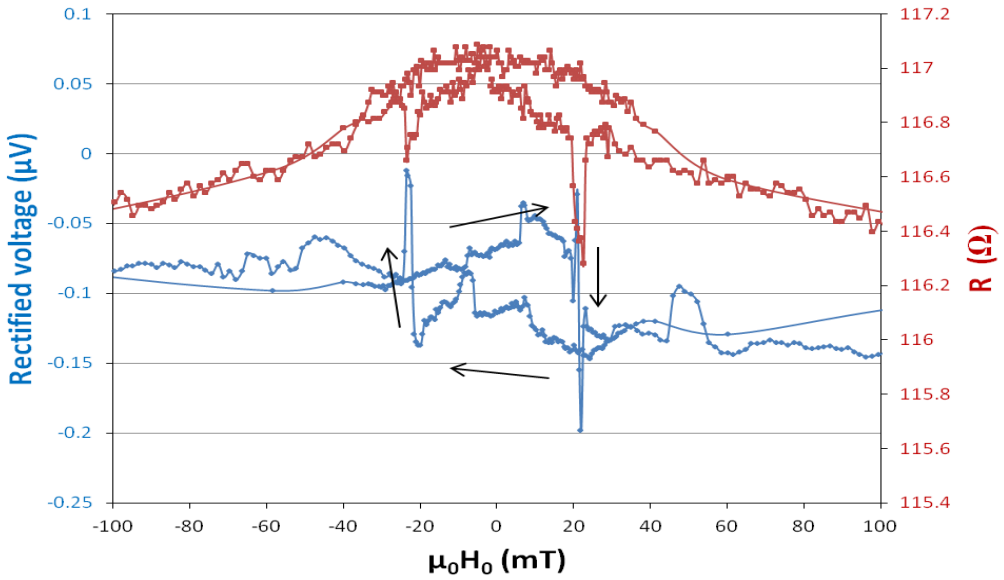

Figure 5.7: Measurement of the resistance (red) and rectified signal (blue), zoomed at low fields, for an applied angle of 80° at 11 GHz. The hysteresis is different from the one at 14 GHz of figure 5.6.

5.1.3 Conclusion

New FMR modes can be observed in the saturated domain while a stripe is broken. These new modes are thus due to the existence of a narrower constriction. It seems that the amplitude of the uniform mode is slightly increase by a small stress. While bending the substrate further, the amplitude is modified depending on the evolution of the effective field at the constriction. Indeed breaking the demagnetization factor in the constriction is increased resulting in a decrease of β. If the angle between magnetization and current lines (β) was above 45°, then a decrease of this angle would make it closer to 45° and would increase the peak amplitude. If the angle was below 45° reducing β reduces the peak amplitude. Because our goal is the atomic scale, we did not have time to understand if the sensitivity of resonant modes is changed or if it is due to new dynamic modes obtained in lower dimension coupled to magnetic electrodes.

In addition to the appearance of new measured modes, the symmetry of these modes is also modified. In particular the odd contribution is increased by at least a factor seven. As the odd contribution is due to the planar rf field, this increase indicates a either a global change of the demagnetization factor or a great influence of the constriction on the resonant modes including the uniform one. When the deformation of the stripe is homogeneous, i.e. there is no creation of a constriction,

then the amplitude decreased too slowly as the induced current is also reduced but there are no new mode detected or change in parity. The influence of magneto-crystalline anisotropy is not know and is questionable when the constriction sizes are below the 3-5 nm scale.

The magnetization reversal seems to produce an hysteresis in the rectified signal at zero field. We even obtain a peak on the rectified signal in the presence of domain wall, indicating a rf change of resistance. This was not the case before bending. Constriction narrowing can therefore modify a lot the behavior of magnetization dynamic at low field, when saturated domains are not in resonance.

5.2 Atomic scale

In the sample of figure 5.8(a) the structure was designed to break in the middle and we were able to measure the FMR properties of the three regions including the stretched electrodes (800-900 Ω). Their resonance was found to change very little with strain. However even in the ballistic (1.3 kΩ) area we could not measure a signal, not even the one of the electrodes on both sides of the contact.

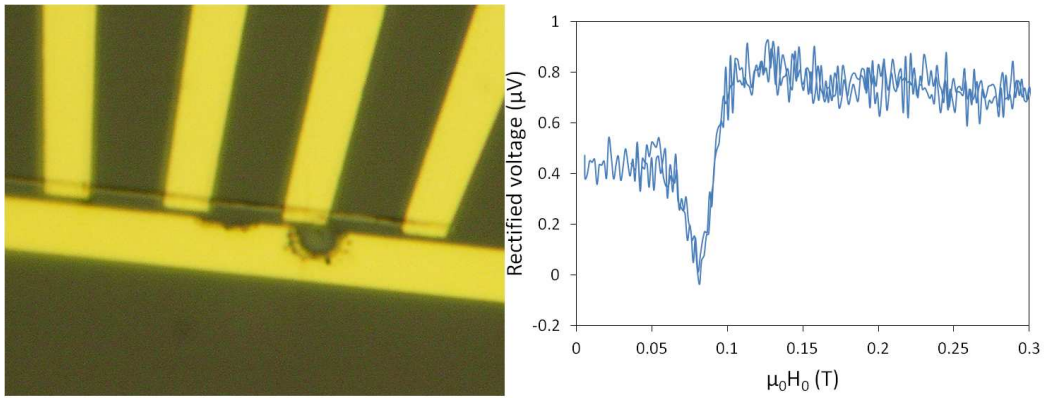

Figure 5.8: (a) optical image of a Py sample before the measurements, with a partly damaged antenna. (b) Rectified signal in the electrodes showing a resonance peak which did not change with strain.

As the structure was broken and a resistive contact established, three main features are observed:

- The rectified signal due to the FMR of the electrodes decreases until it reaches a level lower than the noise. This behavior is expected because the rf inducted current decreases as the resistance increases.

- The value of the baseline increases

- The resistance value decreases when the rf is on. This due to a heating effect as the thermal expansion is different between the metal and the kapton substrate.

For unknown reasons we did not manage to measure any rectified signal corresponding to the FMR of domain in atomic contact, perhaps it is due to the fact that we did not manage to obtain significant AMR in these atomic contacts too. However we managed to measure the resonance of domain walls in atomic contacts in a cobalt sample, we will discussed about it in the following. In this cobalt sample, with a geometry similar to figure 2.9(a), we broke the stripe without constriction. The measurements respected the 3 features above so there is no doubt that there was a local atomic contact.

5.2.1 A contact at 26 kohms

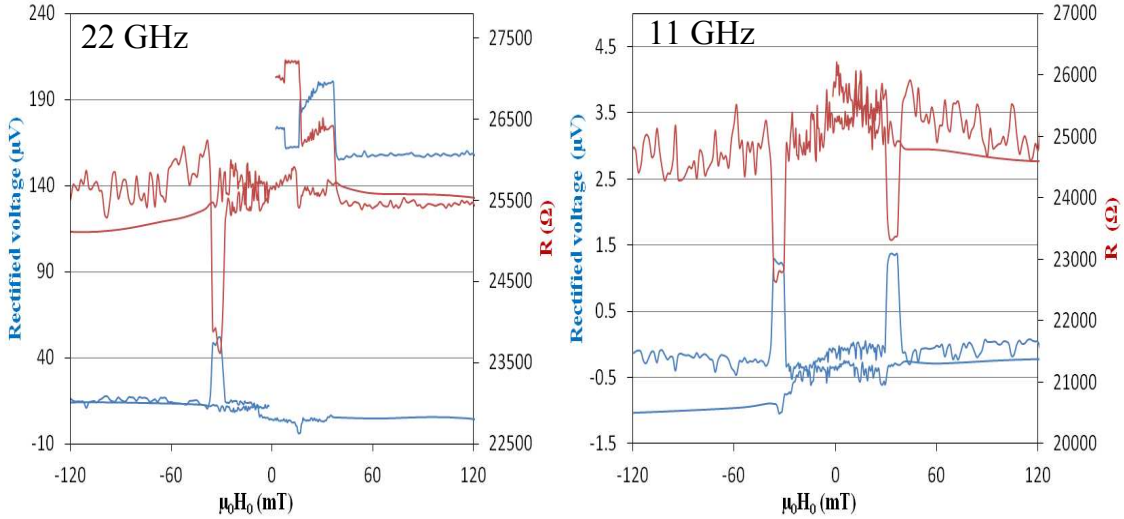

Figure 5.9: Measurement at two frequencies, 11 GHz and 22 GHz, of the rectified signal (blue) induced by the rf and the magnetoresistance (red) during external field sweeps in an atomic contact of conductance close to the quantum value. The magnetization reversals lead to a negative signature of the order of 9% attributed to a domain wall effect (the contact was not stable in the positive part of the 22 GHz curve).

A contact of $\sim$ 25500 Ω i.e. nearly 1 G_0, was stabilized on a Co sample. A domain wall with a resistance of roughly ~ -1800 Ω can be observed when magnetization reverses while sweeping the field at an applied angle of 45°. The DW magnetoresistance corresponds to a decrease of the resistance as for a classical AMR domain wall see figure 5.9. From ab-initio calculations [2] we know that a large AMR contributions (i.e. resistance maximum in parallel configuration) can arise if there is one atom in a 1D geometry as explained in part 1.3.2. The domain walls were obtained between 28 mT and 36 mT, however in the unbroken state the reversing of electrodes occurred before 29 mT. This confirms that domain walls enter the atomic contact just after the electrodes switch their magnetization. This is consistent with a minority domain stabilized close to the constriction by the large possible stray field in this geometry. It should be noted that the magnetoresistive dc effects of the domain wall in our atomic contact with nearly 1 G_0 of base resistance, do not depend on the frequency and rf power. The first interesting feature is that a rectified signal can be clearly seen, induced by the presence of a domain wall. This is in contrast to the measurements before breaking (see part 4.1.2) where no clear rectified voltage could be observed during magnetization reversal. The peaks

are thus attributed to the magnetic susceptibility of the domain walls. It is indeed unlikely that they correspond to a change of the base line level due to a change of resistance as this would produce the opposite effect (the baseline was observed to decrease with resistance). It is also interesting to notice that this baseline can dramatically change level with an atomic rearrangement causing only little resistance change as what happened for the positive fields of figure 5.9 for 22 GHz. This impressive effect is not understood.

The peaks on the rectified signal due to the domain wall were measured positive for all frequencies, irrelevantly of the RF current phase in the unbroken state. This shows that in atomic contacts the phase of the induced current can be considered independent from the frequency.

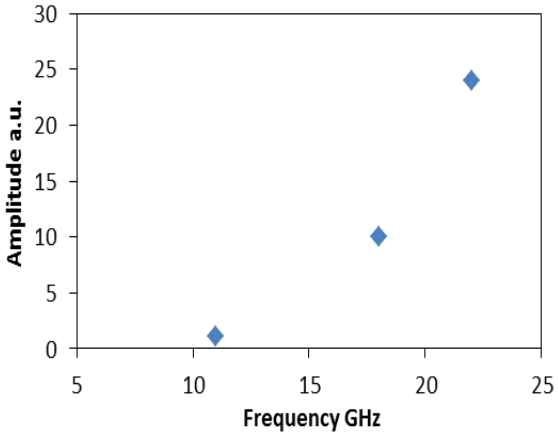

Figure 5.10: Summary of the DW peaks' amplitudes at $1G_0$, corrected from the estimated rf power for each frequency (estimated using resistance measurements of the unbent stripe). Measurements could be carried out for 22, 18 and 11 GHz before the contact closed.

The peaks on the rectified signal are between 28 mT and 36 mT for all measured frequencies 22, 18 and 11 GHz. The rectified peaks amplitudes are shown in figure 5.10 after correction for the RF relative power for the different frequencies. The highest is obtained for 22 GHz: 4 times higher than the one of 18 GHz and 25 times above the one at 11 GHz. We conclude that in atomic contacts the DW resonance amplitude depends sensitively on frequency. Qualitatively, one can imagine that the effective magnetic field in the domain wall is highly inhomogeneous, even more than in the continuous stripe domain walls studied in chapter 4. A resonance condition may be found at some specific position in the wall which also depends on its precise geometry on the atomic constriction. The resonance results locally in a precession of the internal spins at the contact level. The angle of precession of the

domain wall spins (supposing a resistive angular variation similar to bulk AMR) is at least three times the one obtained in a saturated domain before establishing the atomic contact.

Therefore, we demonstrate here that the high value of DWR close to 10% (about the maximum expected and measured for Co atomic contacts, see part 1.3.2.2) allows to generate a measurable resistive signal resulting from the magnetic response to the RF excitation. This is in contrast to what we measured in unbroken stripes. A clear frequency dependence is observed but not understood, and it is clear that some theoretical work is needed to go further in the analysis. Noticeably, no peak of domain resonance has been found for the three frequencies at magnetic fields lower than 0.5 T for which it occurs in the unbent samples for frequencies lower than 28 GHz as shown in figure 5.11. One should notice that the FMR peaks of the electrodes from both sides of the atomic contact could not be measured as they are expected to be in the noise of the rectified voltage baseline (the rf currents being too small).

5.2.2 A contact at 11 kohms

Now let us study what happens in an atomic contact of nearly 11 kΩ with a field angle of 70°. We measure the resistance and the rectified voltage at four frequencies 22, 18, 11 and 7 GHz and various rf powers delivered by the source. The domain wall has a positive resistance (opposite to that of the 1 G_0 conductive state of the previous part) of 140-160 Ω which corresponds to ∼1.4% of magnetoresistance. The positive magnetoresistance means than the DWR dominates the domain wall magnetoresistance signal because of an ultra thin domain wall and a not too enhanced AMR (two *half atom 1D* perhaps like that of the geometry of part 1.3.2).

Negative peaks in the rectified signals clearly appear between 4 and 103 mT, and -4 and -88 mT for the 4 frequencies measured (at 0 dBm) as shown in figure 5.11. These magnetic fields correspond to the presence of the domain walls with positive resistance of figure 5.13. The shape of the signal is independent of frequency, like in the previous paragraph, even if the rf power is different (2.8 times higher at 7 GHz than at 18 GHz). It is also independent on the phase Φ between magnetization and current measured before breaking. In the unbroken state at 7 GHz, the phase was such that no hysteresis could be measured and the frequency was too low for domain resonance. Yet significant peaks are observed when in the atomic contact regime due to the DW resonance. One should notice that these peaks are here much higher for the domain in this 11 kΩ state than those of the 1 G_0 state, although the DWR was more important. This means that either the precession is more important or the angular variation of resistance is much higher in this 11 kΩ atomic contact.

From figure 5.12, the ratio of the rectified voltage peak amplitude with the frequency is different from that in the previous section. These amplitude variations

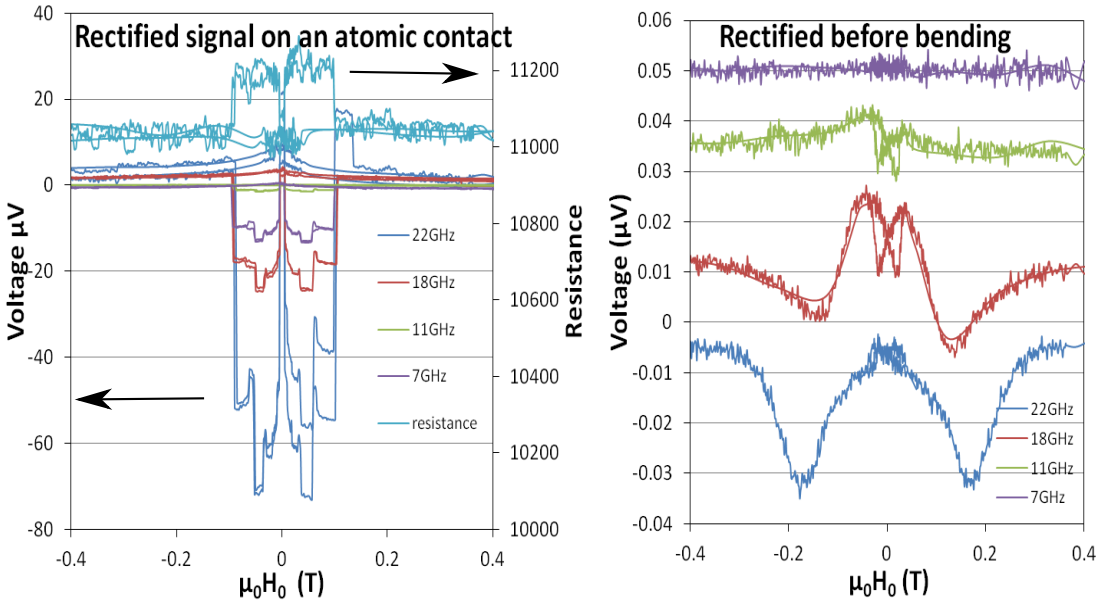

Figure 5.11: Rectified voltages in an atomic contact of 11 kΩ (left) and before bending (right) measured for 4 frequencies 22, 18, 11, 7 GHz. The rf power delivered by the source is 0 dBm. Note the very different scales of the voltage axes. The corresponding resistance curve is also plotted (in bright blue).

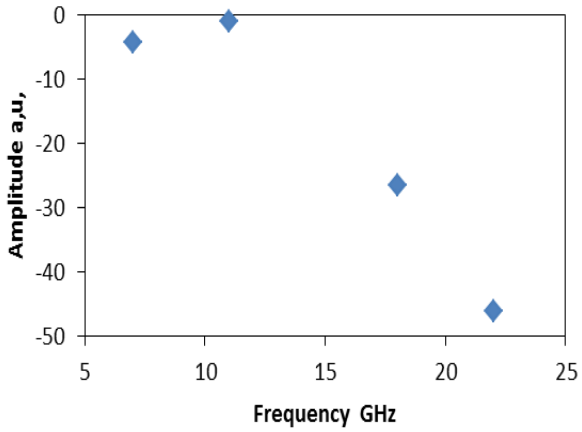

Figure 5.12: Summary of the DW peaks amplitudes for the 11 kΩ contact corrected from the estimated relative rf power of each frequency (22, 18, 11, 7 GHz).

with frequency are not simple and depend on the geometry of the atomic contact. However, one can notice that they both increase with frequency in absolute value. This seems to indicate that the DW resonance peaks are at higher frequency.

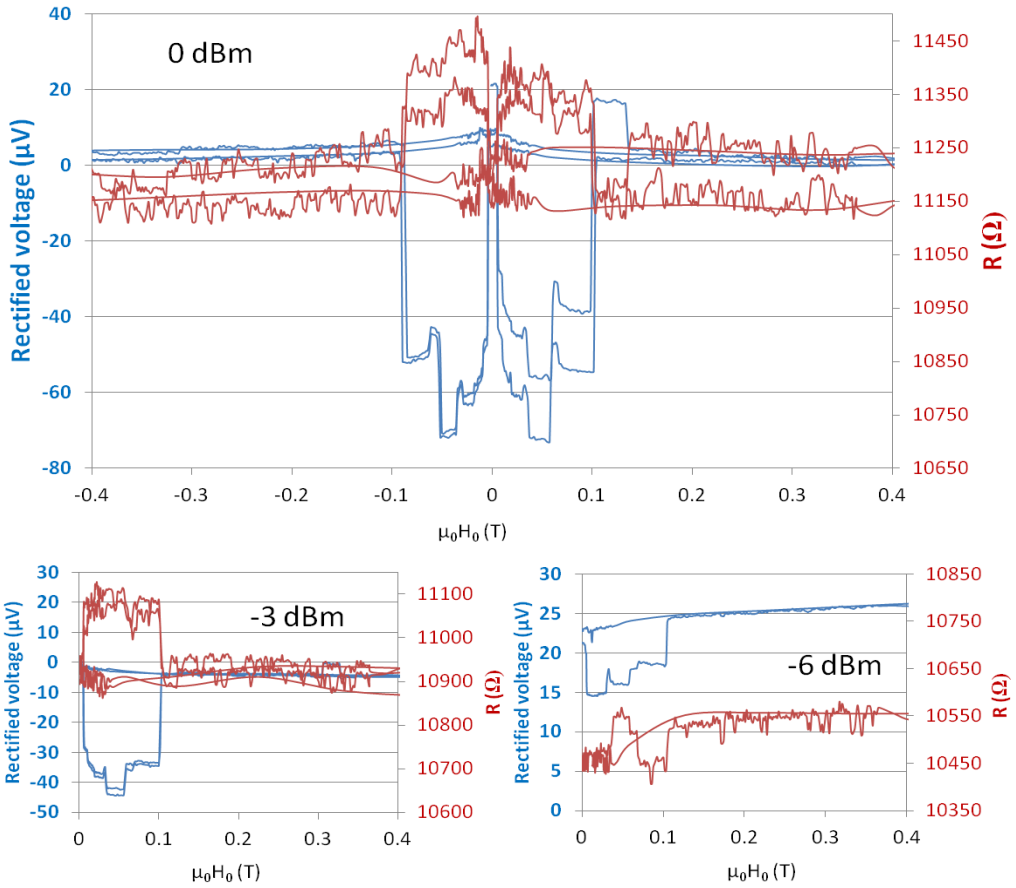

Figure 5.13: Rectified voltage for different powers at 22 GHz in blue. The corresponding resistance curves are in red. The domain wall resistance is positive at roughly 150 Ω or 1.4%, indicating a GMR like DW.

Figure 5.13 compares the variation of the rectified signal at a frequency of 22 GHz for three different rf powers. The two curves at 0 dBm or -3 dBm are very similar. The resistance at 0 dBm and -3 dBm have similar variation. The base resistance seems to decreases at lower power. However we said before that if we increase the power, due to the thermal expansion of metal and kapton which are different and as the cobalt is not suspended, kapton dominates and contracts the contact while heating. That is why a decrease of power increases the resistance, so that the change of the base resistance (of nearly 350 Ω) is due to a change in the exact contact geometry.

The rectified signals are in proportion, within a factor two, as expected for a linear excitation. The shape is also very similar confirming that the two contacts at 0 dBm and -3 dBm are nearly the same. These results are also confirmed at the other

frequencies (less noticeable for 7GHz). Indeed the measurements were performed in the following order 22, 18, 11, 7 at 0 dBm then -3 dBm and finally -6 dBm. In fact, the longer one waits since the stabilization of the contact the higher the chance that it becomes instable again with a noticeable change in the geometry. This mechanical instability of the contact is responsible for the change in behavior of the resistance for the -6 dBm power at 22 GHz. Indeed in figure 5.13 and -6 dBm, what could be identified as DW resistance effects begins only above 35 mT but the rectified signal is already in a negative peak. So even if the domain wall core is not exactly on the central atom, the rf excitation is enhanced. Because the resonance is a collective response of the domain wall and its nearby atoms, it is in principle possible that a signature could appear in the rectified signal without the corresponding one in the resistance. However as expected, the shape and the amplitude should be different if the DW is not exactly the same.

Quantitatively, we can estimate that the angle of precession (supposing an AMR like angular variation) of the domain wall is at least 20 times (at 22 GHz, around 15°) larger than that of domain resonance before bending the sample (about 0.75°). This angle of DW resonance is of the same order of magnitude as the one estimated in part 4.1.2. However, their mechanism of resonance is rather different because in atomic contacts, the signature is obtained in the rectified signal, i.e. at the rf frequency, whereas in magnetic stripes the effect was mainly an rf induced resistance change. Moreover, in the atomic contact regime, the signal amplitude is also found to depend on the frequency. Interestingly, the rectified voltage peaks are larger and much broader than those found in the previous atomic contacts presented before, in spite of an 8 times lower DW resistive effect than in part 5.2.1. The signal is therefore highly influenced by the shape of the contact as it also influences the magnetization reversal.

5.2.3 Back to contact

When an atomic contact is closed, the resistance decreases but the original continuous geometry is not fully recovered as the breaking can still be visible as can be seen in figure 5.14). Just after the 11 kΩ contact closed itself suddenly, the contact then reached a resistance value of 195 Ω.

In figure 5.15 we have measured the rectified signal for the frequency of 22 GHz in the new contact. Interestingly, a signal is found which closely resembles that of the atomic contact. Indeed it has the same shape, in the same range of fields, with an amplitude divided by 600. This is likely to originate from the same atomic contact as before, which is now in parallel to a new, lower resistance contact. The rf induction current crossing the atomic part being much reduced, one can expect a

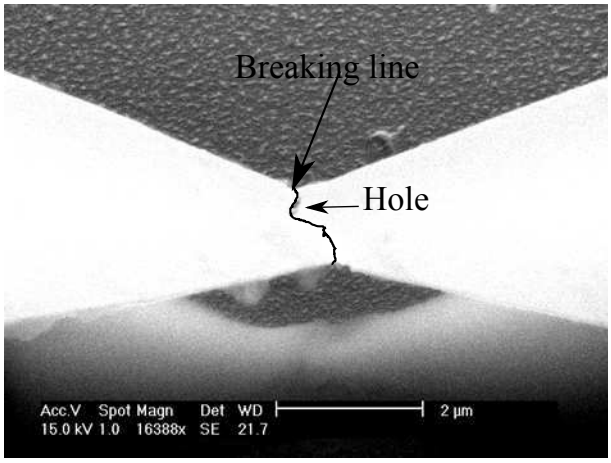

Figure 5.14: SEM image of a gold contact used in a MBJ where the geometry of the former atomic contact can be partially seen.

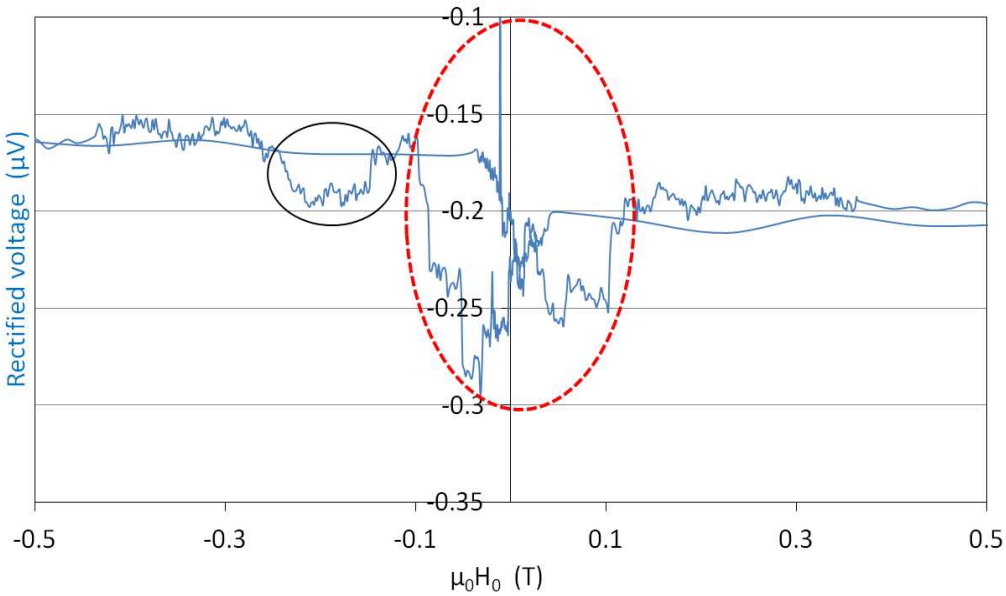

Figure 5.15: Rectified voltage at 22 GHz after closing the atomic contact of part 5.2.2. The area in the black ellipse is due to the FMR of saturated domain. In the red ellipse, the rectified voltage is due to the influence on the geometry of the former one at 11 kΩ.

similar but smaller rectifying behavior. The influence of the former geometry of the atomic contact changes with the time to reorganize the atoms in a more stable state. Hence, the different contributions are found to evolve in the scale of minutes. This

reorganization of the contact allowed us to measure the *atomic* reversal for only two frequencies: 22 and 18 GHz, but their relative amplitudes are identical to the one in the former atomic contact.

5.2.4 Discussion on resonance in atomic contacts

In order to draw any conclusion on the rf induced DW resonance in atomic contacts, it is essential to get theoretical support from ab-initio or tight binding simulations. David Beaujouan and Pascal Thibaudeau from the CEA 'Le Ripault' have developed a code gathering molecular dynamics with tight-binding calculations and spin-orbit effects. Starting from a continuous stripe and pulling on it, they have found the structure of figure 5.1. Once the atomic geometry is determined, it is possible to calculate the magnetic configuration at the atomic scale fixing boundary conditions imposing the presence of a domain wall. As expected, it is found (figure 5.16, that the DW is most stable on the thinnest atomic part and in this case, it is found to be about 6 atomic planes in wideness.

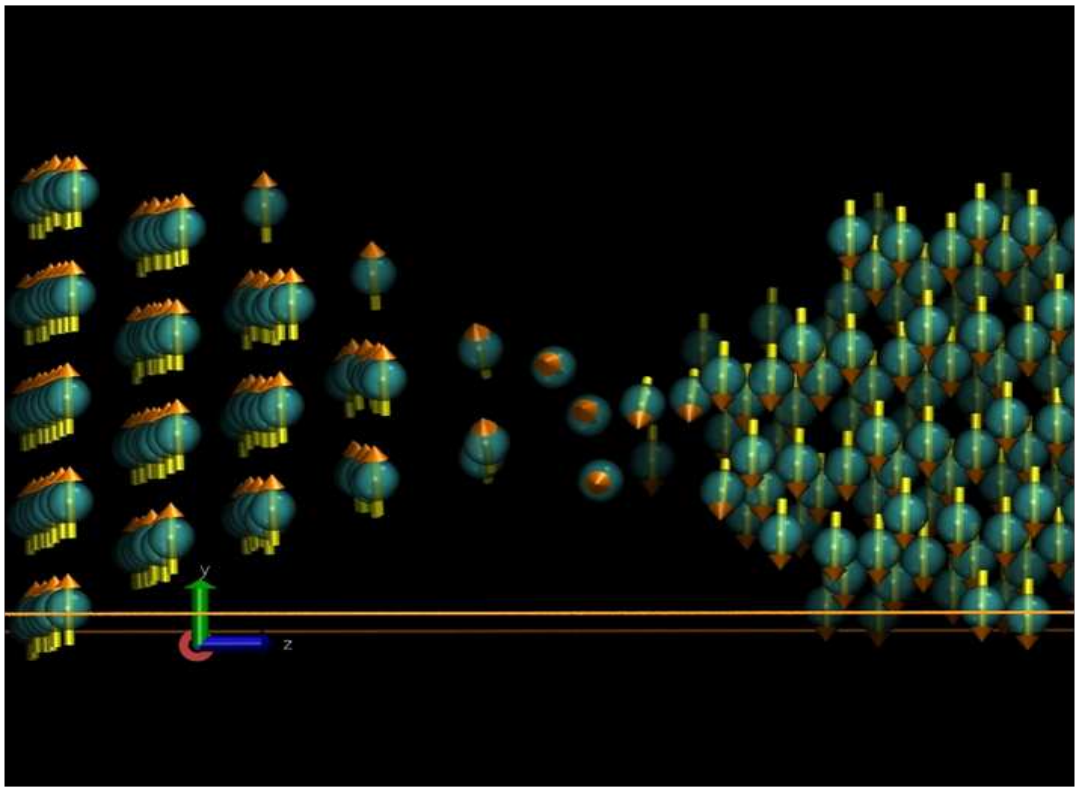

Figure 5.16: Image of a domain wall simulated in an atomic contact.

Experimentally, we have seen that the DW resistive signature can vary quite

significantly between different atomic contacts. We found a contribution of the order of a few10 percent on the 11 kΩ contact and a stronger negative contribution for 26 kΩ one. We first note that this is consistent with our present understanding of DW resistance in atomic contacts. Indeed, the ab-initio calculations of the CEA SPCSI group have demonstrated that large AMR contributions can be obtained in low-dimensional magnetic structures. It was shown that effects of several 10 percent can be obtained when a single atom is found in a purely one dimensional geometry, i.e. with only one neighbor on each side. Experimentally, we think this could be the case in contacts with low conductances, generally below the conductance quantum. In slightly larger contacts, we do not expect to find this 1-D geometry and AMR effects are expected to remain in the 1 percent range. Moreover, a DW resistive contribution of spin scattering origin is expected to exist in all contacts. It is due to the reflection of some minority spin electrons on the potential barrier of spin origin present in domain walls [36, 35]. Experimentally, this is also found to reach about 10 percent in the best cases. Therefore, it is reasonable to attribute the positive DW resistance of our 11 kΩ contact to this effect and the negative DW resistance of the 22 kΩ contact to the AMR of the central atom in a 1-D geometry.

Regarding the resonance properties, one can speculate that because the internal field varies significantly at an atomic scale, a resonance condition can be fulfilled somewhere in the contact for the studied frequencies. Therefore, the rf excitation induces a precession on the resistively active atoms. The exact description of this precession at the atomic scale is difficult because of the complexity of the magnetic configuration and the cooperative character of resonance. Indeed, the DW is intimately coupled to neighboring spins and larger magnetic electrodes. Hence, further ab-initio simulations with magnetization dynamics are required to fully understand our measurements in the atomic scale. Moreover, measurements at higher frequencies should be performed as the rectified signals do not reach their maximum below 22 GHz.

Concerning the resonance properties of 'saturated' atomic contacts, we have not been able to evidence any form of FMR of our atomic contacts. Our only, perhaps relevant, information is that some specific rf frequencies help to destroy some atomic contacts, even at low power. Further measurements at higher frequencies should be performed. It is possible that the expected very large local atomic anisotropy pushes the relevant resonance frequencies very high. Clearly, supplementary experimental (and theoretical) work is needed here.

Chapter 6

Spin currents and resonance

This chapter presents a study of spin currents and especially their interaction with the ferromagnetic resonance properties. First a state of art on Hall effects, spin Hall effect(SHE), inverse spin-Hall effect(ISHE) and how to generate a spin current is presented. Even if spin-orbit scattering gives birth to the spin-Hall effects, the spin-orbit interaction is not studied in this manuscript and its effects will just be postulated. In a second part, our measurements will be presented leading to the detection of inverse spin-Hall effects in a nanostructure and a signature of the influence of spin currents on the ferromagnetic resonance. All these effects have already been reported in the literature, albeit in large samples of several microns or even millimeters in length. We demonstrate here that spin current detection can also be achieved in nanostructures.

6.1 Spin Hall effect and spin currents

6.1.1 Classical Hall effect

The principle of the Hall effect, discovered in 1879 by Edwin Hall, is the deviation of the charge carriers trajectories under an applied magnetic field $\vec{B}$ in a nonmagnetic conductor. This deviation is due to the Lorentz force $\vec{F}_m$.

$$\vec{F}_m = q\vec{v} \wedge \vec{B} \tag{6.1}$$

Where q is the charge of the carrier and v its velocity. In the following, the charge carriers are assumed to be electrons in metals (even if it does work with semiconductors) and $\vec{B}$ is perpendicular to $\vec{v}$. The deviated electrons create a charge imbalance on the border of the metal that induces an electrical field $\vec{E}_{Hall}$ transverse to the current and opposite to the Lorentz one. When the charge imbalance is stabilized, that is:

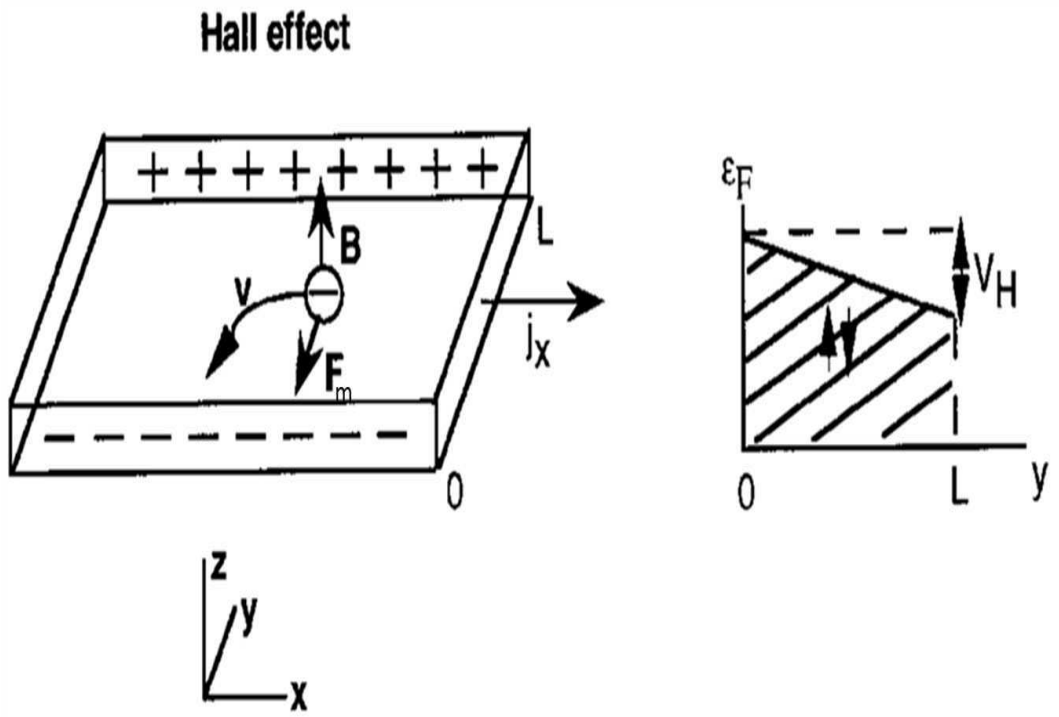

Figure 6.1: Principle of the Hall effect

$$E_{Hall} = vB \tag{6.2}$$

Thus we can measure a voltage V_H transverse to the main current see figure 6.1

$$V_{Hall} = vBL \tag{6.3}$$

with L the width of the conductor. The characteristic of this effect is quantified by the Hall constant R_{Hall} defined by:

$$R_{Hall} = \frac{E_{Hall}}{j_x B} = \frac{1}{\mathrm{n}q} \tag{6.4}$$

with n the carrier density. One can note than when n is small, the Hall constant and so the Hall effect is important for a given density of current and magnetic field. In ferromagnets there are two Hall constants one associated to the external applied field $\vec{B}$ and one for the magnetization $\vec{M}$ of the ferromagnet. The one linked to the magnetization is called the anomalous Hall effect and is due to spin-orbit scattering in ferromagnet.

The Hall effect is used commonly in Hall effect probes to measure magnetic fields $\vec{B}$. For example in our experimental set up, one Hall effect probe measures the magnetic field generated by the electromagnet. The other interest of this effect is in the measurement of the charge carrier density.

6.1.2 Spin-Hall effect

Quantum physics tells us that electrons have their own quantified magnetic moment of value μ_B. That is why Dyakonov and Perel [8] have suggested in 1971 that even in zero applied external magnetic field B a kind of Hall effect call spin-Hall effect still exists. In spin-Hall effect, a charge current in a normal metal is converted to a spin imbalance on the borders transverse to the charge current and with the same symmetry as the Oersted field created by the current (see 6.1). This stems from the spin-orbit interaction that scatters electrons in preferential directions depending on their spin, as for the anomalous Hall effect (see also [9]).

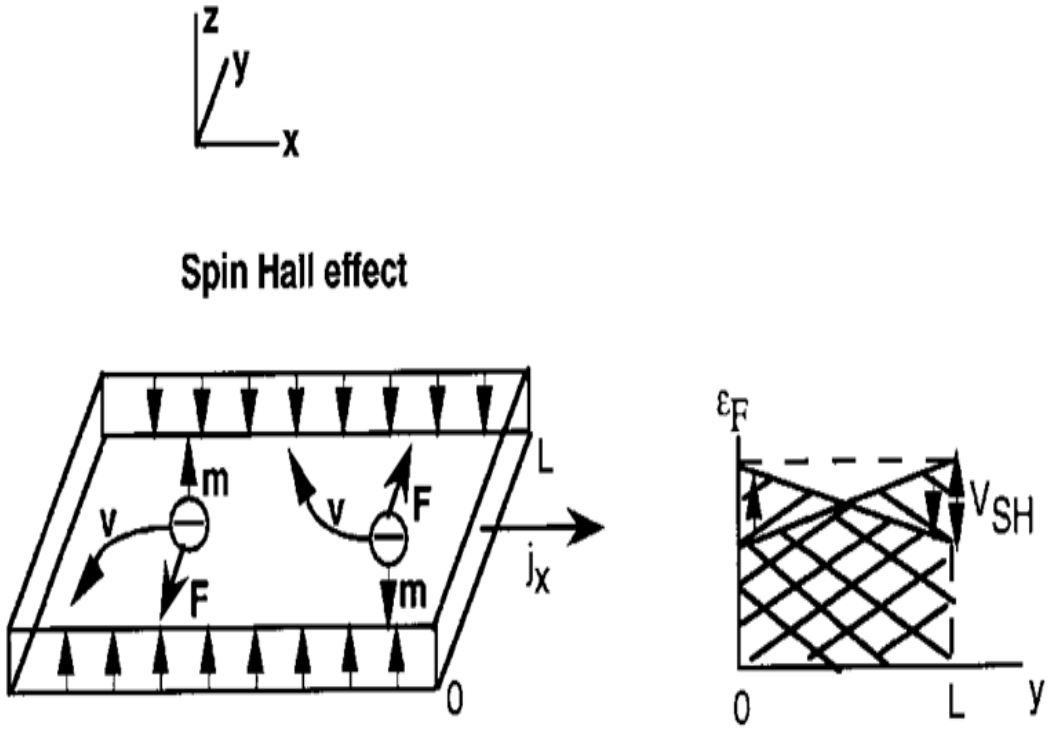

Figure 6.2: Principle of the spin-Hall effect

This spin imbalance can be seen as the creation of two real charge currents opposite in sign and of same absolute value, one for the spin up one for the spin down. As in normal metals charge currents are not spin polarized, this interaction

induces a spin distribution on all the edges with the same symmetry as the Oersted field. Like for the classical Hall effect, it is possible to characterize the efficiency of this charge-spin contribution by a single material specific parameter: the spin Hall angle γ_H, which is defined as the ratio of the spin Hall and charge conductivities. The highest value in metals has been reported for Pt [59, 11] but other values have also been proposed [60, 11] from similar experiments. As two mechanisms, extrinsic [8, 61] and intrinsic SHE [62, 63] are proposed to explain the experimental results, their exact origin is still an open question. In any case, it is not very easy to measure electrically this *spin-voltage* because to do so one should use two electrodes, one is ferromagnetic to scan the spin up or down electrochemical potential and the other one in normal metal as reference (see [64, 65] or [66] for example).

6.1.3 Inverse spin-Hall effect

Reversing the line of thought of 6.1.2 a pure spin current j of polarization $\vec{s}$ can create a measurable real transverse charge current and so a measurable transverse voltage, see figure 6.3. This is called the inverse spin-Hall effect. A pure spin current is constituted of electrons with spin up $+\vec{\mu}_B$(along z) going towards y and electrons with spin down $+\vec{\mu}_B$(along-z) going towards -y in equal quantity, to cancel charge current. Both kinds of electrons have their trajectories bent in the same direction by spin-orbit scattering as this depends on the vectorial product $\vec{v} \wedge \vec{s}$ in the form:

$$\vec{j}_c^{ISH} = \gamma_H (2e/\hbar) \vec{j}_s \wedge \vec{s} \tag{6.5}$$

with $\mathbf{j}_c^{ISH}$ the transverse ISHE charge current and $\mathbf{s}$ the polarization vector of the spin current $\mathbf{j}_{spin}$. However, as spins relax with a typical length scale λ_s, the spin diffusion length, the charge buildup will not increase further when L greatly exceeds λ_s.

6.1.4 Generation of spin current

Spin currents are of great interest because they are non dissipative. They are presently widely studied as they can be used to reverse magnetization [67], excite magnetization dynamics or generate charges in the so called spin battery. But before manipulating them, one should generate them. Beside spin Hall effect, two other ways of producing a measurable, controlled spin current are non-local injection from a ferromagnet and spin pumping at the ferromagnetic resonance (FMR).

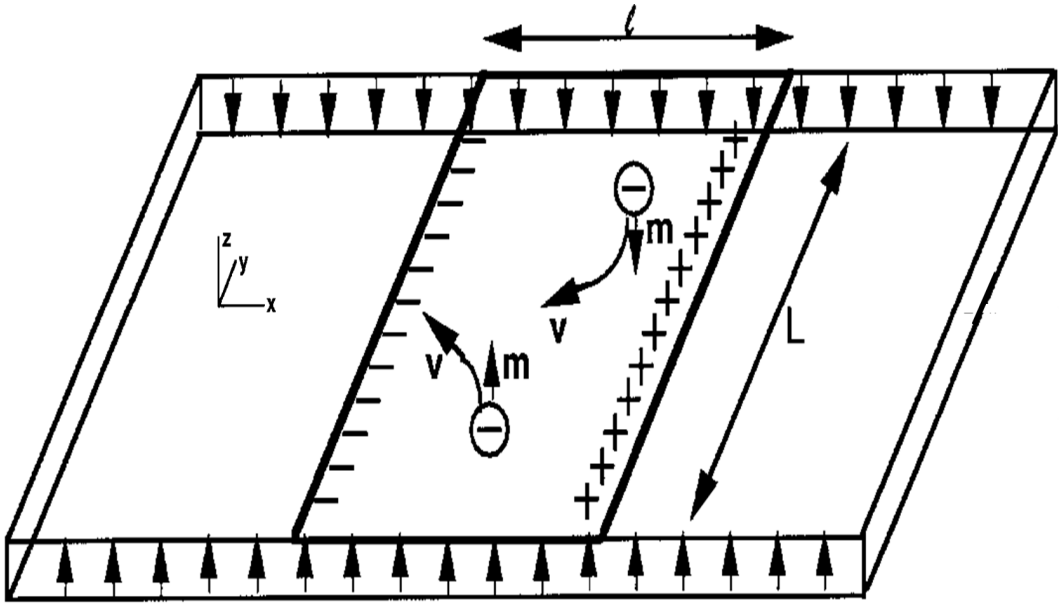

Figure 6.3: Principle of the inverse spin-Hall effect

6.1.4.1 Nonlocal injection

One of the first clear observation of SHE in metallic structures has been realized with a nonlocal spin injection technique see [66]. A good description on the use of nonlocal spin injection to study SHE or ISHE can be found in the article of Otani et al [64]. The nonlocal injection and measurement are using the fact that even if there is no current in a region of a material, the continuity of the electrochemical potential allows a pure spin current to flow [68](see figure 6.4). Indeed the chemical potentials in the normal metal are not the same for spin up and down bands as there is spin accumulation at the interface with the ferromagnet due to the injection of spin polarized carriers.

The intensity of this spin current I_s depends on the intensity of the dc charge current I_{dc} which induces spin accumulation at the interface. This spin current in the nonmagnetic metal propagates over the spin diffusion length. The measurement of SHE or ISHE can be done on very small contacts between two layers as in [64] where the change in spin polarization can be measured. However, this detection technique requires large spin currents and therefore a high charge current density.

6.1.4.2 Spin pumping

Spin currents can be produced dynamically because of the intrinsic damping during ferromagnetic resonance. Indeed, damping processes absorb some angular momentum which can result in the emission of a spin current in a normal metal

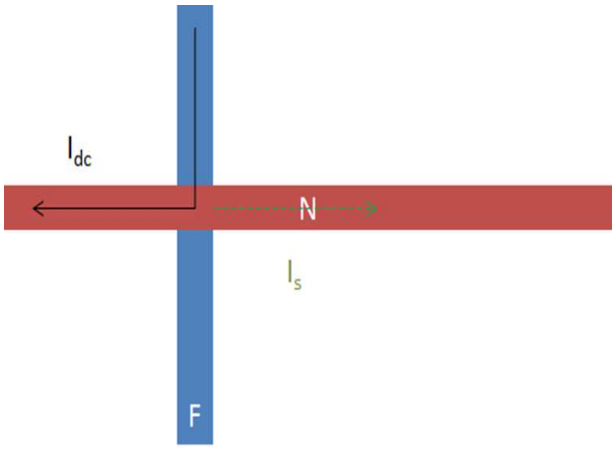

Figure 6.4: Principle of the nonlocal injection of a spin current. F is a ferromagnetic metal and N a nonmagnetic one.

in contact. Considering a F/N junction at equilibrium in which the magnetization is changed suddenly, the bands instantaneously change in energy. In order to go back to the equilibrium situation there has to be spin transfer from one band to an another. If F is in contact with N, this spin transfer can go via N. A way to change periodically the magnetization of F is to put it in resonance, where precession of the magnetization is resonantly excited by a small applied rf magnetic field. Tserkovnyak et al [69, 70] analyzed the case of circular precession of the magnetization and demonstrated that the evolution of the damping due to the interface can generate a spin current in the normal metal. This spin current emitted in N has two components an ac one of course and a dc one, see figure 6.5.

The spin current induced by spin pumping is determined at the interface by [69, 70]:

$$j_s^0 \vec{s} = \frac{\hbar}{4\pi} g^{\uparrow\downarrow} \vec{m} \wedge \frac{d\vec{m}}{dt} \tag{6.6}$$

with $\vec{m}$ the magnetization direction, $g^{\uparrow\downarrow}$ the real part of the effective spin-mixing conductance and $\vec{s}$ the unit vector of the spin current polarization. $\vec{s}$ is perpendicular to $\vec{m}$ and to $\frac{d\vec{m}}{dt}$. If the spin diffusion length λ_s is larger than the thickness t_N of the N layer then one can have reflection back on the boundary and so diffuse back into the F layer. The spin-diffusion equation describes the propagation of the spin accumulation $\vec{\mu}_{\mathrm{N}}$ in the N layer (due to the difference of local electrochemical potential of up and down spins):

$$i\omega \vec{\mu}_{\mathrm{N}} = D \frac{\partial^2 \vec{\mu}_{\mathrm{N}}}{\partial z^2} - \frac{1}{\tau_{sf}} \vec{\mu}_{\mathrm{N}} \tag{6.7}$$

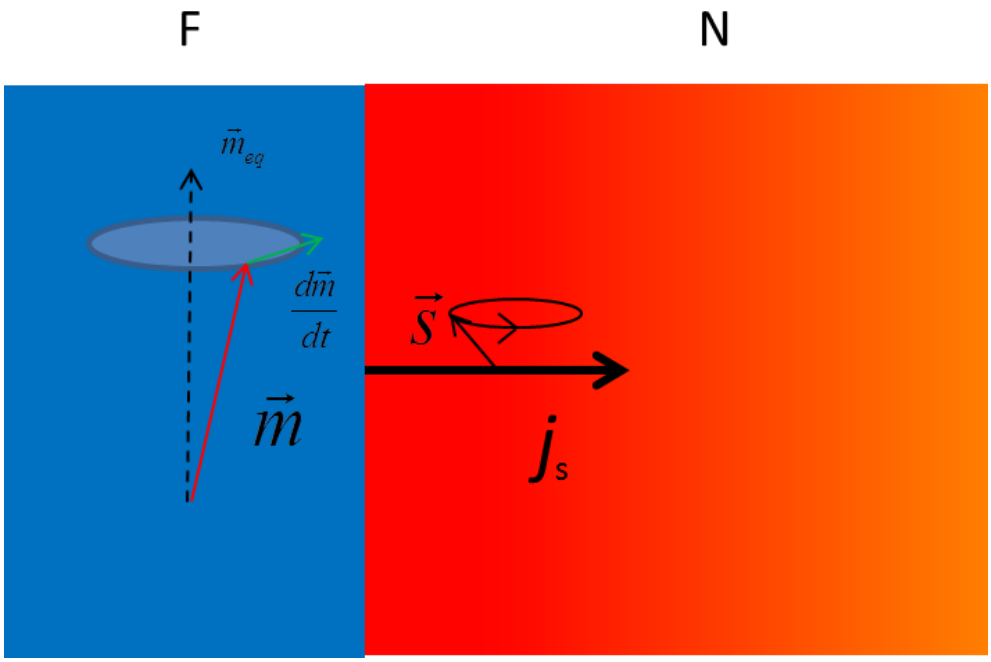

Figure 6.5: Schematic model of spin pumping in a F/N bilayer

where ω is the angular frequency, τ_{sf} is the spin-flip time and $D = V_F^2 \tau_{el}/3$ is the electron diffusion constant, with τ_{el} the electron relaxation time. The boundary condition at the N/F interface is given by

$$j_s^0 \vec{s}(z=0) = -D \left. \frac{\partial \vec{\mu}_{\mathrm{N}}}{\partial z} \right|_{z=0} \tag{6.8}$$

At the free interface we use the full spin current reflection condition

$$\left. \frac{\partial \vec{\mu}_{\mathrm{N}}}{\partial z} \right|_{z=t_N} = 0 \tag{6.9}$$

These equations 6.7,6.8 and 6.9 can be solved analytically to yield the decay of the spin accumulation as a function to the distance from the F/N interface. The dc contribution to the spin current can be written:

$$j_s(z) = j_s^0 \frac{\sinh[(t_N - z)/\lambda_s]}{\sinh(\frac{t_N}{\lambda_s})} \tag{6.10}$$

where $\lambda_s = \sqrt{D * \tau_{sf}}$ is the spin diffusion length. This spin pumping effect can also be used to measure electrically the magnetization resonance see [71, 40] without using SHE-ISHE or with ISHE see [10, 72, 73, 74, 11, 29] for example. The use of

dynamical spin pumping to generate a spin current measured by ISHE has therefore already been reported, but only in very long wires of several hundreds of microns.

6.2 Principle of measurements using spin currents

In this part, the principle of the spin current measurements using ISHE during ferromagnetic resonance is explained. First the sample geometry will be described and then the expected behavior.

6.2.1 Description of the sample

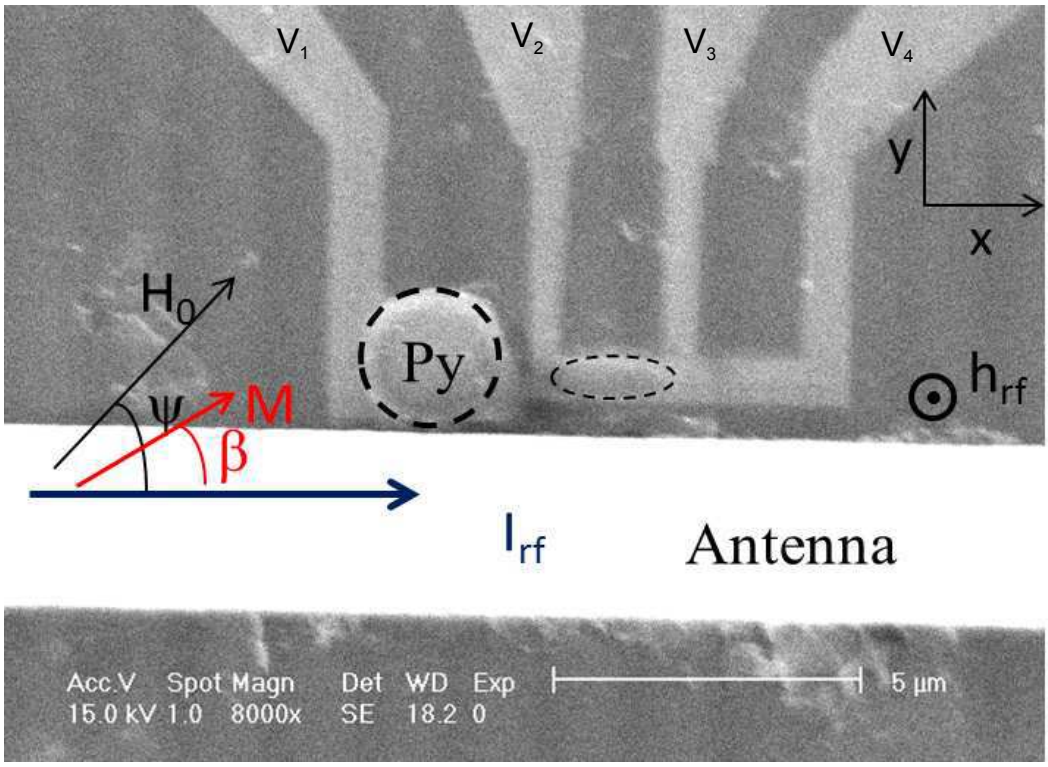

Figure 6.6: SEM image of a device for ISHE measurements of the FMR.

The samples for the study of ISHE are like the one in figure 6.6. We have two bilayer structures, one is a 2 μm diameter circle and the other one an ellipse of 2 μm by 600 nm separated by 800 nm of normal metal. The bilayer is constituted of 15 nm thick of normal metal (Au or Pt) and 20 nm thick Py. One sample was made with the normal metal in gold and the other one with platinum (called gold sample and platinum sample in the following). The fabrication process is explained in part 2.2. The border of the circle is at 200 nm of the shorted end of the rf antenna. The part between V_4 and V_3 is only in nonmagnetic metal and it was used a a reference to verify that there is no magnetic field dependence of the signal without the presence of a ferromagnetic structure. The aim of these samples is to

measure the spin current emission at the resonant state and its effect considering the proximity of the two structures. The 15 nm thickness has been chosen to be the same for Pt and Au. It is an appropriate thickness for Pt to avoid reflection of the spin current at the free interface and to maximize the voltage measured by ISHE. The spin diffusion length λ_s in Pt at 77 K is about 7 nm, whereas it is 35 nm for Au, so the spin current will be reduced due to interface reflection (see part 6.1.4.2). The dc spin current is mainly perpendicular to the layers plane and the ISHE voltage is measured in plane along the charge current path.

The main measurements are carried out at a frequency of 13300 Hz used to modulate the RF field. The rf applied power was 15 dBm which means that nearly 9 dBm reach our shorted end of the antenna. We use such a high rf power to boost the emitted spin currents and hence increase the ISHE signal. A superimposed current at 17 Hz is applied between V_1 and V_4 to measure the static resistance and checking the global state of the sample. For the circle ($V_c = V_1 - V_2$) as for the ellipse ($V_e = V_2 - V_3$) we measured both the resistance (17 Hz) and the voltage at the frequency of rf modulation. This involves it means 4 lock-in amplifiers in total. All of them had their time constant at 300 ms. For the Au sample reported here, the antenna needed to be repaired with silver paint after fabrication, far from the sample. As a result, it seemed to be affected above 20 GHz, which limited our measurements to below this frequency. This is not a real problem as this frequency range is perfectly adequate to induce FMR. The measurement procedure consists in sweeping the applied magnetic field at a given rf frequency. In part 6.4, a dc current is also passed through the sample between V_1 and V_4.

6.2.2 Expected behavior

FMR induced voltages have two origins: one AMR contribution (due to a resistance change) and one ISHE contribution (a pure voltage). The former results from the induction currents at the rf frequency rectified by the resistance change at the same frequency, and the latter is purely a Hall voltage. Both contributions are proportional to the rf power and exist without any polarization of the sample. Indeed the dc component of the spin pumping induced spin current is proportional to the loss of magnetization along the equilibrium position during precession, so to θ^2 where θ is the average cone angle of precession. So varying the rf power can not allow us to separate the two signals (we are in the small angle precession in our measurements). We call the AMR effect the 'rectified signal' and it is in general more important than the ISHE (see next part), which in any case contributes to the measurement. The AMR contribution has an odd (equation 3.8) and an even (equation 3.7) parts as regard to the applied static magnetic field. As equations 6.6 and 6.5 demonstrate, the ISHE current is odd with the magnetization direction. From reference [11] We have the expression of the ISHE voltage :

$$V_{ISHE} = \frac{1}{2}\frac{\gamma_H e L \omega_f \lambda_s g^{\uparrow\downarrow} \sin(\beta)\sin^2(\theta)}{2\pi(\sigma_N t_N + \sigma_{Py} t_{Py})} \tanh(\frac{t_N}{2\lambda_s}) \tag{6.11}$$

where $\frac{1}{2}$ is for the essentially planar precession, L is the length of the bilayer, $\sigma_N t_N + \sigma_{Py} t_{Py}$is the conductance of the bilayer structure (which is measured). The signal measured is $V_{meas} = V_{AMR} + V_{ISHE}$. Due to their different behaviors with the magnetization orientation, we can separate the ISHE contribution from the AMR one. The AMR contribution is zero when β=90° while the ISHE contribution is maximal and odd with saturating field.

It is useful to remember here that, because our dc contacts are not adapted for rf currents, the shapes of the AMR peaks are frequency dependent through the phase between induction currents and magnetization precession. It is completely different for the dc part of the ISHE contribution, which is a pure voltage generating Lorentzian-like peaks for all frequencies and modes. The sign of the ISHE peak on the circle and on the ellipse signals should also be the same.

There should be two main differences between the circle and the ellipse. First for the circle, the resonance field at a given rf frequency is independent of the magnetization direction, i.e. of the in-plane saturating field angle ψ. This is not the case for the ellipse in which the demagnetization field changes with the direction of magnetization, hence the angle β_{ellipse} between $\vec{M}$ and the current lines, as shown in chapter 4.

Because of the geometry of the structure, the current lines bend at the level of the circular nanostructure making an average angle of 30° compared to that of the ellipse. As the circle is highly symmetric, we obtain $\beta_{\text{circle}} = \psi - 30°$ for a field over 30 mT. So the zero signal, due to these geometric reasons, is not the same in the two structures and neither is the symmetry with the direction of $\vec{H}_0$. Especially when the $\vec{H}_0$ is transverse (perpendicular to the antenna but in the plane), the FMR signal of the circle is not negligible and its ISHE contribution is not maximal. The odd contribution of the AMR circle signal, assuming that it is due to a transverses rf magnetic field generated by the antenna, varies as:

$$V_{odd} \propto \cos(\psi)\sin(2 * \beta_{\text{circle}}) \tag{6.12}$$

The rf induced currents passing through the normal layer are also generating an average planar rf magnetic field, transverse to the current. In the circle, its contribution to rectified signal reads:

$$V_{odd} \propto \cos(\beta_{\text{circle}})\sin(2 * \beta_{\text{circle}}) \tag{6.13}$$

The fundamental difference between Au and Pt samples is the higher spin orbit coupling of Pt that will enhance the ISHE contribution. We can also use the strong spin-Hall effect of Pt to inject spins into the ferromagnet. For this, a high

dc current is passed through the structure, flowing mainly through the platinum. A spin current is hence generated perpendicular to the nanostructure by spin Hall effect, which given its polarization either enhances or decreases the resonance (see [75] for example). The spin current from Pt acts as an additional damping term (positive or negative). In the gold sample the effects of a high dc current on the damping is expected to be much less significant and perhaps even not measurable.

6.3 Inverse spin hall effect in nanostructures

In this part we will present our measurements of the ISHE signal on both Pt and Au samples.

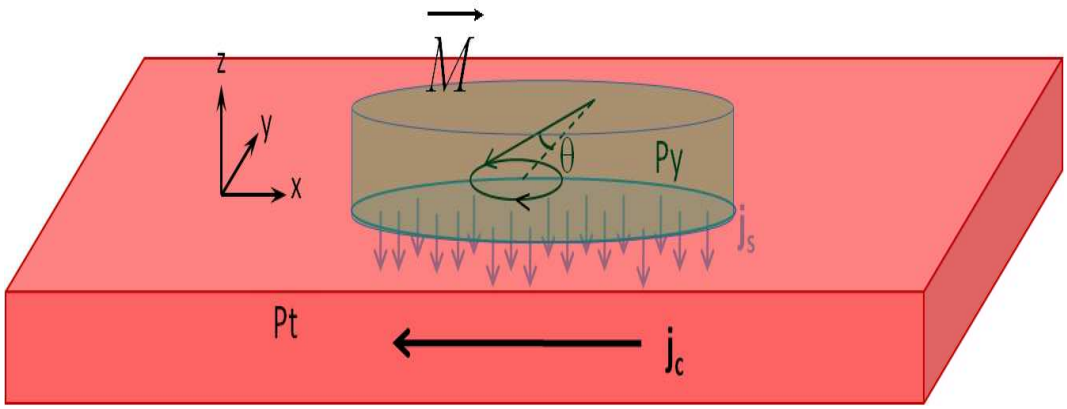

Figure 6.7: Schematics of the generation of a charge current in Pt at the resonance by ISHE using spin pumping in our bilayer nanostructures

6.3.1 The platinum sample

First let us study the rectified voltage with a static magnetic field neither longitudinal nor transverse.

The general amplitude of the rectified signal in figure 6.8 is consistent with the measured AMR resistance of 0.06 Ω, and an angle of precession of 5° (measured at 18 GHz with a dc current) induced by the high power of 15 dBm delivered by rf source. The induced current at resonance is slightly smaller than that generated by the full ferromagnetic nanostructure of chapter 4 for the same rf power. Indeed in the bilayer nanostructure, part of the induced current has to flow in the normal metal below the ferromagnet. The signal is still in the linear regime in spite of the high angle of precession if the static magnetic field is large enough.

The importance of the odd contribution at 60° is higher than in chapter 4 because the Oersted field of the rf induced current is larger. Indeed an important part of this current flows in the normal layer thus inducing at the level of the magnetic nanostructure, a transverse rf magnetic field. Measurements on the pure platinum part of the sample gives a noisy curve independent on the applied field, as expected since no impedance varies at the rf frequency in this branch. The amplitude, in a transverse magnetic field, expected for the ISHE contribution would be at best 40 nV using equation 6.11 the value of Mosendz [11] for spin diffusion length angle of Hall and spin mixing conductance but our measured value for the conductance.

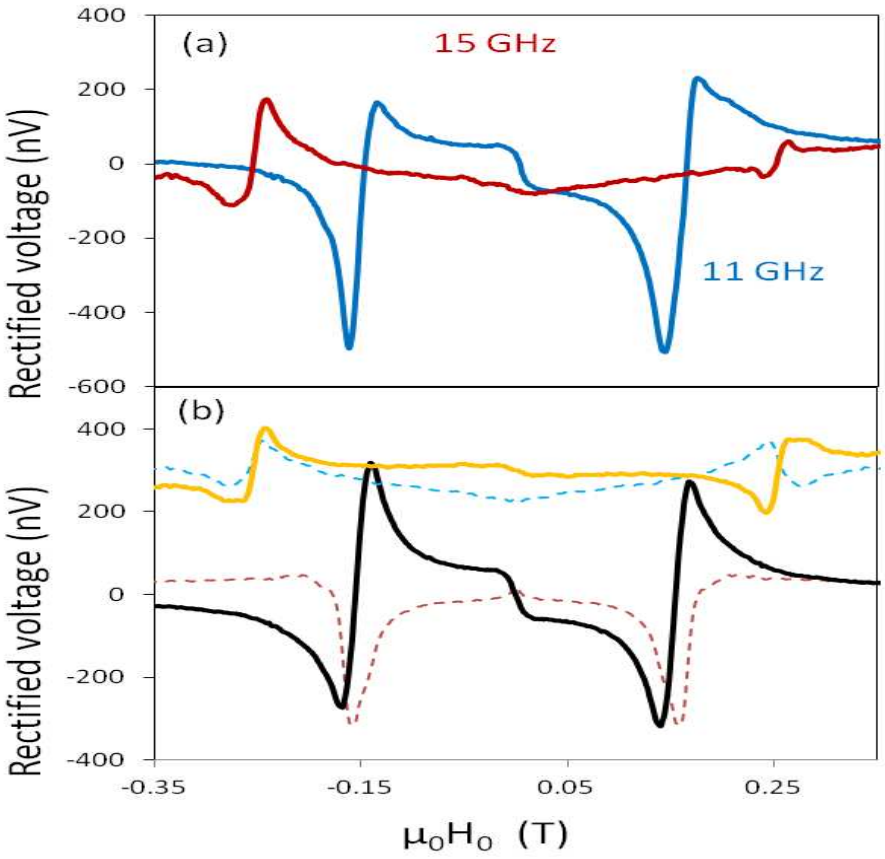

Figure 6.8: (a) Full loop of the rectified signal from the ellipse (b) Separation in odd (solid line) and even (dashed line) contributions. As for the ferromagnetic nanostructures of chapter 4, peak shapes depend on frequency. The applied field angle is 60°.

It should also have a Lorentzian shape. As for the full ferromagnetic structures, the shape of the uniform mode (when not influenced by other modes) is independent on the angle of the static magnetic field. In this measurement, we can not separate with a relevant argument the ISHE contribution from the AMR contribution.

In figure 6.9, the static magnetic field was applied transverse to the main axis of the ellipse so that the ISHE voltage is maximum and the AMR one is the lowest possible, especially in its odd contribution. Hence, the odd part of the rectified signal of the ellipse is attributed to the ISHE contribution. Its ISHE nature is also confirmed by the fact that for all frequencies, a response close to a Lorentzian shape is measured at the uniform resonance field. The value of this ISHE signal reaches

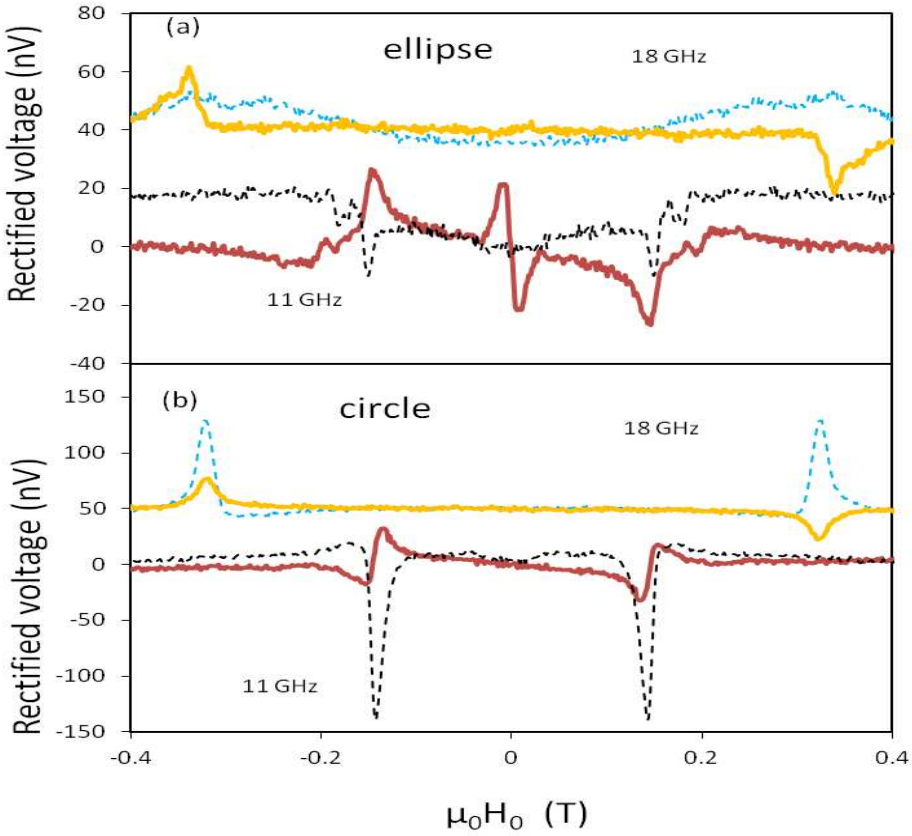

Figure 6.9: (a) ellipse and (b) circle rectified voltages on Pt/Py for a static magnetic field transverse to the main axis of the ellipse. The solid line is the odd contribution and the dashed line the even one.

20 nV in consistence with the expected value of about 40 nV. This is of a similar amplitude to the residual even AMR contribution. The amplitude of 20 nV might be explained by a smaller spin diffusion length of 3 nm instead of 10 nm [75], but we did not measure it. Thus there is no specific change of the *spin Hall* parameters to be expected in nanostructures compared to bulk values.

On the circular nanostructure, the odd part of the signal is not completely Lorentzian. This could be surprising at first sight, but this can be expected as due to the average 60° angle instead of 90°between current lines and magnetization which induces a significant planar Oersted field as well as an AMR variation of resistance at ω_{rf}. However the odd signal on the circle is mainly a negative peak for positive fields at all frequencies, like that measured for the ellipse, thus confirming the influence of the ISHE on the signal. This underlines the importance of the geometry for

a correct detection of the ISHE.

To be completely sure that this is not an artifact, we have carried out a similar study on the same structure in which Pt is replaced by Au. Therefore, this new structure has seen its active part removed as the spin orbit effect in Au is much weaker than that in Pt. This is discussed in the next part.

6.3.2 The gold sample

The full AMR measured in ohms was higher in the Au sample than the Pt sample, so we scaled the amplitude in the plotted rectified signal. However even after corrections, the dynamic AMR contribution is higher than that for the platinum sample, which might be due to a more efficient generation of rf field by the antenna.

The ISHE in the gold sample represented in figure 6.10 is significantly less important (and noisier) than that in the platinum comparatively to the residual even AMR contribution. For the difference in shape between circle and ellipse with regards to the ISHE signal, we still have the same behavior as with platinum, confirming that it depends on the geometry and the frequency. Indeed in Au the spin-orbit coupling is lower than that in Pt, thus the conversion of the spin current in charge current is less efficient. The odd ISHE contribution is about 6 times lower than the AMR induced even one. It is the value expected considering the differences in their spin Hall angles, $\gamma_{Hall}(Pt) = 0.013$ and $\gamma_{Hall}(Au) = 0.0035$ (from reference [11]), and the difference in conductivities of the materials.

6.3.3 Conclusion on ISHE

Using measurements on both Pt/Py and Au/Py bilayers, we have demonstrated that the ISHE contribution in nanostructured bilayer can be extracted. At this small scale, the signal is always mixed with other contributions generated by rectification effects of induced RF currents. The odd parity of the ISHE with the direction of magnetization is used to extract the relevant signal, whose magnitude is consistent with reported Hall angle values [59, 11, 65]. We note here that our results are not consistent with the spin Hall angle values given by some other groups [76, 60, 75]. This difference might depend on the quality of the material and the sensitivity to extract ISHE from other contributions.

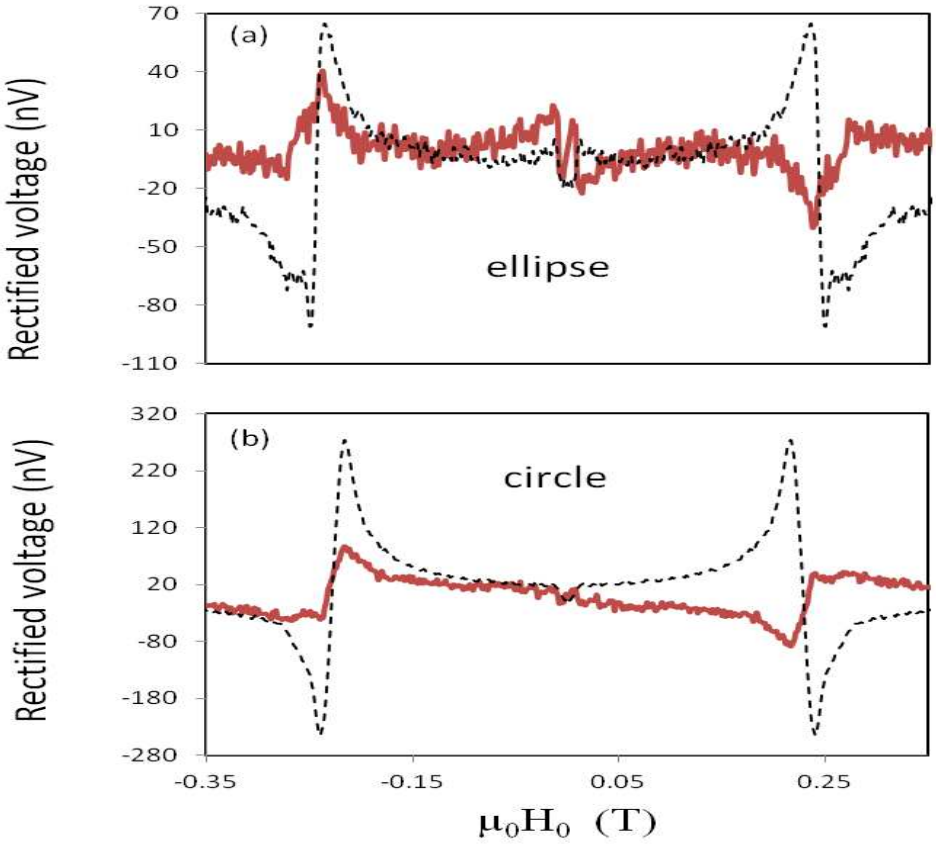

Figure 6.10: (a) ellipse and (b) circle measured voltages on Au/Py corrected from the AMR value, for a magnetic field transverse to the main axis of the ellipse. The odd contribution is the solid line and the even one the dashed line. The rf frequency is 15 GHz.

6.4 Spin injection influence on damping

This section deals with our attempts to change the Gilbert damping in our Pt/Py bilayer using spin injection into Py. The spin current is generated in the Pt by spin Hall effect (the enhancement of damping due to the proximity of Pt [77] is not discussed). First we deal with the case where the applied magnetic field is purely transverse to the structure, and in a second step the angle is slightly tilted by 10° from the transverse direction. To influence the damping, a large dc current is passed through the structure. In the Pt layer this dc current gives birth to a perpendicular spin current with a transverse polarization by spin-Hall effect (see part 6.1.2). This spin current is injected in the Py nanostructures through the interface. This transfer of angular momentum can be seen as an additional term to the damping. Interestingly, depending on the spin direction (parallel or anti-parallel to the magnetization), the extra term can be negative or positive. The influence of this damping variation should be a small modification of the resonance peaks' amplitude and width (see references [76, 75, 77] where it has been observed on large samples). Recently it has also been measured by Brillouin light scattering (BLS) in samples with similar dimensions to ours by Demidov et al. [12]. All the

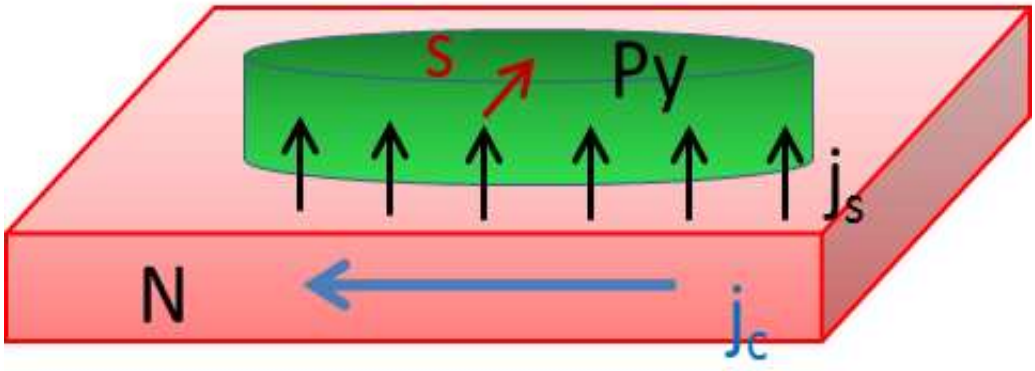

Figure 6.11: Principle of the spin-Hall current injected into the Py through the Pt/Py interface.

measurements of this part, are performed on the ellipse nanostructure.

6.4.1 Transverse field

This change of damping depends on the relative directions of polarization and magnetization. The polarization of the spin current can be reversed by changing the sign of the dc current.

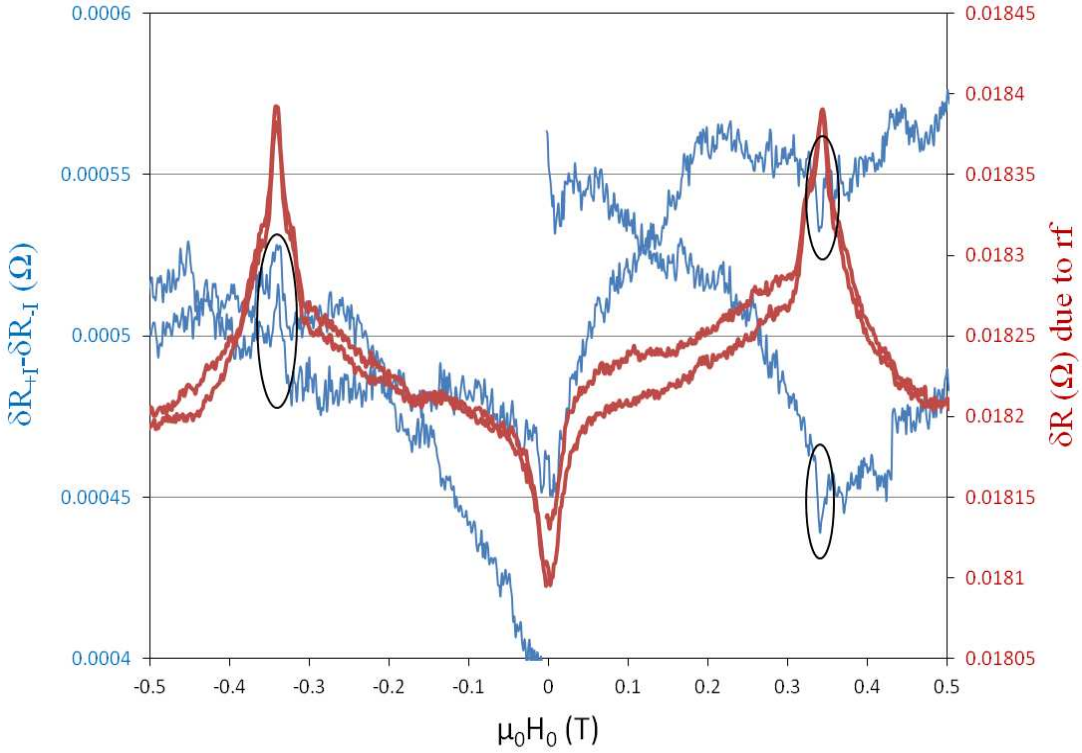

Figure 6.12: rf induced variations of the resistance (in ohms) in red, and difference between positive and negative currents in blue. The rf frequency was 18 GHz and the current density inside Pt is estimated to be $6.35 * 10^6 A/cm^2$.

First we have checked the influence of the current induced Oersted field on the peak position and found it negligible for an applied transverse field. At 18 GHz, the resonant field is 341 mT and the average Oersted field (at maximum dc current) is estimated to be 0.3 mT (about 2/3 of the current goes in Pt from the AMR measurements). Thus, we have seen no difference in the peak position between a positive and a negative current. As the peak variations are tiny, measurement are performed under He gas at 77 K to increase the thermal stability. This is found to be important to extract the small signal from the noise. The measurement with a current density of $6.35 * 10^6 A/cm^2$ at 18 GHz are shown in figure 6.12. The most important feature can be seen in the difference between positive and negative currents where there is a positive peak at negative field and negative peak at positive field. This is expected as the sign of the electrical current determines the polarization of the injected spin current. The damping can be either increased when it is parallel or decreased when antiparallel to the magnetization direction, which is controlled by the magnetic field. The dc peaks are mainly due to the change in the dc signal and the rectified signal (both AMR and ISHE contributions measured

at zero current) was subtracted in order to obtain the effect on damping. When modifying the damping, the rectified signal is also influenced. These changes in the rectified voltage increase with the current and should not be neglected even at high dc current density. The maximum change (assuming no influence from the rectified signal) in the resistance difference between positive and negative current represents 10 percent of the rf induced change of resistance at resonance. Therefore, at the high current density the induced rf resistance change is impacted by 5%. hence, the angle of precession is changed by less than 2.5% or 0.12°, the damping α is also modified by 2.5%. At half the current density the signal due to the change of damping is dominated by the noise.

We have also checked on the gold sample that no change of the damping can be observed for the same current density. This is again consistent with the lower spin orbit coupling of Au than Pt. It also allows us to exclude the temperature as a parameter to explain this slight difference between opposite currents.

6.4.2 Field close to the transverse direction

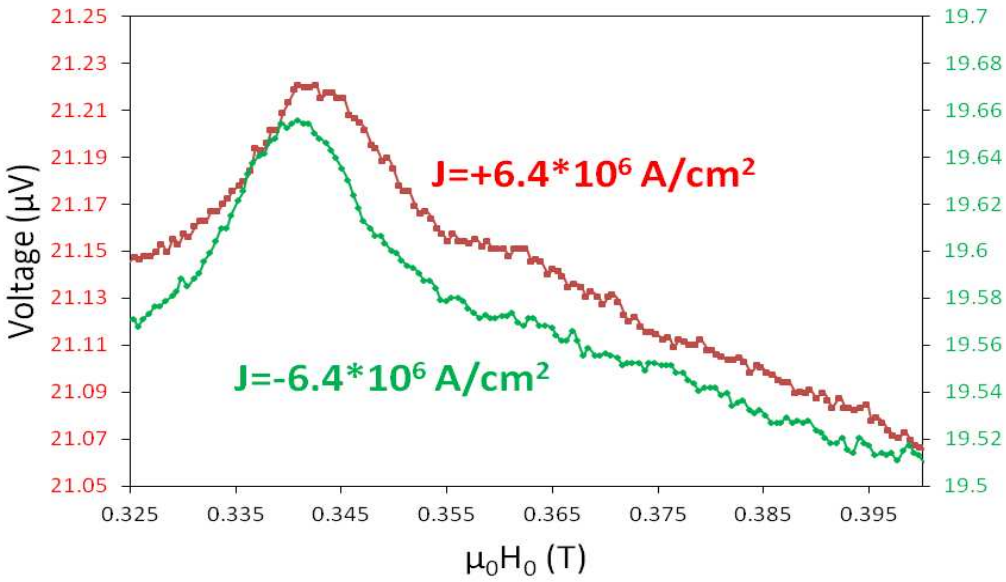

Figure 6.13: Voltage measured for two opposite dc currents on the Pt sample.

We also measured in some details the same effect at an applied field angle of 80°, where the signal should be lower as the magnetization is no more exactly transverse to the current lines. At 18 GHz and positive magnetic field the influence the rectified voltage is almost unaffected. This time the Oersted field has an influence on the position of the peak, see figure 6.13, as it influences also the effective

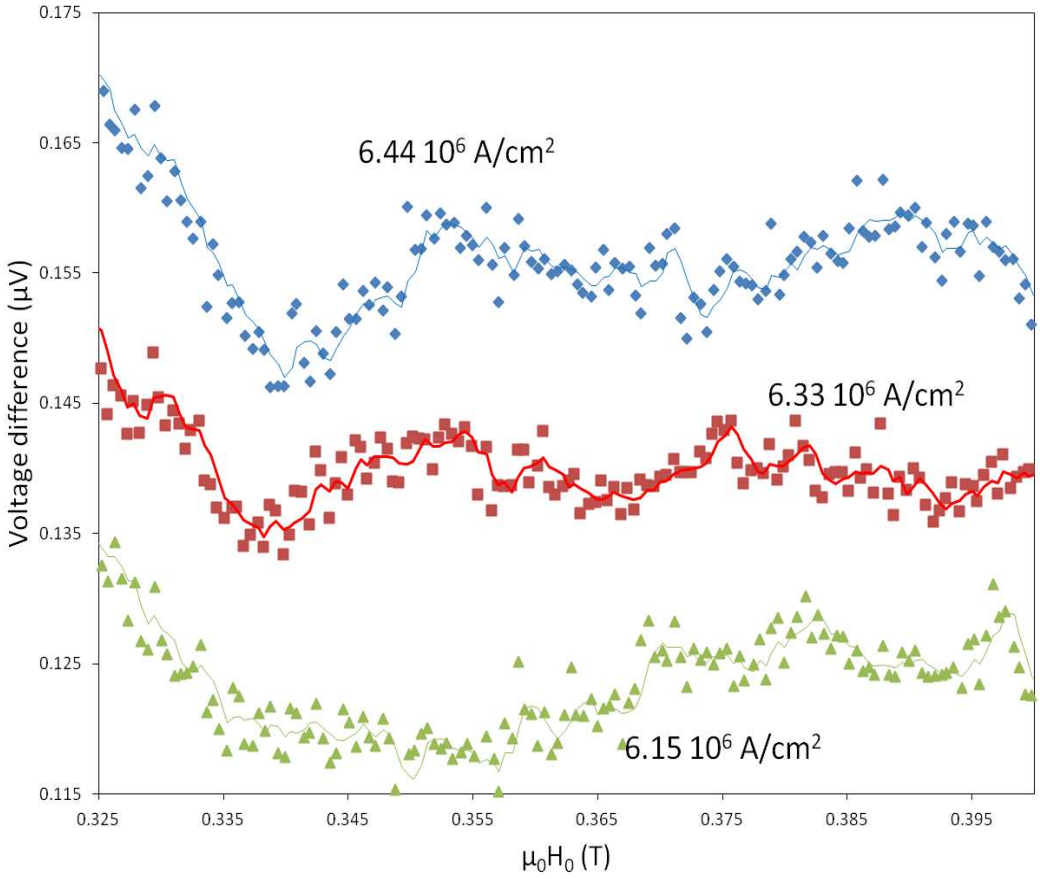

Figure 6.14: Differences between positive and negative currents as a function of field. The dots are an average of 4 measurements, and the solid lines a smoothing fit.

angle β. In order to produce the difference curves as in the previous part, we had to take into account the Oersted field shift. We then obtained the figure 6.14 were the appearance of a negative peak at the resonant field appears above a given current density. So even when the magnetic field is not exactly transverse a signal can be measured evidencing the change of Gilbert damping of our ellipse nanostructure. However the signal is noisier than in the pure transverse geometry. Interestingly, we can estimate that in this experiment, we reached a temperature of the order of 500K (the resistance is supposed to be linear in temperature) as compared to 130 K in the previous transverse experiment. In both cases, the signal is not intense enough to attempt a convincing quantitative explanation. However, it seems that the evolution of damping is not proportional to the applied current.

To conclude on the spin current influence on damping, we were able here to

detect a slight modification of the resonance peak amplitude at the ferromagnetic resonance in a nanostructure. This effect, due to the spin current induced by SHE in Pt, requires rather extreme conditions and results in a noisier measurement than that of the FMR detection by ISHE. However, we are still able to measure it in our nanostructures. This effect can be detected even departing from the optimum conditions regarding magnetization direction.

6.5 Coupling of two ferromagnetic nanostructures

The samples were designed with two adjacent ferromagnetic nanostructures in order to investigate a possible magnetic coupling between them. Indeed the distance between the circle and the ellipse, 800 nm, is lower than their size of 2 μm so dipolar coupling should not be negligible.

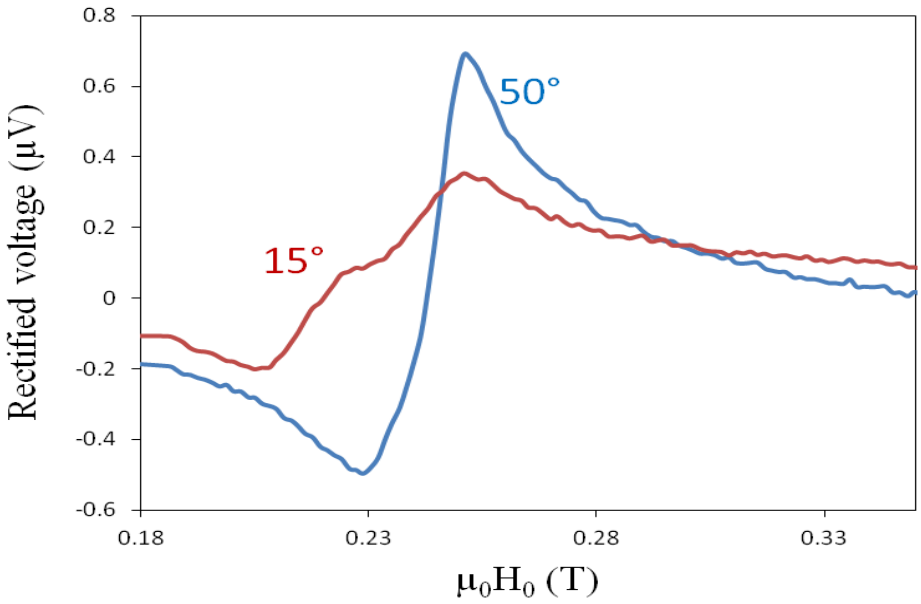

Figure 6.15: The even rectified signal for two angles ψ: -15° (blue) and +50° (red) on the ellipse of the Au/Py sample.

In figure 6.15, the even contribution of the ellipse rectified signal is plotted for two different applied angles at 15 GHz for the gold sample. There is a major difference in the shape, as at -50° we get a Lorentzian derivative shape but at -15° a threshold in the middle of this derivative appears. It is tempting to attribute this to a mode that varies with the angle but this is unfortunately not so simple. At -50° ellipse and circle resonate clearly at different magnetic fields unlike at -15° where they have the same resonant field. So this threshold happens in the middle of the FMR peak where both ellipse and circle are in resonant condition. The influence of spin currents between both structures is not a convincing explanation as the spin diffusion length in gold is estimated near 35 nm. This threshold can be due to two nearby resonances resulting in a dipolar coupling between the two structures thus giving two neighboring resonant fields.

In figure 6.16, we sum up the position of the resonant fields for both ellipse and circle as well as the width of the ellipse peak. The circle resonant field is less

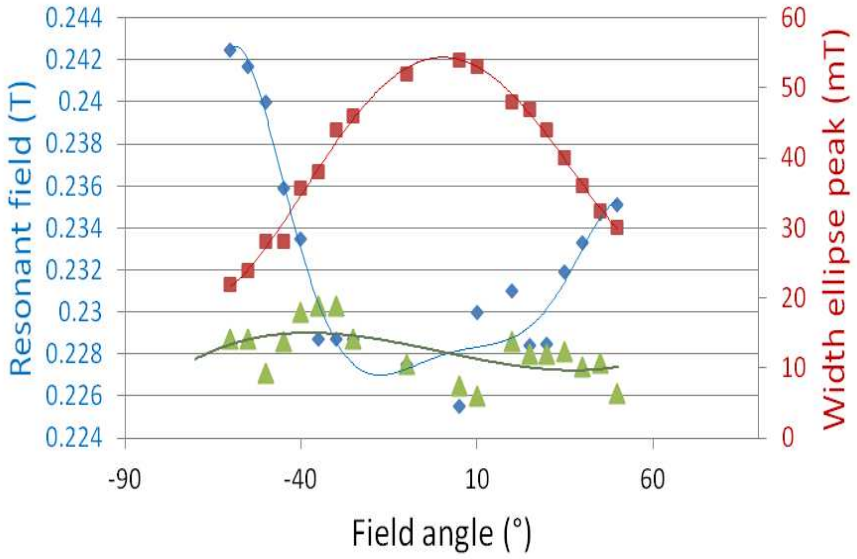

Figure 6.16: Summary of the measurements on the Au/Py sample at 15 GHz and 77 K versus ψ. The resonant field of the ellipse is in blue and the one of the circle in green. For angles near zero the resonant field of the ellipse looks locked near the one of the circle. The angular variation is also not symmetrical on both sides of the zero angle.

impacted because of its larger magnetic volume. However the symmetry with the zero position of the applied angle is not observed, which is quite strange as there should be no reason in different coupling for +/- angles (just the sign of the peak should be reversed for the ellipse). We also designed a similar structure on Pt in which the same type of measurements have been carried out. However, it seems that several modes coexist in the transverse field geometry for the ellipse, which greatly complicates the analysis. This requires therefore further measurements on different samples in order to understand the coupling behavior.

Conclusion and outlook

During this thesis work, we have successfully adapted an rf excitation environment to the mechanical break junction technique. An efficient electrical measurement of the ferromagnetic resonance has been realized in nanostructures where the dynamics of the uniform resonance mode is well known. The best sensitivity to the FMR was reached measuring the rectified signal resulting from a mixing between induction currents and resistance variation at the rf frequency. With this technique we are able to detect magnetic precession in nanostructures with angles as low as 0.05° as well as a sensitivity of a few atoms in an atomic contact geometry. The results obtained during this work concerned dynamical properties of contacts of atomic sizes as well as the interaction of spin currents with the FMR properties of magnetic nanostructures.

In nanostructures of 4 nm in thickness, we have evidenced the large rf susceptibility of transverse domain walls for frequencies above those of domain resonance or domain wall propagation. To achieve this, we have measured the resonance induced average resistance variation using the anisotropic magnetoresistance. The DW rf susceptibility is found to far exceed the one of saturated domains by a factor of 13, as well as being surprisingly independent of the rf frequency. The rf measurement procedure can thus provide information on the domain wall properties which could not be seen in a pure dc resistance measurement.

We have also found that new resonance modes appear when breaking our nanostructures to generate a narrow constriction. These are attributed to the change in the demagnetization factor at the constriction level that reduces the effective magnetic field. Due to the fact that the resonance is a collective response to an rf excitation, the shape and parity of the previous modes are modified. In order to precisely understand the origin of these new modes and the coupling between the dynamical properties of the constriction with the electrodes, simulations are the next essential step. Experimental measurements should also be improved to better determine the number of modes and their position.

One of the main goals of this thesis work was to measure ferromagnetic resonance in atomic contacts. We have not achieved this in the saturated state, maybe because the large expected local anisotropy pushes the resonance frequencies outside our measurement range. However, we managed to measure the resonance of the constrained domain walls in these atomic contacts. We found that their dynamical properties depend on the conductance as well as their exact position in the contact, and vary with frequency. The measured rectified signals correspond to magnetic precession up to 20 times that of saturated domains in the unbroken state. Further ab-initio simulations with magnetism dynamics are required to fully understand these measurements in the atomic scale.

The experimental setup also allowed us to study the emission of spin currents when a ferromagnetic nanostructure is driven to resonance, as well as the reverse effect of damping modulation by spin injection. In Py/Pt nanostructures, we have been able to detect the voltage induced by inverse spin Hall effect in Pt resulting from conversion of spin currents by the strong spin orbit coupling of Pt. Moreover, we have also influenced the ferromagnetic resonance in Py by injection of a spin current produced by spin Hall effect inside the platinum. We have demonstrated here that an electrical detection of these effects can be scaled down to measurements in nanostructures. Lastly, the study of dynamically coupled nanostructures was addressed, but an improvement of materials quality as well as the reduction of some critical length scales are required to evidence the effect of ac spin currents flowing in the normal metal between the magnetic nanostructures.

Bibliography

[1] M. Viret, M. Gabureac, F. Ott, C. Fermon, C. Barreteau, G. Autes, and R. Guirado-Lopez. Giant anisotropic magneto-resistance in ferromagnetic atomic contacts. *The European Physical Journal B - Condensed Matter and Complex Systems*, 51:1–4, 2006. 10.1140/epjb/e2006-00201-3.

[2] G. Autès, C. Barreteau, M. C. Desjonquères, D. Spanjaard, and M. Viret. Giant orbital moments are responsible for the anisotropic magnetoresistance of atomic contacts. *EPL (Europhysics Letters)*, 83(1):17010, 2008.

[3] A. B. Hamida. *Transport électrique et transfert de spin dans des constrictions de tailles nanometriques*. PhD thesis, Université Paris VI, 2010.

[4] A. Ben Hamida, O. Rousseau, S. Petit-Watelot, and M. Viret. Positive domain wall resistance in atomic-sized constrictions. *EPL (Europhysics Letters)*, 94(2):27002, 2011.

[5] Stefan Egle, Cecile Bacca, Hans-Fridtjof Pernau, Magdalena Huefner, Denise Hinzke, Ulrich Nowak, and Elke Scheer. Magnetoresistance of atomic-size contacts realized with mechanically controllable break junctions. *Phys. Rev. B*, 81:134402, Apr 2010.

[6] HJ Juretschke. Electromagnetic theory of dc effects in ferromagnetic resonance. *Journal of Applied Physics*, 31(8):1401–1406, 1960.

[7] J. J. Parks, A. R. Champagne, T. A. Costi, W. W. Shum, A. N. Pasupathy, E. Neuscamman, S. Flores-Torres, P. S. Cornaglia, A. A. Aligia, C. A. Balseiro, G. K.-L. Chan, H. D. Abruña, and D. C. Ralph. Mechanical control of spin states in spin-1 molecules and the underscreened kondo effect. *Science*, 328(5984):1370–1373, 2010.

[8] MI Dyakonov and VI Perel. Possibility of orienting electron spins with current. *JETP LETTERS-USSR*, 13(11):467, 1971.

[9] JE Hirsch. Spin hall effect. *Phys. Rev. Lett.*, 83(9):1834–1837, AUG 30 1999.

[10] K. Ando, J. Ieda, K. Sasage, S. Takahashi, S. Maekawa, and E. Saitoh. Electric detection of spin wave resonance using inverse spin-hall effect. *Applied Physics Letters*, 94(26):262505, JUN 29 2009.

[11] O. Mosendz, V. Vlaminck, J. E. Pearson, F. Y. Fradin, G. E. W. Bauer, S. D. Bader, and A. Hoffmann. Detection and quantification of inverse spin hall effect from spin pumping in permalloy/normal metal bilayers. *Phys. Rev. B*, 82(21):214403, Dec 2010.

[12] V. E. Demidov, S. Urazhdin, E. R. J. Edwards, M. D. Stiles, R. D. McMichael, and S. O. Demokritov. Control of magnetic fluctuations by spin current. *Phys. Rev. Lett.*, 107:107204, Sep 2011.

[13] L Landau and E. Lifchitz. On the theory of the dispersion of magnetic permeability in ferromagnetic bodies. *Phys. Zeit. Sowjetunion*, page 8:153, 1935.

[14] RI Joseph and Scholman.E. Demagnetizing field in nonellipsoidal bodies. *Journal of Applied Physics*, 36(5):1579, 1965.

[15] R.D. McMichael and M.J. Donahue. Head to head domain wall structures in thin magnetic strips. *Magnetics, IEEE Transactions on*, 33(5):4167 –4169, sep 1997.

[16] B. Hillebrands and A. Thiaville, editors. *Spin Dynamics in Confined Magnetic Structures III*. Springer-Verlag Berlin, 2006.

[17] M. Klaeui. Head-to-head domain walls in magnetic nanostructures. *Journal of Applied Physics*, 20(31):313001, AUG 6 2008.

[18] M. D. Mascaro and C. A. Ross. ac and dc current-induced motion of a 360°domain wall. *Phys. Rev. B*, 82(21):214411, Dec 2010.

[19] M. N. Baibich, J. M. Broto, A. Fert, F. Nguyen Van Dau, F. Petroff, P. Etienne, G. Creuzet, A. Friederich, and J. Chazelas. Giant magnetoresistance of (001)fe/(001)cr magnetic superlattices. *Phys. Rev. Lett.*, 61:2472–2475, Nov 1988.

[20] G. Binasch, P. Grunberg, F. Saurenbach, and W. Zinn. Enhanced magnetoresistance in layered magnetic structures with antiferromagnetic interlayer exchange. *Phys. Rev. B*, 39:4828–4830, Mar 1989.

[21] T. Valet and A. Fert. Theory of the perpendicular magnetoresistance in magnetic multilayers. *Phys. Rev. B*, 48:7099–7113, Sep 1993.

[22] M. Julliere. Tunneling between ferromagnetic-films. *Phys.Lett. A*, 54(3):225–226, 1975.

[23] J. C. Slonczewski. Conductance and exchange coupling of two ferromagnets separated by a tunneling barrier. *Phys. Rev. B*, 39:6995–7002, Apr 1989.

[24] E.Y. Tsymbal, O.N. Mryasov, and P.R. LeClair. Spin-dependent tunneling in magneti tunnel junctions. *Journal of Applied Physics*, 15(4):R109–R142, 2003.

[25] M Viret, D Vignoles, D Cole, JMD Coey, W Allen, DS Daniel, and JF Gregg. Spin scattering in ferromagnetic thin films. *Phys. Rev. B*, 53(13):8464–8468, APR 1 1996.

[26] Peter M. Levy and Shufeng Zhang. Resistivity due to domain wall scattering. *Phys. Rev. Lett.*, 79:5110–5113, Dec 1997.

[27] KY Guslienko, BA Ivanov, V Novosad, Y Otani, H Shima, and K Fukamichi. Eigenfrequencies of vortex state excitations in magnetic submicron-size disks. *Journal of Applied Physics*, 91(10, Part 3):8037–8039, MAY 15 2002. 46th Annual Conference on Magnetism and Magnetic Materials, SEATTLE, WASHINGTON, NOV 12-16, 2001.

[28] K. Yu. Guslienko, S. O. Demokritov, B. Hillebrands, and A. N. Slavin. Effective dipolar boundary conditions for dynamic magnetization in thin magnetic stripes. *Phys. Rev. B*, 66(13):132402, Oct 2002.

[29] C.W. Sandweg, Y. Kajiwara, K. Ando, E. Saitoh, and B. Hillebrands. Enhancement of the spin pumping efficiency by spin wave mode selection. *Applied Physics Letters*, 97(25):252504, 20 December 2010.

[30] Y.V. Sharvin. A possible method for studying fermi surfaces. *Soviet Journal of Experimental and Theoretical Physics*, 21:655, September 1965.

[31] E. Scheer, P. Joyez, D. Esteve, C. Urbina, and M. H. Devoret. Conduction channel transmissions of atomic-size aluminum contacts. *Phys. Rev. Lett.*, 78:3535–3538, May 1997.

[32] J. C. Cuevas, A. Levy Yeyati, and A. Martin-Rodero. Microscopic origin of conducting channels in metallic atomic-size contacts. *Phys. Rev. Lett.*, 80:1066–1069, Feb 1998.

[33] E. Scheer, N. Agrait, JC. Cuevas, AL Yeyati, B Ludoph, A. Martin-Rodero, GR. Bollinger, JM. van Ruitenbeek, and C. Urbina. The signature of chemical valence in the electrical conduction through a single-atom contact. *Nature*, 394:154, 1998.

[34] J. Velev, R. F. Sabirianov, S. S. Jaswal, and E. Y. Tsymbal. Ballistic anisotropic magnetoresistance. *Phys. Rev. Lett.*, 94:127203, Mar 2005.

[35] G. Autès, C. Barreteau, D. Spanjaard, and M. Desjonquères. Electronic transport in iron atomic contacts: From the infinite wire to realistic geometries. *Phys. Rev. B*, 77:155437, Apr 2008.

[36] G. Autes. *Transport électronique polarisé en spin dans les contacts atomiques de fer*. PhD thesis, Université Paris VI, 2008.

[37] D. M. Pozar. *Microwave engineering*. Wiley, third edition, 2005.

[38] C.J. Muller, J.M. van Ruitenbeek, and L.J. de Jongh. Experimental observation from weak link to tunnel junction. *Physica C*, 191:485, 1992.

[39] M. V. Costache, S. M. Watts, M. Sladkov, C. H. van der Wal, and B. J. van Wees. Large cone angle magnetization precession of an individual nanopatterned ferromagnet with dc electrical detection. *Applied Physics Letters*, 89(23):232115, DEC 4 2006.

[40] M. V. Costache, S. M. Watts, C. H. van der Wal, and B. J. van Wees. Electrical detection of spin pumping: dc voltage generated by ferromagnetic resonance at ferromagnet/nonmagnet contact. *Phys. Rev. B*, 78(6):064423, AUG 2008.

[41] A. Yamaguchi, K. Motoi, A. Hirohata, and H. Miyajima. Anomalous hall voltage rectification and quantized spin-wave excitation induced by simultaneous application of dc and rf currents in a single-layered ni81fe19 nanoscale wire. *Phys. Rev. B*, 79(22):224409, JUN 2009.

[42] A. Yamaguchi, K. Motoi, H. Miyajima, and Y. Nakatani. Magnetic field dependence of rectification radio frequency current flowing through a single layered ferromagnetic wire. *Journal of Applied Physics*, 105(7):07D301, APR 1 2009. 53rd Annual Conference on Magnetism and Magnetic Materials, Austin, TX, NOV 11-14, 2008.

[43] Y. S. Gui, S. Holland, N. Mecking, and C. M. Hu. Resonances in ferromagnetic gratings detected by microwave photoconductivity. *Phys. Rev. Lett.*, 95:056807, Jul 2005.

[44] Y. S. Gui, N. Mecking, X. Zhou, Gwyn Williams, and C.-M. Hu. Realization of a room-temperature spin dynamo: The spin rectification effect. *Phys. Rev. Lett.*, 98:107602, Mar 2007.

[45] A. Yamaguchi, K. Motoi, A. Hirohata, H. Miyajima, Y. Miyashita, and Y. Sanada. Broadband ferromagnetic resonance of ni81fe19 wires using a rectifying effect. *Phys. Rev. B*, 78(10):104401, SEP 2008.

[46] M. V. Costache, M. Sladkov, C. H. van der Wal, and B. J. van Wees. On-chip detection of ferromagnetic resonance of a single submicron permalloy strip. *Applied Physics Letters*, 89(19):192506, NOV 6 2006.

[47] B. Leven and G. Dumpich. Resistance behavior and magnetization reversal analysis of individual co nanowires. *Phys. Rev. B*, 71(6):064411, Feb 2005.

[48] O. Rousseau, S. Petit-Watelot, and M. Viret. Large rf susceptibility of transverse domain walls. *J. Phys.: Condens. Matter*, 24:024211, 2012.

[49] C. H. Marrows. Spin-polarised currents and magnetic domain walls. *Advances in Physics*, 54:585, 2005.

[50] A Thiaville, Y Nakatani, J Miltat, and Y Suzuki. Micromagnetic understanding of current-driven domain wall motion in patterned nanowires. *EPL (Europhysics Letters)*, 69(6):990–996, MAR 2005.

[51] D. Bedau, M. Kläui, S. Krzyk, U. Rüdiger, G. Faini, and L. Vila. Detection of current-induced resonance of geometrically confined domain walls. *Phys. Rev. Lett.*, 99(14):146601, Oct 2007.

[52] S. Lepadatu, A. Vanhaverbeke, D. Atkinson, R. Allenspach, and C. H. Marrows. Dependence of domain-wall depinning threshold current on pinning profile. *Phys. Rev. Lett.*, 102(12):127203, MAR 27 2009.

[53] J. Grollier, M. V. Costache, C. H. van der Wal, and van Wees B. J. Microwave spectroscopy on magnetization reversal dynamics of nanomagnets with electronic detection. *Journal of Applied Physics*, 100:024316, 2006.

[54] Rai Moriya, Luc Thomas, Masamitsu Hayashi, Yaroslaw B. Bazaliy, Charles Rettner, and Stuart S. P. Parkin. Probing vortex-core dynamics using current-induced resonant excitation of a trapped domain wall. *Nature Physics*, 4(5):368–372, MAY 2008.

[55] http://math.nist.gov/oommf.

[56] E. Saitoh, H. Miyajima, T. Yamaoka, and G. Tatara. Current-induced resonance and mass determination of a single magnetic domain wall. *Nature*, 432:203, 2004.

[57] N. Biziere and C. Fermon. dc effect in a single micrometric spin valve sensor under ferromagnetic resonance. *Applied Physics Letters*, 92(9):092503–1–3, 3 March 2008.

[58] M Gabureac, M Viret, F Ott, and C Fermon. Magnetoresistance in nanocontacts induced by magnetostrictive effects. *Phys. Rev. B*, 69(10):100401, MAR 2004.

[59] O. Mosendz, J. E. Pearson, F. Y. Fradin, G. E. W. Bauer, S. D. Bader, and A. Hoffmann. Quantifying spin hall angles from spin pumping: Experiments and theory. *Phys. Rev. Lett.*, 104(4):046601, JAN 29 2010.

[60] A. Azevedo, L. H. Vilela-Leao, R. L. Rodriguez-Suarez, A. F. Lacerda Santos, and S. M. Rezende. Spin pumping and anisotropic magnetoresistance voltages in magnetic bilayers: Theory and experiment. *Phys. Rev. B*, 83(14):144402, Apr 2011.

[61] S. Zhang. Spin hall effect in the presence of spin diffusion. *Phys. Rev. Lett.*, 85(2):393–396, Jul 2000.

[62] Jairo Sinova, Dimitrie Culcer, Q. Niu, N. A. Sinitsyn, T. Jungwirth, and A. H. MacDonald. Universal intrinsic spin hall effect. *Phys. Rev. Lett.*, 92:126603, Mar 2004.

[63] S. Murakami, N. Nagaosa, and S. Zhang. Dissipationless quantum spin current at room temperature. *Science*, 301:1348, 2003.

[64] Y. Otani and T. Kimura. Spin current and spin hall effect in metallic nanostructures. *IEEE Transactions on Magnetics*, 44(7, Part 2):1911–1915, JUL 2008. 6th International Symposium on Magnetic Multilayers, Perth, AUSTRALIA, OCT 15-19, 2007.

[65] L. Vila, T. Kimura, and Y. Otani. Evolution of the spin hall effect in pt nanowires: Size and temperature effects. *Phys. Rev. Lett.*, 99:226604, Nov 2007.

[66] S.O. Valenzuela and M. Tinkham. Direct electronic measurement of the spin hall effect. *Nature*, 442:176, 2006.

[67] T. Yang, T. Kimura, and Y. Otani. Giant spin-accumulation signal and pure spin-current-induced reversible magnetization switching. *Nature Physics*, 4(11):851–854, NOV 2008.

[68] F.J. Jedema, M.V. Costache, H.B. Heersche, J.J.A. Baselmans, and B.J. van Wees. Electrical detection of spin accumulation and spin precession at room temperature in metallic spin valves. *Applied Physics Letters*, 81(27):5162–5164, DEC 30 2002.

[69] Yaroslav Tserkovnyak, Arne Brataas, and Gerrit E. W. Bauer. Enhanced gilbert damping in thin ferromagnetic films. *Phys. Rev. Lett.*, 88(11):117601, Feb 2002.

[70] Yaroslav Tserkovnyak, Arne Brataas, Gerrit E. W. Bauer, and Bertrand I. Halperin. Nonlocal magnetization dynamics in ferromagnetic heterostructures. *Rev. Mod. Phys.*, 77(4):1375–1421, Dec 2005.

[71] M.V. Costache, M. Sladkov, S.M. Watts, C.H. van der Wal, and B.J. van Wees. Electrical detection of spin pumping due to the precessing magnetization of a single ferromagnet. *Phys. Rev. Lett.*, 97(21):216603, 24 November 2006.

[72] K. Ando, Y. Kajiwara, K. Sasage, K. Uchida, and E. Saitoh. Inverse spin-hall effect induced by spin pumping in various metals. *IEEE Transactions on Magnetics*, 46(9):3694–3696, SEP 2010.

[73] K. Ando, Y. Kajiwara, S. Takahashi, S. Maekawa, K. Takemoto, M. Takatsu, and E. Saitoh. Angular dependence of inverse spin–hall effect induced by spin pumping investigated in a $ni_{81}fe_{19}/pt$ thin film. *Phys. Rev. B*, 78(1):014413, Jul 2008.

[74] K. Ando, T. Yoshino, and E. Saitoh. Optimum condition for spin-current generation from magnetization precession in thin film systems. *Applied Physics Letters*, 94(15):152509, APR 13 2009.

[75] Luqiao Liu, Takahiro Moriyama, D. C. Ralph, and R. A. Buhrman. Spin-torque ferromagnetic resonance induced by the spin hall effect. *Phys. Rev. Lett.*, 106:036601, Jan 2011.

[76] K. Ando, S. Takahashi, K. Harii, K. Sasage, J. Ieda, S. Maekawa, and E. Saitoh. Electric manipulation of spin relaxation using the spin hall effect. *Phys. Rev. Lett.*, 101:036601, Jul 2008.

[77] S. Mizukami, Y. Ando, and T. Miyazaki. Effect of spin diffusion on gilbert damping for a very thin permalloy layer in cu/permalloy/cu/pt films. *Phys. Rev. B*, 66(10):104413, Sep 2002.

[78] A Brataas, Y Tserkovnyak, GEW Bauer, and BI Halperin. Spin battery operated by ferromagnetic resonance. *Phys. Rev. B*, 66(6):060404, AUG 1 2002.

[79] Mark Johnson and R. H. Silsbee. Interfacial charge-spin coupling: Injection and detection of spin magnetization in metals. *Phys. Rev. Lett.*, 55(17):1790–1793, Oct 1985.

[80] S Kaka and SE Russek. Precessional switching of submicrometer spin valves. *Applied Physics Letters*, 80(16):2958–2960, APR 22 2002.

[81] SI Kiselev, JC Sankey, IN Krivorotov, NC Emley, RJ Schoelkopf, RA Buhrman, and DC Ralph. Microwave oscillations of a nanomagnet driven by a spin-polarized current. *Nature*, 425(6956):380–383, SEP 25 2003.

[82] K. Uchida, S. Takahashi, K. Harii, J. Ieda, W. Koshibae, K. Ando, S. Maekawa, and E. Saitoh. Observation of the spin seebeck effect. *Nature*, 455(7214):778–781, OCT 9 2008.

[83] A. Vanhaverbeke, O. Klein, M. Viret, and J. Ben Youssef. Nonlocal properties of a multidomain magnetic configuration. *Phys. Rev. B*, 80(18):184414, Nov 2009.

[84] A. Vanhaverbeke and M. Viret. Simple model of current-induced spin torque in domain walls. *Phys. Rev. B*, 75(2):024411, JAN 2007.